Imperial College London

Remote and Local Interactions of Extreme Weather Systems

Yan Lok Enoch Tsui

2023

Department of Physics

Imperial College London

Submitted in partial fulfilment of the requirements for the degree of
Doctor of Philosophy of Imperial College London and
the Diploma of Imperial College London

This page is intentionally left blank.

Abstract

Tropical cyclones, wildfires and regional precipitations are taken as examples of extreme weather. Their local and remote interactions with the environment and with each other are studied. Diabatic heating anomalies in both the atmosphere and ocean lead to large scale circulation anomalies, allowing for teleconnections of extreme weather events; while changing surface friction represents a kind of direct interaction with the environment.

Tropical cyclones in the Caribbean bring anomalous precipitation and hence latent heating and ascent over the region, resulting in a cross-equatorial thermally direct Hadley-type circulation anomaly with a descending branch over the Amazon and promotes fire-favourable atmospheric conditions there.

A new SubNiño4 index designed to capture the evolution of Pacific subsurface heat content in the El Niño-Southern Oscillation cycle is studied and shown to act as a long-range indicator for surface signals of the said cycle, outperforming the commonly used western equatorial Pacific warm water volume anomaly. It further works for atmospheric responses driven by the said cycle, including regional precipitation anomalies throughout the tropics and fires in Continental and Maritime Southeast Asia.

The boundary layer profiles of intensifying and steady-state tropical storms making landfall near Hong Kong are similar to each other but distinct from decaying ones. The decaying tropical storms have stronger inflow than non-decaying ones, driven by a much larger inflow angle in the mid- to low-level of the boundary layer under similar reduction in wind speed throughout. This is attributed to the weakening storms experiencing enhanced surface friction from land.

A sharp decrease in surface friction leads to the first, predominately purely dynamical, stage of a fast-slow re-intensification process in tropical cyclones moving back over ocean from land. They then continue onto a thermodynamically driven intensification due to a resumption of latent heat and moisture supply from a warm and moist ocean surface.

Statement of Originality

The contents of this thesis are the original work of the author, except where referenced. Most of the work presented in this thesis has been published in peer-reviewed journals as detailed below.

- Tsui, E. Y. L. & Toumi, R. (2021), 'Hurricanes as an enabler of Amazon fires', *Scientific Reports* **11**(1), 16960.
- Tsui, E. Y. L. & Toumi, R. (2022), 'Pacific subsurface temperature as a long-range indicator of El Niño, regional precipitation, and fire', *Quarterly Journal of the Royal Meteorological Society* **148**(746), 2102–2117.
- Tsui, E. Y. L., Chan, P. W. & Toumi, R. (2023), 'Boundary layer profile of decaying and non-decaying tropical storms near landfall', *Atmospheric Science Letters* **25**(1), e1189.

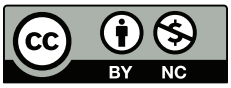
Copyright Declaration

The copyright of this thesis rests with the author. Unless otherwise indicated, its contents are licensed under a Creative Commons Attribution-Non Commercial 4.0 International Licence (CC BY-NC).

Under this licence, you may copy and redistribute the material in any medium or format. You may also create and distribute modified versions of the work. This is on the condition that: you credit the author and do not use it, or any derivative works, for a commercial purpose.

When reusing or sharing this work, ensure you make the licence terms clear to others by naming the licence and linking to the licence text. Where a work has been adapted, you should indicate that the work has been changed and describe those changes.

Please seek permission from the copyright holder for uses of this work that are not included in this licence or permitted under UK Copyright Law.



Acknowledgements

First and foremost I would like to express my most sincere gratitude to my supervisor Prof Ralf Toumi for putting up with me over the course of my PhD. You have demonstrated high standard, immense agility in the construction of scientific argumentation and great resourcefulness as an academic. I have much to learn from you.

I would like to thank Dr Kevin Hodges and Dr Arnaud Czaja for agreeing to be my viva examiners and Prof Timothy Horbury and Dr Edward Gryspeerdt for serving as my early stage assessment and late stage review examiners. I am particularly grateful to Dr Edward Gryspeerdt for your reassuring words whenever I have doubts as to whether I am on track along my PhD.

I would like to thank Dr Nathan Sparks, Dr Eric Lai and King Heng Lau for your support and friendships as fellow research groupmates. I am also indebted to you for the many Linux, WRF and Python know-hows without which my time as a PhD student at Imperial would have been much more difficult and excruciating.

I would like to thank Prof Shuai Wang for setting a very fine example for me as a highly respectable early career researcher with formidable industriousness, integrity and productivity. You have been a much comforting sight at the AMS 35th Conference on Hurricanes and Tropical Meteorology in New Orleans, when I was all by myself in a country I have never visited for my first ever academic conference, having been stood up by everyone in my own research group. I am also grateful for the career discussions we have had.

I would like to thank Dr Bahareh Kamranzad for sharing with me your own experience as an academic and telling me about the academic landscape of Japan. I am also grateful to you for listening to me when I felt lost, uncertain and doubtful of myself as a second year PhD student. Had I not known you, the idea of becoming a postdoctoral researcher in Japan and in general would probably have remained in the realm of fantasy rather than being turned into an active pursuit.

I would like to thank Dr Marie Shaylor for making it much less intimidating for me to blend in with the Imperial Space and Atmospheric Physics PhD community. Perhaps more importantly, you have shown much kindness and support to me as I approach the very unsettling final stage of my PhD.

Due to the COVID-19 pandemic, I have not been able to travel back to Hong Kong to meet my parents. I therefore cannot be more grateful to my aunt and uncle Anna and Albert Kwan for hosting me in Florida in the summer of my second year after I attended the AMS 35th Conference on Hurricanes and Tropical Meteorology in New Orleans and to my aunt and uncle Wendy and Laurent Guariglia for hosting me in Ermont over the Christmas and New Year of my third and fourth year. You have truly and in every sense of the expression given me a home away from home. I am also delighted by the coincidence that Wendy, Laurent and my parents were all in London on the day I had my viva.

I would like to thank my old friends from secondary school Franco Lam, Dr Tin Hang Hung and Janet Chik for spending time with me in and showing me around London. Because of you, I never truly felt alone here, even when I just arrived in this very foreign and at times unfriendly city. I am particularly grateful to Franco Lam, if not because of you I would not have queued 12 hours for the Laying-in-state of Her Majesty Queen Elizabeth II on 16 September 2022, which is now among some of the most cherished memories I have collected during my PhD.

I would like to thank Cathy Lau, Dr Tin Hang Hung, Dr Pok Man Tam and Wing Sum Lau for listening to and talking with me on multiple occasions from Hong Kong, Oxford, Pennsylvania and Kyoto respectively. Those conversations kept me from falling apart when I felt most weak and vulnerable for very different reasons.

I would like to thank Man Li Su and John Wong for your help and support, without which it would probably not have been possible for me to complete this thesis on time due to accommodation issues. Furthermore, you have made my stay in Glasgow highly enjoyable.

Last, I must thank the Leverhulme Centre for Wildfires, Environment and Society for funding my PhD.

Contents

List of Figures **11**

List of Tables **18**

1 Introduction **19**

1.1 Extreme weather 19

1.1.1 Tropical cyclones 19

1.1.2 Wildfires 24

1.2 Large scale atmospheric and oceanic circulations 25

1.2.1 Hadley and Walker circulations 28

1.2.2 El Niño-Southern Oscillation 29

1.3 Atlantic sea surface temperature variability and teleconnections 30

1.4 Atmospheric boundary layer 33

1.5 Layout of thesis 35

2 Data and methods **37**

2.1 European Centre for Medium-Range Weather Forecasts Reanalysis version 5 dataset 37

2.2 Moderate Resolution Imaging Spectroradiometer Collection 6 Active Fire Products 39

2.3 Fire danger indices historical data from the Copernicus Emergency Management Service 40

2.4 Tropical Rainfall Measuring Mission dataset 40

2.5 Global Precipitation Climatology Project dataset 41

2.6 Indian Institute of Tropical Meteorology rainfall dataset 42

2.7 Hadley Centre Sea Ice and Sea Surface Temperature dataset 43

2.8 Hadley Centre “EN” series version 4 dataset 44
2.9 International Best Track Archive for Climate Stewardship dataset 45
2.10 Hong Kong Observatory wind profiler dataset 47
2.11 Weather Research and Forecasting model 48

3 Hurricanes as an Enabler of Amazon Fires 52
3.1 Introduction 52
3.2 Methods 53
3.3 Results 54
3.3.1 Seasonal cycles of storms and fires 54
3.3.2 North Atlantic SST and ITCZ behaviour 55
3.3.3 Atlantic ITCZ and Caribbean precipitation 58
3.3.4 Caribbean storms and Amazon fires 59
3.3.5 Atmospheric Amazon fire risk factors 61
3.4 Discussion 62
3.5 Conclusions 67

4 Pacific Subsurface Temperature as a Long-range Indicator of El Niño, Regional Precipitation, and Fire 69
4.1 Introduction 69
4.2 Methods 71
4.3 Results 73
4.3.1 Connection between sea surface and subsurface temperatures 73
4.3.2 Delayed teleconnections of SubNiño4 77
4.3.2.1 Regional precipitation 77
4.3.2.2 Fires in Southeast Asia 82
4.4 Discussion 84
4.5 Conclusions 89

5 The Effects of Changing Surface Conditions on the Boundary Layer Structure of Weak Tropical Cyclones Near Landfall 91
5.1 Introduction 91
5.2 Methods 93
5.3 Results 96

5.4 Discussion 100
5.5 Conclusions 103

6 The Re-intensification of Tropical Cyclones Re-entering Ocean from Land 104
6.1 Introduction 104
6.2 Methods 105
6.3 Results 106
6.4 Discussion 115
6.5 Conclusions 119

7 Conclusions 121
7.1 Summary 121
7.2 Future work 123

Bibliography 127

Appendix A Supplementary Plots for Chapter 4 149

Appendix B Supplementary Plots for Chapter 5 151

List of Figures

1.1 Tracks and frequency of tropical cyclones and tropical storms. (Zehnder 2023) 20

1.2 Idealised radial cross section through an intense tropical cyclone showing the distributions of clouds, rain, radial flow and equivalent potential temperature (θ_e) on the left and azimuthal wind speed (u) and angular momentum (M) on the right. The θ_e contours are congruent with the M contours. (Wallace & Hobbs 2006) 21

1.3 Annual average number of fires observed by satellite from 2001 to 2006. (Bowman et al. 2009) 24

1.4 Annual average net primary productivity of carbon due to fires from 2001 to 2006. (Bowman et al. 2009) 25

1.5 Schematic of the fire parameterisation developed by Li et al. (2012). Text boxes in yellow, red, and blue colours represent 3 parts in the fire module: fire occurrence, fire spread, and fire impact. (Li et al. 2012) 26

1.6 Schematic of 3 fire danger rating systems — the American National Fire Danger Rating System (NFDRS), the Australian McArthur's Forest Fire Danger Meter (MARK-5) and the Canadian Fire Weather Index (FWI) System. (Di Giuseppe et al. 2016) 27

1.7 A schematic map indicating the location and seasonality of the typical precipitation effects in land regions that are favoured during El Niño events. (Davey et al. 2014) 31

1.8 A schematic map indicating the location and seasonality of the typical land temperature effects that are favoured during El Niño events. (Davey et al. 2014) 31

1.9 Vertical profile of (a) wind speed $|\vec{u}|$ and (b) angle of deviation with respect to $\vec{u}_g$ in the Ekman layer. 35

3.1 (a) Average annual fire count of northern South America between 2001 and 2018. The red box is the most fire-active region. (b) Seasonal cycles of Amazon fire count and North Atlantic (NA), Caribbean (Carib.) and non-Caribbean (non-Carib.) tropical cyclone number computed from 2001 to 2018. 55

3.2 (a) Scatter plot with linear least square fit of ASO Amazon fire count against ASO Caribbean tropical cyclone count in the years 2001–2018. Shaded region indicates 95% confidence interval. (b) Same as (a) except against non-Caribbean tropical cyclone count. 56

3.3 (a–b) Climatology of (a) MAM and (b) ASO precipitation between 2001 and 2018. (c–d) Same as (a–b) except for composite difference (significant at 95% confidence interval) of the top and bottom 5 years between 2001 and 2018 ranked by ASO Amazon fire count. Average precipitation difference over the Amazon is given in the lower right. (e–f) Same as (a–b) except for correlation with ASO Amazon fire count. (a–f) The red box is the Amazon fire region. (b, d, f) The orange box includes the Atlantic ITCZ. 57

3.4 Same as Figure 3.3 except for SST. The red box is the Amazon fire region. . . 58

3.5 (a) Scatter plot with linear least square fit of ASO Atlantic ITCZ precipitation against MAM North Atlantic SST in the years 2001–2018. Shaded region indicates 95% confidence interval. (b) Same as (a) except for ASO Caribbean precipitation. 59

3.6 (a, c, e) Composite difference of ASO horizontal wind at 850 hPa and precipitation (significant at 95% confidence interval) of the highest and lowest 5 years between 2001 and 2018 ranked by (a) ASO Amazon fire count, (c) ASO Atlantic ITCZ precipitation and (e) ASO Caribbean precipitation. (b, d, f) Same as (a, c, e) except for 850 hPa-200 hPa vertical wind shear. (a–f) The boxes are Amazon (red), Atlantic ITCZ (orange) and Caribbean (green). 60

3.7 (a) Scatter plot with linear least square fit of ASO Amazon vertical velocity at 600 hPa against ASO Caribbean tropical cyclone count computed from 1980 to 2019. Shaded region indicates 95% confidence interval. (c) Same as (a) except against ASO non-Caribbean tropical cyclone count. (e) Same as (a) except against ASO Caribbean precipitation. (b, d, f) Same as (a, c, e) except for ASO Amazon FWI. 63

3.8 (a, c, e) Composite difference (significant at 95% confidence interval) for ASO precipitation of the top and bottom 13 years between 1980 and 2019 ranked by (a) ASO Amazon FWI, (c) ASO Caribbean tropical cyclone count and (e) ASO Caribbean precipitation. Average precipitation difference (significant at 95% confidence interval) over the Caribbean and the Amazon are given in the upper right and lower right respectively. (b, d, f) Same as (a, c, e) except for vertical velocity at 600 hPa. 64

4.1 Blue box is the Niño3.4 region. Orange box shows the horizontal extant of the SubNiño4 region. Green box shows the horizontal extant of the region over which WWV_W is defined. Pink boxes are the domains considered for regional precipitations, except for that covered by the IITM all-India dataset. Red boxes are the domains considered for Southeast Asian fires. 73

4.2 (a) Time series of the SubNiño4 and Niño3.4 indices. Subsurface warm (cold) events are indicated with pink (cyan) shading. (b) Frequency spectra of SubNiño4 and Niño3.4. The dashed lines indicate the 95-th percentile amplitude from an ensemble of 10000 AR(1) model simulations. (c) Normalised histogram of SubNiño4 and Niño3.4 with mean (μ), standard deviation (σ), skewness (g_1) and excess kurtosis (β_2). (d) Same as (c) but for Niño4-Z20 anomaly. (e) Same as (c) but for surface zonal wind stress anomaly over the Niño4 region. (f) Observation weights for SubT at 27 different points within the SubNiño4 region (grey) and the average (pink). The red line marks the beginning of 1979. 75

4.3 Composite difference of SubT profile averaged between 5° S and 5° N between subsurface warm and cold events with various lead/lag times. Only difference deemed significant at 95% confidence or above by bootstrapping with 5000 resamples is shown. The dashed grey line and the black box indicate the climatological 20 °C isotherm and the extent of the SubNiño4 region respectively. Anchor for subsurface warm events: February 1981, May 1986, March 1989, October 1989, February 1997, July 2004, December 2007, August 2018; anchor for subsurface cold events: August 1983, July 1987, February 1992, May 1993, January 1995, December 1997, March 2010, January 2016. 76

4.4 Similar to Figure 4.3 but showing correlation ($p < 0.05$) between the SubNiño4 index and SubT profile averaged between 5° S and 5° N with various lead/lag times from the peak of subsurface warm/cold events. 77

4.5 (a) Correlation, r, between Niño3.4 in DJF and SubNiño4 (orange) and WWV_W anomaly (green) in the 25 overlapping 3-month periods immediately prior. (b) Same as (a) but for MAM. (c) Same as (a) but for JJA. (d) Same as (a) but for SON. (a–d) Correlations with $p < 0.05$ are indicated with solid dot markers and connected with solid line. Grey shading indicates correlation levels with $p \geq 0.05$. 78

4.6 (a) Correlation ($p < 0.05$) between precipitation in DFJ and the SubNiño4 index 12 months prior. (b) Same as (a) but for MAM. (c) Same as (a) but for JJA. (d) Same as (a) but for SON. (a–d) The black box indicates the extent of the SubNiño4 region. 78

4.7 (a) Correlation, r^2, between Maritime Continent precipitation in DJF and SubNiño4 (orange), WWV_W anomaly (green) and Niño3.4 (blue) in the 25 overlapping 3-month periods immediately prior. (b) Same as (a) but for MAM. (c) Same as (a) but for JJA. (d) Same as (a) but for SON. (a–d) Correlations with $p < 0.05$ are indicated with solid dot markers and connected with solid line. Grey shading indicates correlation levels with $p \geq 0.05$. . . . 79

4.8 (a) Same as Figure 4.7 (a) but for Northeast Brazil precipitation in MAM. (b) Same as (a) but for South Africa precipitation in DJFM. 80

4.9 (a) Same as Figure 4.7 (a) but for Gulf of Guinea precipitation in JJAS. (b) Same as (a) but for Sahel precipitation. 81

4.10 (a) Same as Figure 4.7 (a) but for East Africa precipitation in OND. (b) Same as (a) but for MAM. 81

4.11 (a) Same as Figure 4.7 (a) but for India precipitation in JJAS computed with data from 1960 to 2016. (b) Same as (a) but computed with data from 1979 to 2016. 82

4.12 (a) Annual mean fire count over Southeast Asia. The red and purple boxes are for Continental and Maritime Southeast Asia respectively. (b) Same as Figure 4.7 (a) but for Continental Southeast Asia FWI in DJFM. (c) Same as (b) but for Maritime Southeast Asia FWI in JASO. 83

5.1 Spatial distribution of wind profiler samples, classified into intensifying (IN) TS, steady-state (SS) TS, decaying (DE) TS and DE TC. (a) Geographic location of cyclone centre at the time of measurement. Location of the Sha Lo Wan weather station is indicated by the red dot. (b) Azimuthal angle (relative to the direction of cyclone translation) and distance (normalised by R_{max}) of the Sha Lo Wan weather station from cyclone centre at the time of measurement. 94

5.2 Boundary layer profile of inflow angle for intensifying (IN), steady-state (SS) and decaying (DE) TS averaged over (a) all samples and (b) samples in the front-left quadrant. 98

5.3 Same as Figure 5.2 but for reduction factor. 98

5.4 Same as Figure 5.2 but for radial velocity. 99

6.1 Overview of the development (dev, cyan), landfall (lf, brown) and seafall (sf, blue) runs of the experiment, showing the time-evolutions of (a) V_{max}, (b) p_{min}, (c) R_{max} and (d) $\tilde{R}_{\mathrm{max}}$. 108

6.2 Post-seafall time-evolution of certain tropical cyclone properties in the individual seafall runs (light blue) and average (solid blue) — (a) $V_{\max}$; (b) difference in $V_{\max}$ with respect to the value at seafall; (c) same as (b) but with respect to the value 1 hour after seafall; (d–f) same as (a–c) but for $p_{\min}$; (g) $V_{\max}/V_{\text{gwb}}$; (h) $\alpha_{\max}$. (a–h) Cyan line indicates the average value between the 5-th and 8-th days in the development run as a representative value. . . . 109

6.3 Post-seafall time-evolution of certain tropical cyclone properties in the individual seafall runs (light blue) and average (solid blue) for groups classed by $V_{\max}$ 1 hour after seafall. (a) $V_{\max}$ for cyclones with $57.3\,\text{kt} \leq V_{\max} < 67.6\,\text{kt}$ 1 hour after seafall. (b) Same as (a) but showing the difference of $V_{\max}$ with respect to the value 1 hour after seafall. (c) Same as (a) but showing $p_{\min}$. (d) Same as (a) but showing $l_{\max}$. (e–h), (i–l), (m–p), (q–t) Same as (a–d) except for cyclones with $67.6\,\text{kt} \leq V_{\max} < 77.8\,\text{kt}$, $77.8\,\text{kt} \leq V_{\max} < 88.1\,\text{kt}$, $88.1\,\text{kt} \leq V_{\max} < 98.4\,\text{kt}$, $98.4\,\text{kt} \leq V_{\max} < 108.6\,\text{kt}$ 1 hour after seafall. (a–t) Cyan line shows the time-evolution of the corresponding tropical cyclone property over a window in the initial intensification stage of the development run such that the $V_{\max}$ at hour 1 corresponds to the seafall group average value. 110

6.4 Scatter plots with linear least square fit of post-seafall $\dot{V}_{\max}$ against (a) $V_{\max}$, (c) $p_{\min}$, (d) $R_{\max}$, (e) $\tilde{R}_{\max}$ and (f) I at seafall and (b) $V_{\max}$ 1 hour after seafall, where the post-seafall $\dot{V}_{\max}$ are obtained by linearly regressing the time series of $V_{\max}$ within the 6-hour window beginning 1 hour after seafall. Shaded regions indicate 95% confidence interval. 112

6.5 Same as Figure 6.4 but with post-seafall $\dot{V}_{\max}$ obtained by linearly regressing the time series of $V_{\max}$ within the 24-hour window beginning 1 hour after seafall. 113

6.6 (a–m) Scatter plots with linear least square fit of $\Delta\tilde{R}_{\max}$ against $\tilde{R}_{\max}$ at seafall at various time after seafall. (n) Sensitivity of $\Delta\tilde{R}_{\max}$ against $\tilde{R}_{\max}$ at seafall as a function of time after seafall. (o) Squared correlation coefficient and p-value between $\Delta\tilde{R}_{\max}$ and $\tilde{R}_{\max}$ at seafall as a function of time after seafall. (a–n) Shaded regions indicate 95% confidence interval. 114

6.7 Composite azimuthal average radial profile of V_{surf} in seafall runs with $\tilde{R}_{\max} < 75\,\text{km}$ at seafall every 3 hours since seafall. 115

6.8 Same as Figure 6.7 but for $L_Z^{5\,\mathrm{km}}$. 116
6.9 Same as Figure 6.7 but for w. 117

A.1 Same as Figure 4.7 but showing r. 149
A.2 Same as Figure 4.8 but showing r. 149
A.3 Same as Figure 4.9 but showing r. 150
A.4 Same as Figure 4.10 but showing r. 150
A.5 Same as Figure 4.11 but showing r. 150
A.6 Same as Figure 4.12 but showing r. 150

B.1 Same as Figure 5.1 but for TS only, classified into close to ($< 80\,\mathrm{km}$) and far from ($\geq 80\,\mathrm{km}$) land. 151
B.2 Same as Figure 5.2 but with profiles composited by cyclone centre's distance to land. 152
B.3 Same as Figure 5.3 but with profiles composited by cyclone centre's distance to land. 152
B.4 Same as Figure 5.4 but with profiles composited by cyclone centre's distance to land. 153
B.5 Same as Figure 5.2 but for decaying TS and TC. 153
B.6 Same as Figure 5.3 but for decaying TS and TC. 154
B.7 Same as Figure 5.4 but for decaying TS and TC. 154

List of Tables

5.1 Intensifying TS measurements summary statistics. Bold for quadrants with at least 10 samples. 94
5.2 Steady-state TS measurements summary statistics. Bold for quadrants with at least 10 samples. 94
5.3 Decaying TS measurements summary statistics. Bold for quadrants with at least 10 samples. 95
5.4 Decaying TC measurements summary statistics. Bold for quadrants with at least 10 samples. 95

6.1 Areas bounded above by the development run curve and below by the averaged seafall run curve between hour 1 and hour 72 in Figure 6.3 (b, f, j, n, r). 108

Chapter 1

Introduction

1.1 Extreme weather

Extreme weather refers to those weather events that deviate significantly from historic norms, in other words occurrences that fall onto the extremes of climate variability such as droughts and floods. They are often hazardous and costly from a socio-economical point of view. In this thesis, the primary focus is placed on tropical cyclones and wildfires.

1.1.1 Tropical cyclones

Lasting from a few days up to several weeks (Chan & Kepert 2010), tropical cyclones are highly, but not exactly, axisymmetric atmospheric vortices formed over warm tropical oceans driven by fluxes of latent and sensible heat, moisture and momentum at the air-sea interface (Wallace & Hobbs 2006, Chan & Kepert 2010). They possess considerable destructive power, mainly threatening coastal regions from the high tropics all the way to the subtropics (Chan & Kepert 2010). Figure 1.1 shows the major tracks and seasons for tropical cyclones around the globe together with frequency of occurrence for individual ocean basins.

3 theories regarding tropical cyclone core formation have been proposed, all of which are centred around mesoscale convective systems and/or associated mesoscale convective vortices enhancing low-level cyclonic vorticity (Chan & Kepert 2010). It is then essential for these mesoscale convective systems and mesoscale convective vortices to moisten and somewhat stabilise at the lower- to middle-troposphere such that downdrafts are inhibited

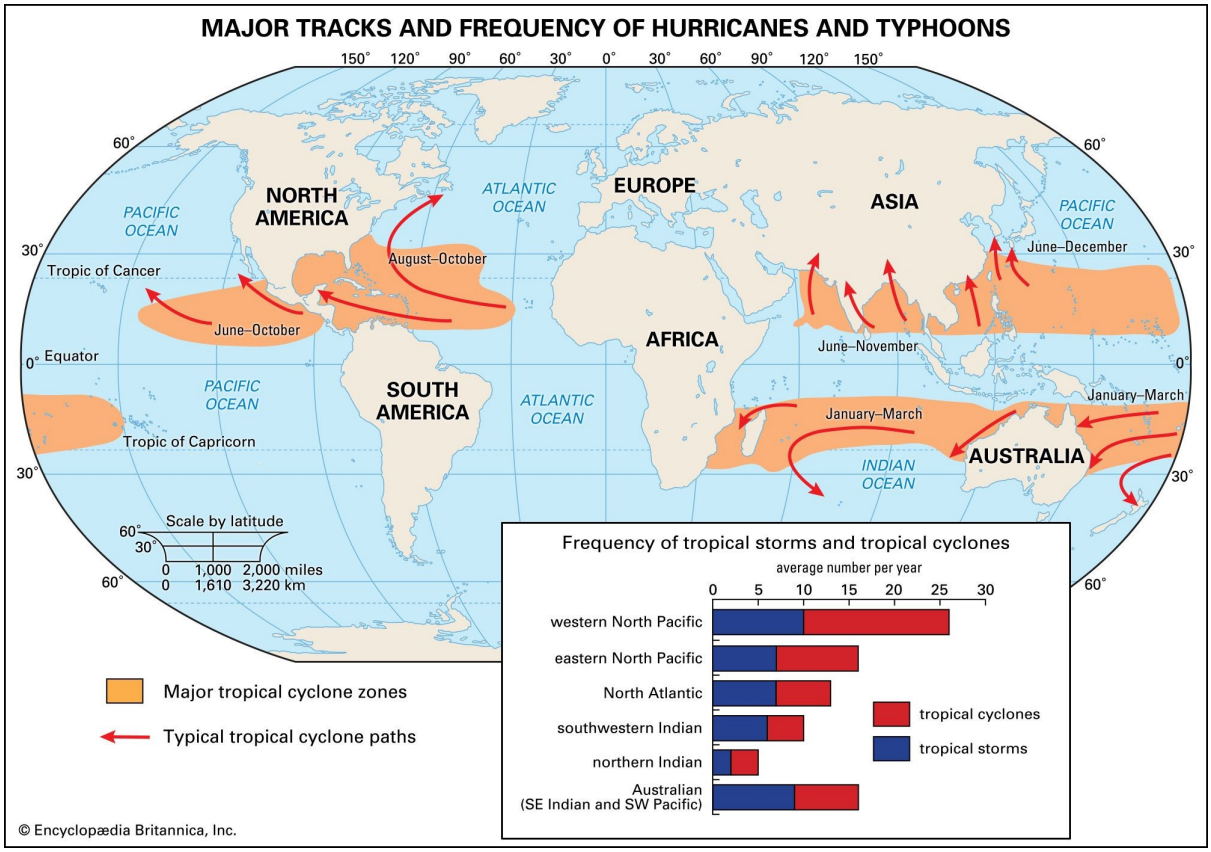


Figure 1.1: Tracks and frequency of tropical cyclones and tropical storms. (Zehnder 2023)

while convective potential remains (Chan & Kepert 2010, Wallace & Hobbs 2006). Finally, the cold vortex core warms up and becomes downdraft-free and self-sustaining (Wallace & Hobbs 2006, Chan & Kepert 2010). The heat and moisture required are provided by the ocean in the form of fluxes at the air-sea interface into the low-level inflow air (Wallace & Hobbs 2006, Chan & Kepert 2010), which is brought into cyclonic motion by the Coriolis force (Wallace & Hobbs 2006).

For tropical cyclones to form, the sea surface temperature must be sufficiently high, usually above 26.5 °C (Wallace & Hobbs 2006, Chan & Kepert 2010), and a deep surface-based conditionally unstable layer must exist (Chan & Kepert 2010). The latitude must be sufficiently high so that the Coriolis effect is appreciable to bring the low-level inflow air into cyclonic motion (Wallace & Hobbs 2006). Tropical cyclone genesis and intensification is favoured by organised deep convection in an environment with large-scale mean ascent and high mid-level humidity (Chan & Kepert 2010), low-level cyclonic circulation (Maloney & Hartmann 2000), weak vertical wind shear (Gray 1968) and a weakening of trade winds (Inoue et al. 2002). Higher sea surface and tropospheric temperatures are in general

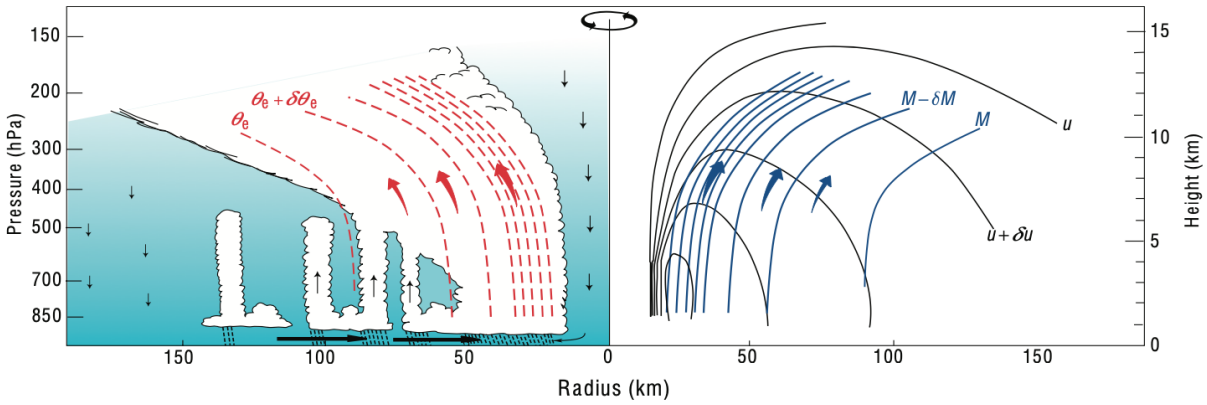


Figure 1.2: Idealised radial cross section through an intense tropical cyclone showing the distributions of clouds, rain, radial flow and equivalent potential temperature (θ_e) on the left and azimuthal wind speed (u) and angular momentum (M) on the right. The θ_e contours are congruent with the M contours. (Wallace & Hobbs 2006)

favourable to the development of tropical cyclones to higher intensity (Bister & Emanuel 2002).

Figure 1.2 shows the structure of an idealised intense tropical cyclone. In a mature tropical cyclone, there is an eye, typically with a radius between 10 km and 50 km (Chan & Kepert 2010), at the centre of the warm core (Wallace & Hobbs 2006) extending through much of the troposphere (Chan & Kepert 2010). The eye has exceptionally low pressure (Wallace & Hobbs 2006), which can be lower than the ambient pressure by as much as 10% (Chan & Kepert 2010), but is relatively calm (Chan & Kepert 2010, Wallace & Hobbs 2006). It is devoid of clouds and wind speeds are low (Chan & Kepert 2010, Wallace & Hobbs 2006). Above the boundary layer, the air is in descent with temperature increasing and humidity decreasing as height increases (Wallace & Hobbs 2006). In other words, there are a temperature inversion and a thermally indirect circulation in the eye (Wallace & Hobbs 2006). The eye is surrounded by a rapidly rotating ring of deep convective clouds, called the eyewall, rising from just above sea surface all the way to the tropopause (Chan & Kepert 2010, Wallace & Hobbs 2006). The eyewall itself is further surrounded by spiral rain bands (Chan & Kepert 2010, Wallace & Hobbs 2006). The whole system can have a spatial extent of over 150 km in radius (Wallace & Hobbs 2006). Outside the eye in the eyewall and rain bands, air is in ascent under extensive thermally direct circulation, feeding kinetic energy and angular momentum into the system (Chan & Kepert 2010, Wallace & Hobbs 2006).

In the inner core region near the eyewall, the azimuthal wind is in near cyclostrophic

balance with the temperature field, meaning that the vertical gradient of angular momentum is proportional to the radial gradient of temperature, except in the surface boundary layer and the high-level outflow layer (Chan & Kepert 2010, Wallace & Hobbs 2006). Given the ascent in the warm core, cyclostrophic balance dictates that the azimuthal winds must weaken as height increases (Chan & Kepert 2010, Wallace & Hobbs 2006). To conserve angular momentum, the air spirals outwards as it rises leading the eyewall to slope outwards as height increases (Wallace & Hobbs 2006, Chan & Kepert 2010). Since cyclostrophic balance is the 2-way balance between pressure gradient force and centripetal force, it is a good approximation only for the inner core region, where a combination of high wind speed and small radius of curvature causes the centripetal force to dominate over the Coriolis force. As the wind speed drops and the radius of curvature increases away from the cyclone centre beyond the eyewall, the Coriolis force becomes more and more important relative to the centripetal force and cyclostrophic balance slowly gives way to gradient wind balance — the 3-way balance among pressure gradient force, centripetal force and Coriolis force — in the middle region. Further beyond in the outer region, the centripetal force becomes so weak that geostrophic balance — the 2-way balance between pressure gradient force and Coriolis force — becomes a good approximation. The momentum transfer from surface air into the sea due to friction breaks the wind balance at the surface boundary layer, causing a low-level cyclonic inflow (Chan & Kepert 2010, Wallace & Hobbs 2006). On the other hand, the high-level outflow is anticyclonic and displays much poorer axisymmetry (Chan & Kepert 2010, Wallace & Hobbs 2006).

The movement of tropical cyclones is dominated by some sort of average of the surrounding horizontal flow, called the steering flow, and the Coriolis effect under presumed barotropic conditions (Chan & Kepert 2010). The advection of the relative vorticity of a tropical cyclone by the steering flow causes it to move downstream. The Coriolis force leads to an advection of planetary vorticity and a subsequent adjustment in relative vorticity change, termed the beta effect. The beta effect introduces an additional westward and poleward component to the movement of tropical cyclones on top of that due to the steering flow. Interaction with another nearby tropical cyclone (Fujiwhara effect), baroclinic effects and interaction with land surface and topography near landfall also act to modify tropical cyclone tracks (Chan & Kepert 2010).

Generally speaking, tropical cyclones drift westwards for a week before recurving pole-

wards around the western flanks of the subtropical anticyclones (Wallace & Hobbs 2006). Eventually, they either find themselves entering high latitude oceans or making landfall. Over high latitude oceans where the sea surface temperature is too low to sustain tropical cyclones, they may dissipate entirely or undergo extratropical transition and develop into a cold core structure (Chan & Kepert 2010). Over land, tropical cyclones are cut off from the supply of heat and moisture from the ocean and under enhanced surface friction, causing them to weaken (Wallace & Hobbs 2006); unless the land surface is exceptionally warm and wet, in which case tropical cyclones may maintain intensity or re-intensify over land (e.g. Emanuel et al. 2008, Wakefield et al. 2021).

As a tropical cyclone makes landfall, the strong winds and heavy precipitation it developed over the ocean hit the concerned coastal regions with full force (Wallace & Hobbs 2006). Furthermore, the surface wind stress, atmospheric pressure deficit and momentum transfer into the ocean due to the tropical cyclone raises the water level, causing what is known as a storm surge (Chan & Kepert 2010). As the storm surge closes in to the shore, it is enhanced by the shallow shelf and can lead to flooding in vast coastal low-lying areas (Chan & Kepert 2010). While tropical cyclones occur in all ocean basins except the South Atlantic and the Southeast Pacific (Gray 1968, Wallace & Hobbs 2006, Chan & Kepert 2010), tropical cyclones are more active in the Northern Hemisphere with the Northwest Pacific being most frequently hit (Gray 1968). Given the general pattern of their tracks, it is clear that the high impact ones are found mainly in the Northwest Pacific and the North Atlantic.

There are conflicting views in the tropical cyclone research community as to whether climate change leads to an increasing, decreasing or insignificant trend in the overall annual tropical cyclone count (Chan & Kepert 2010). However, increasing sea surface temperature, tropospheric temperature and tropospheric water vapour content in the tropical ocean basins causes an increase in both the number and intensity of the most intense tropical cyclones by raising both the convective available potential energy and maximum potential intensity over there (Chan & Kepert 2010, Knutson et al. 2010, Kossin et al. 2020, Emanuel 2020). Increase in tropospheric water vapour content also leads to an increase in precipitable water vapour in the tropics, enhancing tropical cyclone-related precipitation (Chan & Kepert 2010). Tropical cyclones are also migrating polewards with their location of lifetime maximum intensity shifting closer to land, driven by climate change-induced modifications to large scale atmospheric circulations (Wang & Toumi 2021). Moreover, a rising sea level

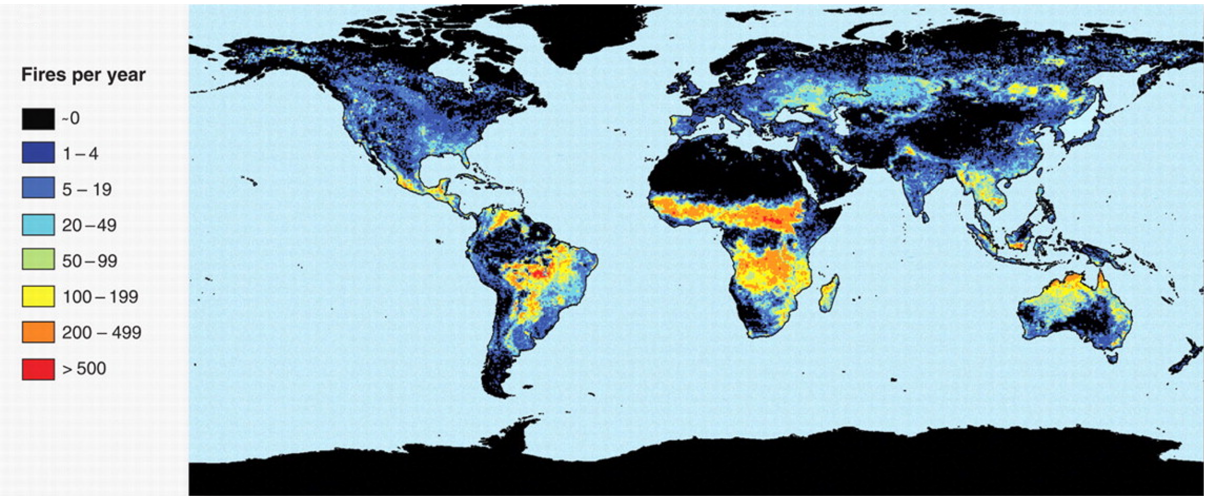


Figure 1.3: Annual average number of fires observed by satellite from 2001 to 2006. (Bowman et al. 2009)

further enhances the severity of tropical cyclone storm surge (Lin et al. 2012).

1.1.2 Wildfires

Wildfires occur globally affecting all vegetated land mass (Figure 1.3). They are destructive in both ecological and socioeconomic terms (Cury et al. 2020, Bowman et al. 2009). As seen from Figure 1.3, regions affected by high-frequency fires are mainly concentrated within the tropics. Wildfires are important contributors to the budget and growth of several trace gases and aerosols, including greenhouse gases (van der Werf et al. 2010, Bowman et al. 2009). For example, Figure 1.4 shows the net primary productivity of carbon due to fires. South America and equatorial Asia are the 2 major regions that contribute to the global net fire carbon emission (van der Werf et al. 2010).

Some environmental factors that affect wildfires have been identified, for example they are more probable under drought conditions (Bowman et al. 2009), can be sparked by lightning (Rodríguez-Pérez et al. 2020), intensified by wind (Clark et al. 1996) and their activities affected by El Niño-Southern Oscillation (Burton et al. 2020, Bowman et al. 2009). An appreciable amount of fires are set deliberately by humans for a number of purposes including agriculture, deforestation, fuel hazard management, habitat maintenance and stimulation of forest and pasture regeneration (Bowman et al. 2009, Berenguer et al. 2021). In various fire models (e.g. Thonicke et al. 2010, Li et al. 2012, Mangeon et al. 2016), both meteorological and anthropogenic variables and processes are considered. Figure 1.5 is a

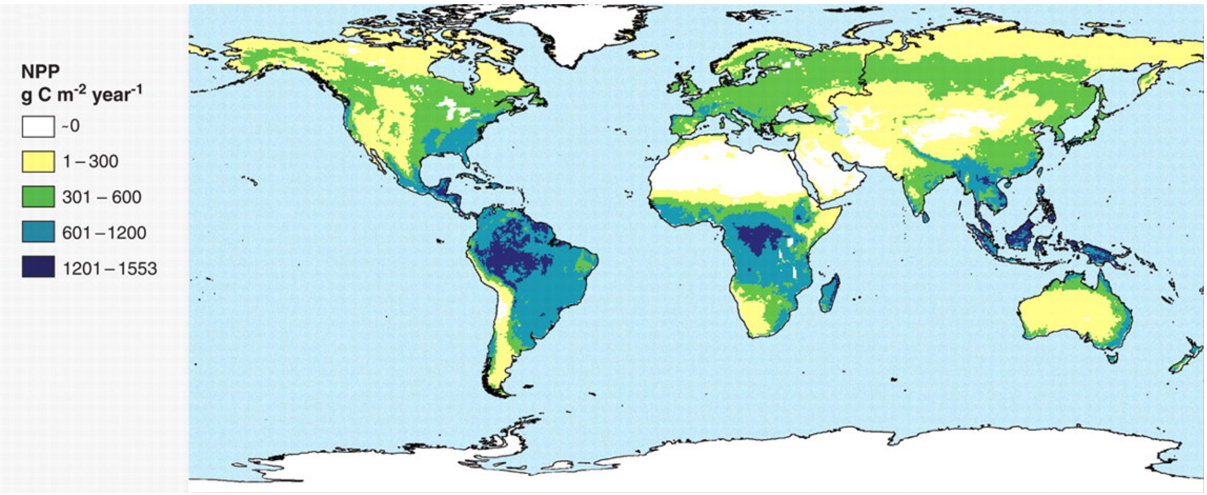


Figure 1.4: Annual average net primary productivity of carbon due to fires from 2001 to 2006. (Bowman et al. 2009)

schematic diagram for the fire model developed by Li et al. (2012) for example.

It is clear that not all wildfires are pure meteorological phenomena. They are usually modelled as a culmination of extreme weather events with anthropogenic modulations. However, meteorological factors does have a direct effect on the severity of any wildfires regardless of their origin, including anthropogenic ones. It is also conceivable that humans would choose to start fires under favourable meteorological conditions for convenience and efficiency. To focus on the meteorological aspects of wildfires, various fire risk indices developed by agencies around the globe are helpful. They are essentially output from fire models that do not incorporate any anthropogenic components but are otherwise complete. Surface temperature, wind, humidity, cloud cover and precipitation are among the common meteorological variables considered. Figure 1.6 shows schematically the fire models behind 3 different fire danger rating systems, illustrating how fire-favourable conditions result from a culmination of extreme weather events over time.

1.2 Large scale atmospheric and oceanic circulations

It is clear from the previous section that extreme weather are modulated locally by the environment in which they are embedded. They can also interact locally with each other. For example, the presence of Hurricane Ophelia (2017) off the coast of Portugal greatly enhanced the spread and severity of the fires of October 2017 in Portugal by bringing hot dry air from northern Africa into Portugal and subjecting the region to strong wind (Ramos

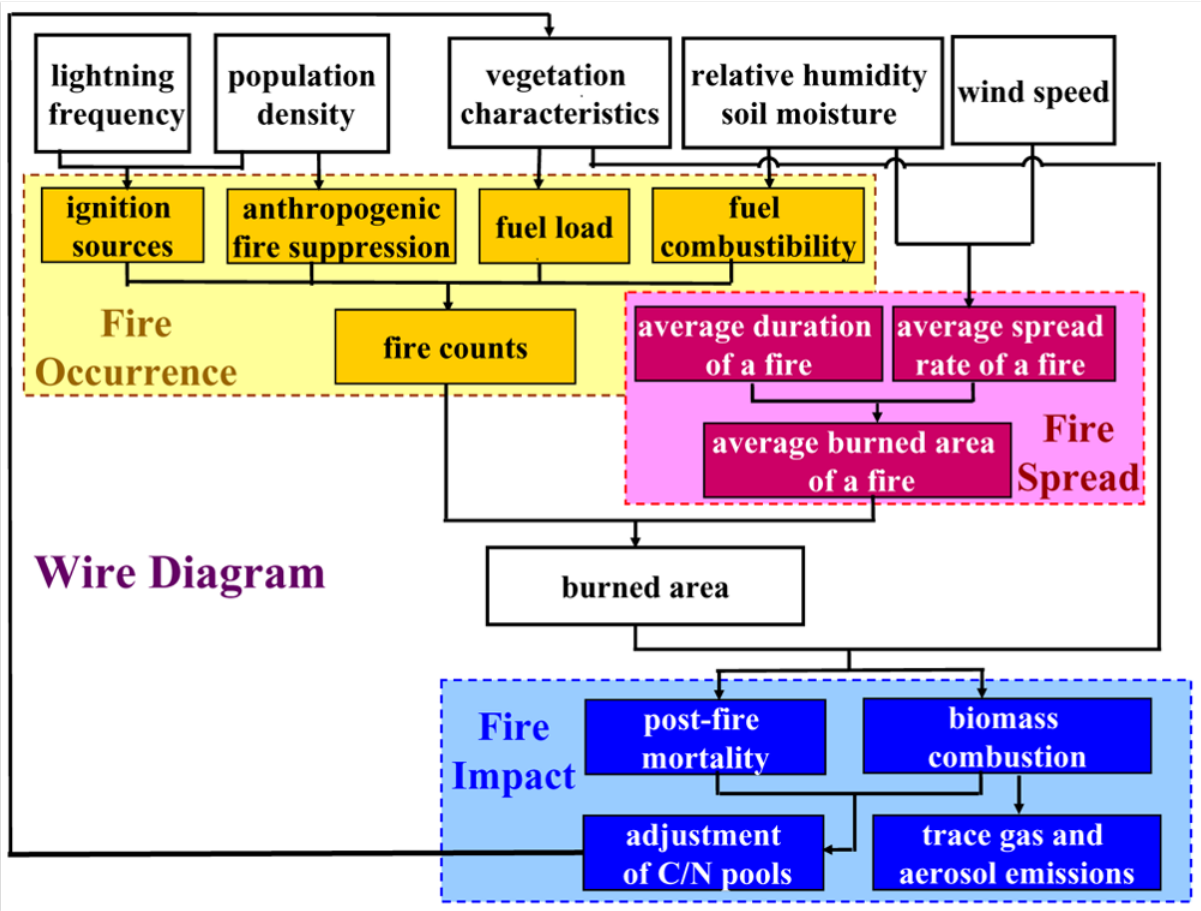


Figure 1.5: Schematic of the fire parameterisation developed by Li et al. (2012). Text boxes in yellow, red, and blue colours represent 3 parts in the fire module: fire occurrence, fire spread, and fire impact. (Li et al. 2012)

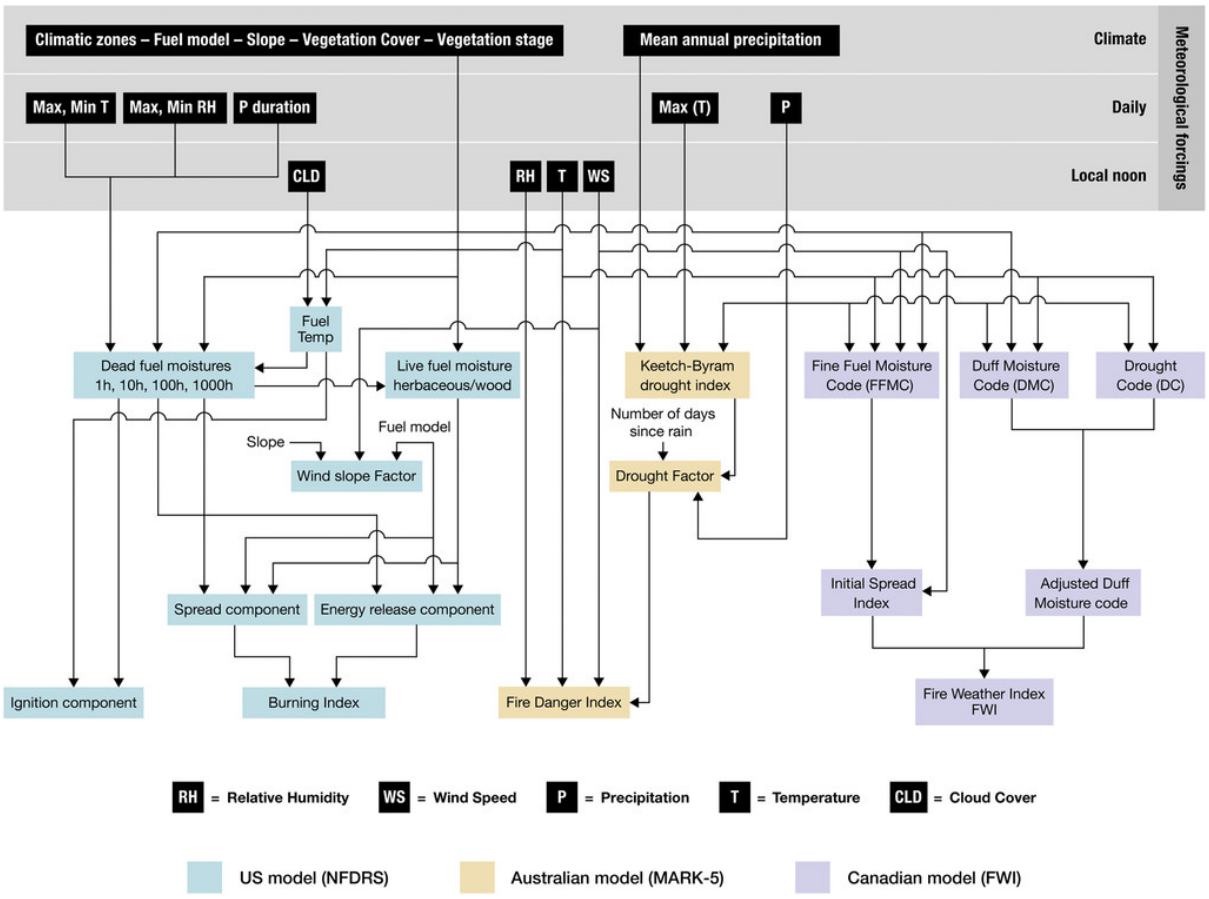


Figure 1.6: Schematic of 3 fire danger rating systems — the American National Fire Danger Rating System (NFDRS), the Australian McArthur's Forest Fire Danger Meter (MARK-5) and the Canadian Fire Weather Index (FWI) System. (Di Giuseppe et al. 2016)

et al. 2023). In addition to interacting locally with the environment and among themselves, extreme weather can also be connected to each other over vast distances with or without time lag — a phenomenon known as teleconnection. Large scale circulations both in the atmosphere and in the ocean can link extreme weather together or even provide a pathway for them to interact with each other directly, even though they may be separated in the space and/or time domain.

1.2.1 Hadley and Walker circulations

Hadley circulations are meridionally oriented thermally direct circulations which exist in each of the Northern and Southern Hemispheres (Lorenz 1967, Schneider 2006). Air rises near the equator due to differential heating. It then travels polewards in the upper troposphere to satisfy conservation of mass, acquiring an eastward component as it does so due to Coriolis force. The air sinks in higher latitudes due to differential cooling and travels equatorwards down the near-surface horizontal pressure gradient, acquiring a westward component as it does so due to Coriolis force, giving rise to the easterly trade winds. The Hadley circulations in the Northern and Southern Hemispheres would be completely symmetric on an idealised aqua-planet with symmetric heating along the equator. The spatial extent of the Hadley circulations and the relative position of their ascending and descending branches can be modified by the incorporation of off-equatorial and/or localised heating (Lindzen & Hou 1988, Gill 1980), background zonal wind (Phlips & Gill 1987) and orography (e.g. Rodwell & Hoskins 2001, Krishnan et al. 2003). In some cases, the circulation can cross the equator, with the ascending and descending branches located in opposite hemispheres.

The Walker circulation is a zonally oriented thermally direct circulation which exists in the equatorial Pacific first described by Bjerknes (1969). With a well-developed cold tongue in the equatorial East Pacific, the air above is cooled to such an extent that it is prevented from ascending due to its density. Unable to join the Hadley circulations, which are ascending in the tropics, the air instead flows westwards, down the near-surface horizontal pressure gradient, between the Hadley circulations of the Northern and Southern Hemispheres. Reaching the West Pacific warm pool, the air is heated and moistened by the warm ocean below and forced into moist-adiabatic ascent. In the upper troposphere, the horizontal pressure gradient is reversed. The air then flows eastwards and descends to

complete the circulation.

1.2.2 El Niño-Southern Oscillation

El Niño (La Niña) events refer to the warming (cooling) of the equatorial Pacific sea surface temperature (Wang 2018, Timmermann et al. 2018). These conditions are accompanied by a weakening (strengthening) of the Pacific equatorial trade winds and other changes in atmospheric and oceanic circulations (Timmermann et al. 2018). For example, the El Niño event in 2015/16 (L'Heureux et al. 2017) was triggered by successive westerly wind bursts in the equatorial East Pacific during the first quarter of 2015. This led to an eastward propagation of a dowelling oceanic Kelvin wave and deepened the thermocline of the eastern Pacific cold tongue, resulting in surface warming in the central and eastern Pacific in May to June 2015. As the heat supply to the ascending branch of the atmospheric Hadley circulation from the ocean surface is enhanced, the said circulation is intensified. Anomalous flux of westerly angular momentum is introduced to the mid-latitudes by the descending branch of the enhanced Hadley circulation, which is finally carried to the equator by the trade winds, forming a positive feedback loop known as the Bjerknes feedback (Bjerknes 1966, 1969). The 2015/16 El Niño event was brought to an end by the slow discharge of equatorial heat content into off-equatorial regions in early 2016.

The Southern Oscillation refers to the oscillatory exchange of air mass between the tropical East and West Pacific (Julian & Chervin 1978), or equivalently the oscillatory behaviour of the sea-level pressure between the tropical East and West Pacific (Wang 2018). It is intimately linked to fluctuations in the strength of the Walker circulation, whose near-surface leg is driven by the zonal sea surface temperature gradient in the equatorial Pacific (Bjerknes 1969, Wang 2018).

The warming and cooling of the equatorial Pacific sea surface temperature and the Southern Oscillation are now understood as different manifestations of the same basin-wide climate phenomenon termed El Niño-Southern Oscillation (ENSO), which is driven by coupled atmosphere-ocean processes (Wang 2018, Timmermann et al. 2018). The Bjerknes feedback (Bjerknes 1966, 1969) already explains how El Ninõ and La Niña can be brought to a mature state by a positive feedback among equatorial Pacific sea surface temperature anomaly, equatorial Pacific zonal wind anomaly via sea surface temperature gradient, Hadley circulation, Walker circulation and ocean circulation. The challenge is to explain

the oscillatory behaviour of ENSO, to which various negative feedback mechanisms have been put forward, giving rise to 4 different self-sustained oscillator models for ENSO:

- delayed oscillator model (Suarez & Schopf 1988, Battisti & Hirst 1989), based on the reflection of west-propagating downwelling Rossby waves into east-propagating downwelling Kelvin waves at the western boundary of the Pacific;
- recharge-discharge oscillator model (Jin 1997*a*,*b*), based on the discharge and recharge of equatorial Pacific ocean heat content to and from higher latitudes via Sverdrup transport;
- western Pacific oscillator model (Weisberg & Wang 1997, Wang et al. 1999), based on the upwelling Kelvin wave forced by wind anomalies in the western Pacific; and
- advective-reflective oscillator model (Picaut et al. 1997), based on the anomalous zonal current associated with the reflections of upwelling Rossby (downwelling Kelvin) waves into upwelling Kelvin (downwelling Rossby) waves at the western (eastern) boundary of the Pacific and the mean zonal current.

Wang (2001, 2018) nicely summarised the 4 self-sustained oscillator models into the unified oscillator model, suggesting that all proposed negative feedback mechanisms are at work together, the relative importance of which could vary with time.

ENSO affects global climate and marine and terrestrial ecosystems (Timmermann et al. 2018). It dominates interannual climate variability and affects seasonal precipitation, wind and temperature patterns over vast distances globally through dynamical atmospheric processes (Davey et al. 2014, Timmermann et al. 2018). For example, Figures 1.7 and 1.8 show the typical anomalies of precipitation and land temperature respectively around the globe favoured by El Niño.

1.3 Atlantic sea surface temperature variability and teleconnections

At interannual time scales, the variability of the sea surface temperature of the tropical North Atlantic is associated with both ENSO and the North Atlantic Oscillation (NAO, oscillation in the sea level pressure gradient between the subtropical and subartic North Atlantic)

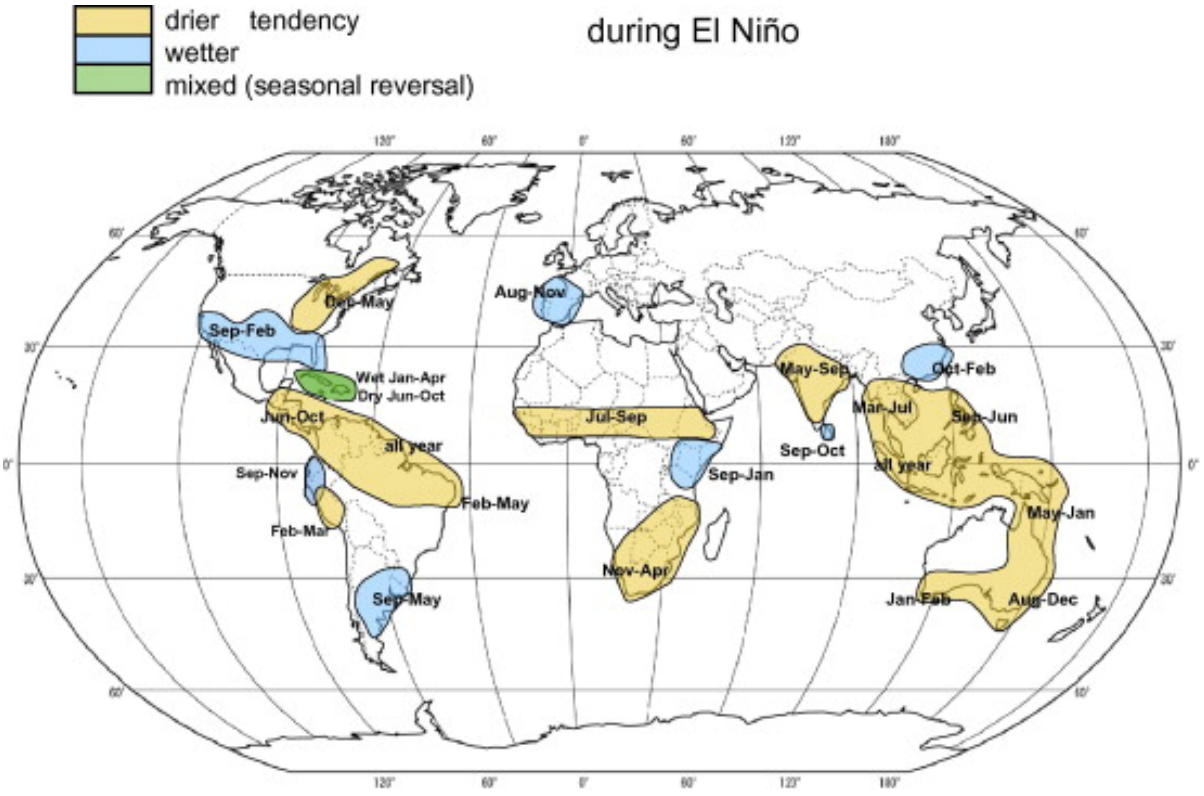


Figure 1.7: A schematic map indicating the location and seasonality of the typical precipitation effects in land regions that are favoured during El Niño events. (Davey et al. 2014)

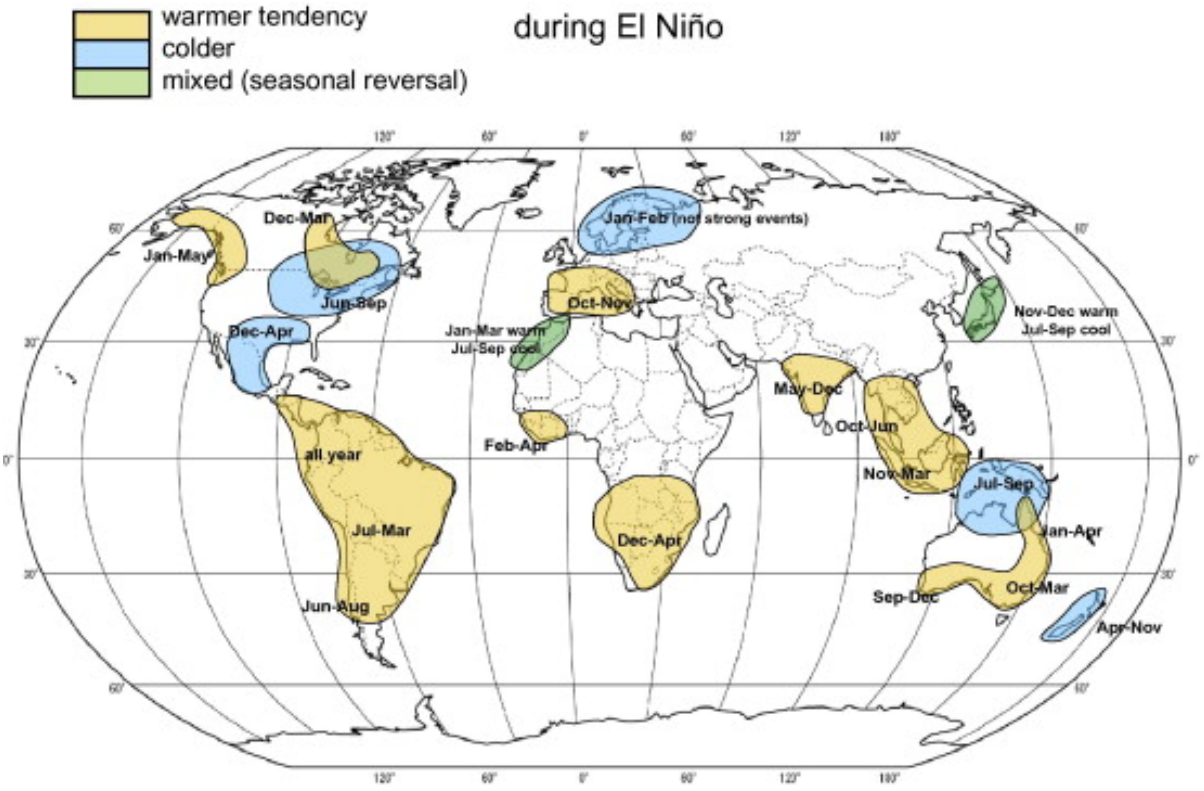


Figure 1.8: A schematic map indicating the location and seasonality of the typical land temperature effects that are favoured during El Niño events. (Davey et al. 2014)

through their modulation of the intensity of the trade winds and hence latent and sensible heating as well as entertainment cooling at the sea surface (Enfield & Mayer 1997, Klein et al. 1999, Czaja et al. 2002, Zhang et al. 2012). The teleconnection between the Pacific and Atlantic could be understood to be via Rossby wave propagation (Hastenrath 2000) or intensity changes in the Walker and Hadley circulation cells (Wang 2002, Wang & Enfield 2003). Under this context, ENSO also affects the cloud cover over the Atlantic and contributes to the radiative budget there. The area of the Atlantic warm pool is modulated by both ENSO and NAO (Zhang et al. 2012, Enfield et al. 2006). North Atlantic sea surface temperature displays teleconnection with Sahel (Liu et al. 2014) and Brazilian (Hastenrath 2000) precipitation and Eurasian summer climate (Li & Ruan 2018).

The sea surface temperature of the North Atlantic basin has been shown to also demonstrate oscillation with a period of several decades (Schlesinger & Ramankutty 1994, Kushnir 1994). The anomaly pattern is basin-wide with maxima in the vicinity of Iceland, in the Labrador Sea, and northeast of Bermuda (Kushnir 1994). This variability, now termed the Atlantic Multidecadal Oscillation (AMO), is commonly associated with the strength of the Atlantic meridional overturning circulation and with coupled ocean-atmosphere processes in the North Atlantic (Wills et al. 2019, Mann et al. 2014, Knight et al. 2005). During the warm (cold) phase of the AMO, the area of the Atlantic warm pool is lager (smaller) (Zhang et al. 2012, Wang et al. 2008) and an anomalous cyclonic (anticyclonic) circulation is set up in the middle of the ocean basin centred at 45° N and 35° W (Kushnir 1994). AMO is also linked with Sahel drought (Folland et al. 1986, Rowell et al. 1995), Northeast Brazilian precipitation variability (Folland et al. 2001), continental US precipitation and river flows (Enfield et al. 2001), Atlantic hurricane frequency (Goldenberg et al. 2001) and North American and European summer climate (Sutton & Hodson 2005). Ting et al. (2014) and Mann et al. (2014) pointed out the importance of properly isolating the true internal variability in the Atlantic sea surface temperature from that due to external natural and/or anthropogenic radiative forcing when assessing the amplitude and phase of the AMO and more crucially the remote climate impacts of it.

1.4 Atmospheric boundary layer

The atmospheric boundary layer, or boundary layer for short, is a layer of the atmosphere at the bottom of the troposphere, typically with a thickness of about 1 km to 2 km (Wallace & Hobbs 2006). The dynamics of the boundary layer is dominated by turbulence, which mixes momentum, heat, moisture and aerosols vertically. The boundary layer is thus the layer of the atmosphere which is most affected by its bottom boundary, in other words the Earth's surface. The top of the boundary layer is marked by a strong stable layer of capping inversion which acts to trap the turbulence and associated vertical transports within the boundary layer. As a result, the effects of surface friction is almost not felt by the free atmosphere, which is the part of the atmosphere sitting above the boundary layer.

Turbulent flow refers to one that contains a superposition of irregular swirls, called eddies, of many sizes. In the atmosphere, turbulence has a horizontal scale of motion below 2 km and is further classified into boundary-layer turbulence (> 200 m), surface-layer turbulence (> 20 m), inertial subrange turbulence (> 2 m) and fine-scale turbulence (> 2 mm) (Wallace & Hobbs 2006). Turbulence can also be classified into mechanical, thermal or inertial. Mechanical turbulence results from shear in the mean wind, which can for example arise from frictional drag or wake turbulence. Thermal turbulence results from the vertical motion of warm and cold air due to buoyancy forces. Inertial turbulence refers to the smaller eddies that are generated spontaneously along the edge of larger eddies. In this process called turbulent cascade, some of the inertial energy of the larger eddies is carried away by the smaller eddies formed. The turbulence kinetic energy (TKE) of an air parcel is defined by (Wallace & Hobbs 2006)

$$\frac{\mathrm{TKE}}{m} = \frac{1}{2}\left[\overline{(u-\overline{u})^2} + \overline{(v-\overline{v})^2} + \overline{(w-\overline{w})^2}\right], \tag{1.1}$$

where m is the mass of the air parcel in turbulent motion and $\vec{u} = (u, v, w)$ is the wind velocity. By subtracting the mean wind in the kinetic energy calculation, the TKE is clearly just the part of the kinetic energy of the air parcel associated with turbulent fluctuations. Notice that each term in the square bracket in Equation (1.1) is a variance. A TKE can be associated to each eddy scale, resulting in a TKE spectrum, which is a useful description of turbulent flow. Due to molecular viscosity, TKE is continually dissipated into internal energy and is therefore not conserved. Although the dissipation mostly occurs at eddies of

the smallest scale, the entire TKE spectrum is affected due to energy cascade.

The classical idealised manifestation of the boundary layer is called the Ekman layer. The following derivation of the vertical wind profile of the Ekman layer is taken from Vallis (2017). Within the Ekman layer, a 3-way balance among Coriolis force, pressure gradient force and friction is assumed while geostrophic balance is assumed to hold beyond. It is also assumed that the Ekman layer is Boussinesq, hydrostatic balance holds in the vertical, buoyancy is constant in the horizontal and friction can be parameterised by a constant Eddy viscosity. The governing equation for the wind within the Ekman layer is then

$$f\hat{k}\times\vec{u}=-\frac{1}{\rho}\nabla_{\mathrm{h}}p+A\frac{\partial^2\vec{u}}{\partial z^2}, \tag{1.2}$$

where f is the Coriolis parameter, $\vec{u}=(u,v)$ the wind velocity, ∇_{h} the horizontal gradient, ρ the density, p the pressure and A the Eddy viscosity. The 3 terms in Equation (1.2) from left to right are the Coriolis, pressure gradient and friction term respectively. Using the definition of the geostrophic wind

$$u_{\mathrm{g}}=-\frac{1}{f\rho}\frac{\partial p}{\partial y};\qquad v_{\mathrm{g}}=\frac{1}{f\rho}\frac{\partial p}{\partial x}, \tag{1.3}$$

Equation (1.2) can be written as

$$f\hat{k}\times\left(\vec{u}-\vec{u}_{\mathrm{g}}\right)=A\frac{\partial^2\vec{u}}{\partial z^2}, \tag{1.4}$$

where $\vec{u}_{\mathrm{g}}=\left(u_{\mathrm{g}},v_{\mathrm{g}}\right)$ is the geostrophic wind. The appropriate boundary conditions are no slip at the Earth's surface and geostrophic balance beyond the Ekman layer, i.e. $\vec{u}(z=0)=\vec{0}$ and $\vec{u}(z\to\infty)=\vec{u}_{\mathrm{g}}$. Further assuming that $\partial\vec{u}_{\mathrm{g}}/\partial z=\vec{0}$, i.e. the geostrophic wind is constant in the vertical, Equation (1.4) admits the solution

$$u=u_{\mathrm{g}}-e^{-z/d}\left[u_{\mathrm{g}}\cos\left(\frac{z}{d}\right)+v_{\mathrm{g}}\sin\left(\frac{z}{d}\right)\right] \tag{1.5}$$

$$v=v_{\mathrm{g}}+e^{-z/d}\left[u_{\mathrm{g}}\sin\left(\frac{z}{d}\right)-v_{\mathrm{g}}\cos\left(\frac{z}{d}\right)\right], \tag{1.6}$$

where $d=\sqrt{2A/f}$. At the bottom, $\vec{u}$ deviates from $\vec{u}_{\mathrm{g}}$ by an angle of 45° to the left (right) in the Northern (Southern) Hemisphere. Figure 1.9 shows the vertical profile of wind speed $|\vec{u}|$ and angle of deviation with respect to $\vec{u}_{\mathrm{g}}$ in the Ekman layer.

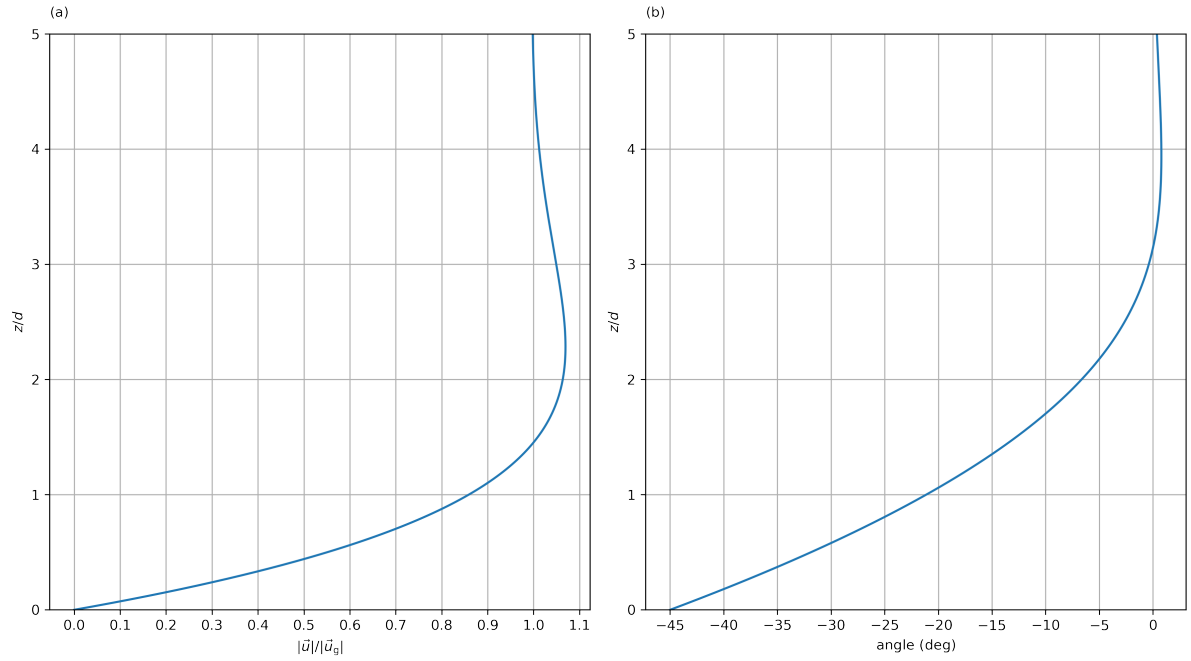


Figure 1.9: Vertical profile of (a) wind speed $|\vec{u}|$ and (b) angle of deviation with respect to $\vec{u}_g$ in the Ekman layer.

1.5 Layout of thesis

Chapter 2 briefly describes the datasets and numerical weather prediction model used in the studies presented. Short accounts on how they are used are also presented there, with further details given in the relevant sections of Chapters 3 to 6.

Chapter 3 studies the relationship between the presence of tropical cyclones in the North Atlantic and fires in the Amazon. Chen et al. (2015) pointed out that June to November Amazon fires, March to June North Atlantic sea surface temperature anomalies and the number of annual North Atlantic tropical cyclones are all correlated to one another. They concluded from a Monte Carlo analysis that the correlation between fires and tropical cyclones cannot be fully explained by assuming only a common linkage of the two with the sea surface temperature. Chapter 3 addresses the question whether the presence of tropical cyclones in the North Atlantic contributes to the occurrence of fires in the Amazon, and if so what is the physical mechanism behind.

Chapter 4 explores whether long-range prediction of atmospheric responses driven by ENSO can be achieved via subsurface temperature signals in the Pacific basin. It is well-known that the ENSO cycle consists of a subsurface branch and that the mature surface state is preceded by changes in the ocean heat content which can be up to 18 months

in advance (e.g. Timmermann et al. 2018, Ramesh & Murtugudde 2013, Ballester et al. 2016). In fact, subsurface temperature signals have been successfully incorporated into statistical predictions of the ENSO oceanic surface state (e.g. Drosdowsky 2006, Petrova et al. 2017, 2020). It is then natural to ask if the prediction of atmospheric responses driven by the surface ENSO state can be extended to longer lead-times by exploiting the subsurface branch of the ENSO cycle. Based on Sparks & Toumi (2020), who showed that tropical cyclone landfall in South China can be predicted using the subsurface temperature anomaly under the Niño4 region with a lead-time of 1 year, a new SubNiño4 index is constructed and assessed for its potential as a long-range predictor of ENSO and ENSO-driven atmospheric responses generally.

Chapter 5 assess the effects of intensity change and surface friction on the boundary layer wind profile of weak tropical cyclones near landfall. Previous studies on the effects of surface properties (Zhang & Uhlhorn 2012, Zhang, Li, Perrie & Zhang 2021), intensity change (Rogers et al. 2013, Liao et al. 2019, He et al. 2022) and landfall (Powell 1982, Knupp et al. 2006, Hlywiak & Nolan 2022) have focused on relatively strong systems. Chapter 5 seeks to identify the dominating factor affecting the boundary layer profile of weak tropical cyclones near landfall and any difference in their behaviour to strong systems.

Chapter 6 investigates the re-intensification and structural evolution of tropical cyclones re-entering ocean after making landfall. In general, a tropical cyclone weakens following landfall as it is cut off from the supply of heat and moisture from the ocean and experiences enhanced surface friction. However, such a perturbed system can re-intensify upon re-entering ocean, as is seen regularly in both the Pacific and Atlantic basins. This has not been thoroughly explored by existing works in the literature. Chapter 6 addresses the question what is the baseline structural evolution tropical cyclones go through as they re-enter ocean from land.

Chapter 7 summarises the major findings in all of the works presented in this thesis, discusses their relevance to the atmospheric science research community in general and outlines possible avenues of study, based on the results presented, that may be worthy of undertaking in the future.

Chapter 2

Data and methods

2.1 European Centre for Medium-Range Weather Forecasts Reanalysis version 5 dataset

The European Centre for Medium-Range Weather Forecasts Reanalysis version 5 (ERA5) dataset (Hersbach et al. 2020) is produced by the Copernicus Climate Change Service (C3S) at the European Centre for Medium-Range Weather Forecasts (ECMWF). ERA5 provides global estimates of a comprehensive set of atmospheric, land and oceanic climate variables by combining vast amounts of satellite, aircraft, radiosonde, land station, ship station, radar and buoy observation data from agencies around the world using advanced modelling and data assimilation techniques. The model covers the entire globe on a 31 km horizontal grid with 137 vertical levels form the surface up to an altitude of 80 km. In addition to the 137 model levels, the resulting data is also available on 37 pressure levels from 1000 hPa to 1 hPa, 16 potential temperature levels from 265 K to 850 K, and single levels. The temporal coverage of ERA5 is from 1940 to present at hourly resolution. Daily and monthly aggregates of the hourly data are also available. In Chapter 3, the zonal and meridional wind at 850 hPa and 200 hPa, and vertical velocity at 600 hPa are taken from ERA5 monthly averaged data on pressure levels (Hersbach et al. 2019*a*); and the sea surface temperature, mean surface downward shortwave radiation flux and precipitation are taken from ERA5 monthly averaged data on single levels (Hersbach et al. 2019*b*). In Chapter 4, the surface zonal wind stress data are the eastward turbulent surface stress taken from ERA5 monthly averaged data on single levels (Hersbach et al. 2019*b*).

The ensemble uncertainties in ERA5 are small. For example, between the 9 ensemble members and the control member, the uncertainties in temperature, relative humidity and zonal wind at the 500 hPa pressure level for 2018 are 0.006 K, 0.3% and 0.4 cm s^{-1} respectively, with values of a similar magnitude found for 1980 (Hersbach et al. 2020). This however only shows that the reanalysis model in ERA5 is well-behaved and robust against random errors in the input observation datasets and is also related to the quality of the observations themselves. Such ensemble uncertainties are not representative of the actual uncertainties of ERA5 around the true state of the atmosphere at any given time. ERA5 uses an incremental 4-dimensional variational data assimilation technique (Courtier et al. 1994) to minimise the reanalysis output variables' departure from observations to meet the goal of providing the most accurate representation of the actual hourly state of the global atmosphere. The ERA5 dataset has been verified against several observation datasets (Hersbach et al. 2020). However, this is somewhat circular because given the scope of observation datasets used to produce ERA5, it is almost certain that any credible observation dataset that could be reasonably chosen for verification has already been incorporated into ERA5 one way or the other and hence not completely independent. Nevertheless, it can be said that ERA5 gives a best hourly estimate of the comprehensive state of the atmosphere consistent with both observations and reanalysis model physics.

Notwithstanding the above, ERA5 contains systematic errors intrinsic to its production algorithm. The model constraint ensures smooth hourly products within any of the 12-hour windows used for data assimilation at the cost of possibly introducing systematic jumps at the transition points in between (Hersbach et al. 2020). For example, the 10 m wind speed over Paris, France at 10:00 UTC exhibits a jump of around 0.25 m s^{-1} on average. However, when considering interannual variabilities, such systematic errors that affect all data points equally do not affect the correlation or composite analysis performed. It is also known that the resolution of ERA5 is not sufficient to properly describe tropical cyclones, leading to a higher than actual minimum pressure although the area in pressure deficit with the environment corresponds well with the actual shape of the cyclone in general (European Centre for Medium-Range Weather Forecasts 2023). This, however, is not a point of concern for this thesis as ERA5 is not used for studying the structural details or intensity of tropical cyclones but large scale circulations in the atmosphere.

2.2 Moderate Resolution Imaging Spectroradiometer Collection 6 Active Fire Products

The Moderate Resolution Imaging Spectroradiometer (MODIS) Collection 6 Active Fire Products (Giglio et al. 2016, 2020) are produced by the National Aeronautics and Space Administration (NASA) using measurements taken by the MODIS onboard the Terra and Aqua satellites. Out of the entire collection, the 2 products MCD14ML and MOD14CMQ are used in this thesis. The MCD14ML product contains information for each individual fire pixel detected by both the Terra and Aqua satellites. It includes the date, time and satellite of detection and the geographic coordinates, detection confidence and inferred type of the fire pixel. Although the MCD14ML product is available from 2001 to 2022, Aqua record is not available until July 2002. Only fire pixels detected by the Terra satellite are considered throughout this thesis. The fire pixels recorded in the MCD14ML product are filtered to keep only those detected by the Terra satellite in the region of interest and classed as "presumed vegetation fire" with a detection confidence of at least 30% (normal to high confidence). These fire pixels are then adjusted for the cloud coverage recorded in the MOD14CMQ product according to Giglio et al. (2006). The MOD14CMQ product contains monthly data from the Terra satellite covering the entire globe with a spatial resolution of 0.25° and is available from 2001 to 2018. This procedure results in a monthly time series of fire count over an area of interest as the total number of cloud cover-adjusted fire pixels over that region from 2001 to 2018. In Chapter 3, the MODIS fire count is used to locate the most fire-active region over the Amazon and for correlation analysis. In Chapter 4, the MODIS fire count is used to locate the most fire-active region over both Continental and Maritime Southeast Asia.

Terra MODIS active fire products have been validated against coincident, high resolution fire masks derived from the Advanced Spaceborne Thermal Emission and Reflection Radiometer (ASTER) imagery (Giglio et al. 2020, Schroeder et al. 2008). For fires reaching 100 30 m resolution ASTER active fire counts, the MODIS detection probability is at least 80% (Schroeder et al. 2008). MODIS is capable of routinely detecting fires reaching 1000 m^2 of size, lowering to 100 m^2 and 50 m^2 under very good and pristine observing conditions. For instance, a fire can go undetected by MODIS due to cloud cover. However with correction in place and a focus on interannual variation over a fixed season and hence

largely similar observing conditions, this should not pose a major concern. On the other hand, some non-fire pixels are inevitably flagged as fire pixels by the MODIS fire detection algorithm. Therefore, fire pixels with a detection confidence below 30% (low confidence fire) are excluded.

2.3 Fire danger indices historical data from the Copernicus Emergency Management Service

The Copernicus Emergency Management Service for the European Forest Fire Information System (EFFIS) produces fire danger indices and relevant intermediate variables (Copernicus Climate Change Service, Climate Data Store 2019, Di Giuseppe et al. 2016) from 3 different fire danger rating systems using ERA5 data as input. The 3 fire danger rating systems are the American National Fire Danger Rating System (NFDRS), the Canadian Fire Weather Index (FWI) System and the Australian McArthur's Forest Fire Danger Meter (Mark 5). The dataset covers the entire globe daily from 1940 to present with a spatial resolution of 0.25°. Di Giuseppe et al. (2016) showed that among the 3 systems, the FWI gives the best dependency index skill score in the regions studied in this thesis. The FWI depends on local noon relative humidity, temperature and wind speed among others (see Figure 1.6). In Chapter 3, the seasonal FWI time series for Amazon is obtained for correlation analysis. In Chapter 4, the seasonal FWI time series for both Continental and Maritime Southeast Asia are obtained for correlation analysis.

Since the EFFIS produced FWI is a direct application of the FWI System on ERA5 data, its uncertainty results solely from carrying over ERA5 uncertainties. The use of the FWI to extend the period of analysis into pre-MODIS era is supported by the high correlation found between the FWI and MODIS time series over the MODIS era for the regions studied.

2.4 Tropical Rainfall Measuring Mission dataset

The Tropical Rainfall Measuring Mission (TRMM) (National Aeronautics and Space Administration 2017) was jointly run by NASA and the Japan Aerospace Exploration Agency (JAXA) (previously the National Space Development Agency of Japan (NASDA), until 2003). The TRMM 3B43 product (Tropical Rainfall Measuring Mission (TRMM) 2011) provides the

best estimates of monthly precipitation within the latitude band between 50° S to 50° N, covering both the tropics and the sub-tropics, using measurements from the precipitation radar and TRMM microwave imager onboard the TRMM satellite calibrated by rain gauge data. The TRMM 3B43 data has a spatial resolution of 0.25° and is available from 1998 to 2019. In Chapter 3, the precipitation is taken from the TRMM 3B43 version 7 product. The seasonal time series of precipitation over the Atlantic ITCZ and Caribbean are further obtained for correlation analysis.

Previous version of TRMM tends to underestimate precipitation over land but such bias is expected to have been reduced in the current version (Iguchi et al. 2009). The current version of TRMM has been validated well, albeit somewhat low, against Pacific Ocean atoll rain gauges (Huffman & Bolvin 2018). This can be expected at other tropical ocean basins as well. Rauniyar et al. (2017) showed that over the Maritime Continent, uncertainties are higher over land compared to ocean. Climatological calibrations applied as part of the production of TRMM products "might change the mean bias or even the seasonal cycle, but they should not change the interannual variations or long-term trends" (Huffman & Bolvin 2018). Although the focus of Chapter 3 is on interannual variations, the accuracy in representing precipitations over ocean dominated regions in the Atlantic basin with TRMM data is arguable and hence results derived therefrom shall be interpreted with caution. If only TRMM data were used for precipitations in the analysis in Chapter 3, the results would indeed be somewhat questionable. This problem is however mitigated by the fact that ERA5 precipitations are also used in Chapter 3 and produced consistent results.

2.5 Global Precipitation Climatology Project dataset

The Global Precipitation Climatology Project (GPCP) (Huffman et al. 1997) is part of the Global Energy and Water Cycle Exchanges (GEWEX) programme under the World Climate Research Programme (WCRP) jointly sponsored by the World Meteorological Organization (WMO), the Intergovernmental Oceanographic Commission (IOC) of the United Nations Educational, Scientific and Cultural Organization (UNESCO) and the International Science Council (ISC) (previously the International Council for Science (ICSU), until 2018). The GPCP Monthly product (Adler et al. 2018, 2016) provides the best estimates of global monthly precipitation by combining satellite datasets of microwave and infrared measure-

ments and outgoing longwave radiation retrievals over land and ocean and rain gauge observations over land. The GPCP Monthly data has a spatial resolution of 2.5° and is available from 1979 to present. In Chapter 4, the seasonal time series of precipitation over the Maritime Continent, Northeast Brazil, Gulf of Guinea, Sahel, South Africa and East Africa are obtained from the GPCP Monthly product.

Gebremichael et al. (2003) evaluated the performance of the GPCP product against rain gauge measurements at 3 sites, 2 in North Dakota and 1 in Thailand, with densely populated rain gauges. They found that the correlation coefficients between the GPCP estimates for all 3 sites and the corresponding gauge measurements exceed 0.85. Furthermore, GPCP does not exhibit any significant bias for the 2 North Dakota sites but over-estimates rainfall at the Thailand site by 29%. However, it should be noted that the over-estimate at the Thailand site could be an artefact due to the number of gauges involved in the GPCP estimate for that region. Li et al. (2023) assessed the performance of GPCP over the global ocean against observations by 58 Passive Aquatic Listeners (PALs). The multi-year mean rain rates from GPCP have a root mean square error of $1.42\,\mathrm{mm\,day^{-1}}$ and a correlation coefficient of 0.89 with PAL observations. GPCP performs well in capturing the monthly mean and spread of and correlating with the PAL observed rainfall in the tropical Northeast Pacific, tropical Northwest Pacific, tropical North Indian Ocean and subtropical North Atlantic. However, it deviates noticeably from observed seasonal behaviour in the tropical Southeast Pacific and extratropical North Pacific and gives low correlations with observations there. Among the regions whose seasonal time series of precipitation is taken from GPCP in Chapter 4, most are near regions where GPCP performs well and none is close to the problematic ones. Therefore, it is expected that the use of GPCP here should give reasonable and credible results.

2.6 Indian Institute of Tropical Meteorology rainfall dataset

The Indian Institute of Tropical Meteorology (IITM) produced monthly, seasonal and annual rainfall time series for all-India, homogeneous regions and meteorological subdivisions from 1871 to 2016 (Kothawale & Rajeevan 2017). Rainfall measurements from 306 stations spread uniformly throughout India are used to produce the monthly rainfall time series for 30 meteorological subdivisions. The monthly rainfall time series for 5 homogeneous re-

gions and all-India are then given as the area weighted averages of the monthly rainfall time series of the meteorological subdivisions composing the concerned area. The seasonal and annual rainfall time series are produced from the monthly versions. In Chapter 4, the seasonal time series of precipitation over India is obtained from the IITM monthly rainfall time series for all-India.

The IITM dataset is based solely on measurements taken by a set of carefully selected ground stations and can thus be taken as the ground truth with the following caveats in the treatment of potential outliers. Monthly rainfall values that deviate from the reporting station's long term mean by more than 4 times the standard deviation are flagged as potential outliers. These are checked against the corresponding Indian Daily Weather Reports (IDWR) value and replaced as appropriate. If the flagged outlier is reported by a station not covered by the IDWR, the value is checked against values from surrounding stations along with percentage departure from the corresponding subdivisional value and replaced by interpolation as appropriate. Furthermore, a very limited number of stations reported no rainfall during the monsoon season from June to September. These data points are also treated by the procedure outlined above. Uncertainties introduced this way into the IITM monthly rainfall time series for all-India should have negligible effects for the study here.

2.7 Hadley Centre Sea Ice and Sea Surface Temperature dataset

The Hadley Centre Sea Ice and Sea Surface Temperature (HadISST1) dataset (Rayner et al. 2003) is produced by the Hadley Centre of the UK Met Office (UKMO) in collaboration with UKMO, the National Oceanography Centre, Southampton and the Lamont-Doherty Earth Observatory of Columbia University. The HadISST1 dataset provides the best estimates of global monthly sea ice and sea surface temperature by combining a number of datasets with satellite and in situ measurements. The HadISST1 data has a spatial resolution of 1° and is available from 1871 to present. In Chapter 4, the time series of the Niño3.4 index is obtained from the HadISST1 dataset by averaging over the Niño3.4 region (170° W–120° W, 5° S–5° N).

The HadISST1 dataset is temporally homogeneous and consistent based on the global root mean square average standard deviation of 1° area grid box time series (Rayner et al.

2003). It also gives persistent detrended sea surface temperature anomalies between 1982 and 1999, with 1-month lagged autocorrelation exceeding 0.8 in much of the tropics (Rayner et al. 2003). The use of reduced space optimal interpolation (Kaplan et al. 1997) allowed increased data coverage without compromising the real variability of the original observed data (Rayner et al. 2003). The ensemble mean time series of the Southern Oscillation Index simulated in the HadAM3 (Pope et al. 2000) atmosphere-only general circulation model forced with HadISST1 produced a correlation of 0.59 with the observed time series (Rayner et al. 2003). Chelton & Risien (2016) found that the standard deviations of sea surface temperature anomalies in HadISST1 are 0.2 °C to 0.4 °C larger after 1949 compared to prior. This nonstationarity does not concern the study in Chapter 4 as the period of study is entirely after 1949. Chelton & Risien (2016) also found zonal (meridional) discontinuities at regular interval of 2° post-1949 in the zonal (meridional) first difference of sea surface temperature with zonally (meridionally) oscillating striations in standard deviation at a typical amplitude of about 0.05 °C. This manifests as a chequerboard pattern in the standard deviation of the temperature field itself albeit subtle in magnitude. Nonetheless, the authors concluded that despite such artefacts in the HadISST1 dataset, it is still suitable for studies of large-scale signals associated with short-term climate variability from interannual to decadal time scales. Therefore, the HadISST1 dataset can be used for the study of ENSO in Chapter 4.

2.8 Hadley Centre "EN" series version 4 dataset

The Hadley Centre "EN" series version 4 (EN4) dataset (Good et al. 2013) is produced by the Hadley Centre of UKMO. The EN4 dataset provides the best estimates of global monthly subsurface ocean temperature and salinity profiles by combining a number of datasets. The EN4 dataset has a horizontal spatial resolution of 1° with 42 vertical levels from 5 m to 5350 m below sea level and is available from 1900 to present. The EN4 dataset comes with 4 different sets of bias corrections. The version EN.4.2.2 with Gouretski & Reseghetti (2010) XBT and Gouretski & Cheng (2020) MBT corrections is used in this thesis. Each subsurface potential temperature data entry has an accompanying observation weight between 0 and 1 to indicate the relative contribution from observations. In Chapter 4, the time series of the SubNiño4 index is obtained from the EN4 dataset by averaging over the Niño4 region

(160° E–150° W, 5° S–5° N) and between the depths of 100 m and 300 m.

The EN4 dataset uses an optimal interpolation algorithm and is not based on physical models but observed profiles and background fields only (Killick 2021). If observations are persistently absent, the background fields are relaxed to climatology. Since no physical model is involved in its curation, uncertainties in the EN4 dataset result mainly from the quality of observations. The dataset takes into account bias corrections for the XBT and MBT probes. On the other hand, the number of observation profiles have changed over time, in particular there has been an appreciable increase since 1940 (Killick 2021). To reflect this, the EN4 dataset provides an observation weight associated with each data point. The observation weight describes the relative influence of observations and climatology and ranges from 0 to 1, with 0 meaning no observation. To ensure consistency and limit uncertainties, Chapter 4 focuses on the period starting from 1960, since when the average observation weight for the region described in the previous paragraph stays consistently above 0.8 in general.

2.9 International Best Track Archive for Climate Stewardship dataset

The International Best Track Archive for Climate Stewardship (IBTrACS) dataset (Knapp et al. 2010, 2018) is curated by the National Oceanic and Atmospheric Administration (NOAA) National Centers for Environmental Information (NCEI) with data provided by the World Meteorological Organization (WMO) Regional Specialized Meteorological Centres (RSMCs) and Tropical Cyclone Warning Centres (TCWCs) and a few other agencies around the globe. The major contributors are:

- NOAA National Hurricane Center (NHC) [RSMC Miami]
- Japan Meteorological Agency (JMA) [RMSC Tokyo]
- India Meteorological Department (IMD) [RSMC New Delhi]
- Météo-France [RMSC La Réunion]
- Fiji Meteorological Service (FMS) [RSMC Nadi]

- NOAA Central Pacific Hurricane Center (CPHC) [RSMC Honolulu]
- Australian Bureau of Meteorology (BOM) [TCWC Melbourne]
- Meteorological Service of New Zealand, Ltd. (MetService) [TCWC Wellington]
- China Meteorological Administration (CMA)
- Hong Kong Observatory (HKO)
- US Department of Defense Joint Typhoon Warning Center (JTWC)

IBTrACS contains records of the nature, location, maximum sustained wind speed, central pressure and distance to land of tropical cyclones. Depending on the reporting agency, further information regarding the tropical cyclone's size and intensity category may also be available. The IBTrACS data is mostly 6-hourly (3-hourly with interpolation) and covers the entire globe. It is available from the time of first record to present. The earliest record for each ocean basin are:

- North Indian: 25 October 1842
- South Indian: 11 January 1848
- North Atlantic: 23 June 1851
- East Pacific: 29 September 1876
- West Pacific: 24 June 1884
- South Pacific: 4 January 1897
- South Atlantic: 25 March 2004

In Chapter 3, the time and location of tropical cyclones present in the North Atlantic basin from 1980 to 2019 are obtained from the IBTrACS dataset. Only cyclones with 1-minute maximum sustained wind of 34 kt above, i.e. systems classified as tropical storm or above on the Saffir-Simpson hurricane wind scale, are considered. In Chapter 5, for each tropical cyclone in the Hong Kong Observatory wind profiler dataset (see Section 2.10), the radius of maximum wind speed (R_{max}), 1-minute maximum sustained wind speed (V_{max}), coordinates of the cyclone centre and its distance to land at regular 6-hour interval are taken from the

IBTrACS dataset. These are then linearly interpolated to 10-minute time steps to match with the Hong Kong Observatory data. The translation speed (V_{trans}) and direction of the cyclones are further obtained from the interpolated coordinates. The interpolated coordinates are also used to compute the distance R between the cyclone centre and the weather station, which is then normalised by the interpolated R_{max} to give $r = R/R_{\text{max}}$.

In IBTrACS' Technical Documentation (Knapp 2019), estimates of uncertainties in storm intensity and position are given. For the periods and basins concerned, the uncertainty in V_{max} is estimated to be around 10 kt; while that in position is 30–40 km ($V_{\text{max}} < 60$ kt), 20–25 km ($60 \leq V_{\text{max}} < 100$ kt) and 10–15 km ($V_{\text{max}} \geq 100$ kt). These uncertainties take into account discrepancies among agencies. In both Chapter 3 and Chapter 5, only data from US agencies are considered. Hence the uncertainties can be expected to be less, although a lower bound of about 10 km uncertainty in position always applies due to reporting resolution. V_{max} is used in Chapter 3 to filter storms that are too weak and in Chapter 5 to classify storms based on intensity. Uncertainty in V_{max} only affects the classification of borderline cases and the impact on the analysis should be minimal. In Chapter 3, the entire track of a storm is used to determine whether it entered the Caribbean region (88° W–52° W, 10° N–25° N) throughout its lifetime. Given the size of the Caribbean region and that the entire lifetime of the storm is considered, the impact of uncertainty in position is negligible to the study. In Chapter 3, the calculations of inflow angle, radial velocity and V_{trans} rely on the storm position. An uncertainty of 30 km in storm position results in around 13° uncertainty in inflow angle at a distance of 100 km and around 1 m s^{-1} uncertainty in V_{trans}. Although these uncertainties are appreciable, they are not large enough to invalidate the conclusions of the study.

2.10 Hong Kong Observatory wind profiler dataset

Measurements of boundary layer zonal and meridional wind velocities by a wind profiler fitted at the Sha Lo Wan weather station (113.9° E, 22.3° N) in the north of Lantau Island, Hong Kong are provided by the Hong Kong Observatory (HKO). The wind profiler measures the wind velocity throughout the boundary layer directly above it with a vertical resolution of about 50 m at regular 10-minute intervals. Detailed description on the working principle of the wind profiler can be found for example in Tse et al. (2013). Measurements at each

altitude and each time step are quality controlled. Data from days with tropical cyclones near Hong Kong are available from 2010 to 2019. Due to a system replacement in Spring 2016, the measurement altitudes before and after are slightly shifted. To combine data from the 2 periods, measurements at each actual measurement altitude are treated as being measured at the nearest 50 m between 200 m and 1400 m inclusive.

This dataset is analysed in Chapter 5. Only those data deemed valid by HKO's internal quality control algorithm taken from landfalling ($r < 4$) cyclones reaching at least tropical storm intensity on the Saffir-Simpson hurricane wind scale ($V_{\text{max}} \geq 34\,\text{kt}$) at the time of measurement based on the interpolated IBTrACS data are considered. It is further required that the wind speed at the top of the boundary layer is at least $4V_{\text{trans}}$, the reason for this is explained below. Note that the condition set for landfalling is rather strong in the sense that it is based on the distance from the weather station rather than the closest distance from land. This has the added benefit of ensuring that all measurements considered are made relatively close to the cyclone centre. Kepert (2001) provided an analytical solution for the inner core of translating tropical cyclones under a linear model and showed that inertially less stable cyclones have larger depth scales. The linearisation requires the cyclone translation speed to be much smaller than the gradient level flow (the K01 criterion). In the approach presented by Shapiro (1983), relatively slow translation of the cyclone is also necessary for the linearisation there to hold. The relative magnitude between cyclone translation speed and tangential wind speed is not a main point of concern if relatively strong cyclones are considered as the latter is always high. However, Chapter 5 focuses on relatively weak cyclones, and thus only data taken when the K01 criterion is met are considered.

2.11 Weather Research and Forecasting model

The Weather Research and Forecasting (WRF) model is a state-of-the-art mesoscale numerical weather prediction system developed by the concerted efforts of the National Center for Atmospheric Research (NCAR), the National Centers for Environmental Prediction (NCEP) and the Earth System Research Laboratory of NOAA, the U.S. Air Force, the Naval Research Laboratory, the University of Oklahoma and the Federal Aviation Administration (FAA). WRF is designed for both atmospheric research and operational forecasting applications

and may be configured with either the Advanced Research WRF (ARW) or Nonhydrostatic Mesoscale Model (NMM) dynamic core. Unlike WRF-ARW, WRF-NMM is no longer in active development.

WRF-AWR (Skamarock et al. 2021) solves a set of fully compressible, nonhydrostatic Eulerian equations cast in flux form by integrating forward in time using third-order Runge-Kutta method starting from a given initial condition and obeying lateral boundary conditions at every time step. The horizontal gird employs Arakawa C-grid staggering; while the vertical coordinate is terrain-following, using a mass-based hybrid sigma-pressure formulation based on dry hydrostatic pressure, with the model top being a constant pressure surface. For physical processes that cannot be resolved explicitly due to insufficient spatial resolution, WRF-AWR allows capturing them by the employment of a selection of different parameterisation schemes. Microphysics, cumulus, surface physics, planetary boundary layer physics and atmospheric radiation physics are covered.

In Chapter 6, the WRF-AWR model is used to run idealised simulations of tropical cyclones re-entering ocean after spending time over land to study their structural evolution. 2 nested square domains with 2-way interactions on an f-plane of a fixed latitude are used. The inner domain with 802-by-802 grid cells and 3.999 km grid spacing (3207.198 km side length) is embedded in the outer domain with 600-by-600 grid cells and 11.997 km grid spacing (7198.2 km side length). The 2 domains are centre-aligned and both have 45 vertical levels, around 12 of which are below 2 km. The time steps of the inner and outer domains are 10 s and 30 s respectively.

An initial bogus vortex described by a near-surface tangential wind speed profile of the form (Wang & Toumi 2019)

$$V_0(r) = \frac{\sqrt{2}}{0.77}\left(V_{0,\max} + \frac{f R_{0,\max}}{2}\right)\sqrt{\frac{1-\exp[-\Phi(r)]}{\Phi(r)} - \exp[-\Phi(r)]} - \frac{f r}{2}, \tag{2.1}$$

where

$$\Phi(r) = \frac{r^2}{0.56 R_{0,\max}^2}, \tag{2.2}$$

r is the radius from the vortex centre, f the Coriolis parameter corresponding to the f-plane latitude of the domains, $V_{0,\max}$ the initial maximum near-surface wind speed and $R_{0,\max}$ the initial radius of maximum near-surface wind speed, is introduced into the model at the centre of the domains at the start. The initial bogus vortex is given a cyclonic sense of rota-

tion and the wind speed tapers off linearly upwards from $V_0(r)$ near the surface to 0 at an altitude of around 17 km. The initial environmental conditions and lateral boundary conditions are given by the Jordan mean tropical sounding during hurricane seasons (Jordan 1958). No background wind is introduced into the model.

A full suite of physics parameterisations is used, including the WRF single-moment 6-class (WSM6) microphysics scheme (Hong & Lim 2006), the Rapid Radiative Transfer Model for general circulation models (RRTMG) scheme (Iacono et al. 2008) for both shortwave and longwave radiations, the Yonsei University (YSU) planetary boundary layer scheme (Hong et al. 2006), and the revised fifth-generation Pennsylvania State University-National Center for Atmospheric Research Mesoscale Model (revised MM5) Monin-Obukhov similarity surface layer scheme (Jiménez et al. 2012) with a 5-layer thermal diffusion land-surface model. As the inner domain grid size of 3.999 km is fine enough to encapsulate most of the structure of the simulated tropical cyclones, neither domain employed any cumulus scheme.

The chosen combination of physics parameterisations has previously been successfully implemented in idealised WRF-AWR simulations for studying the structure of tropical cyclones under various circumstances (e.g. Wang & Toumi 2019, 2022). It is based on the NCAR Tropical Suite, which according to WRF-AWR's User's Guide (Wang et al. 2022) is suitable for tropical cyclone simulations and "ha[s] been highly tested and ha[s] shown reasonable results". Khaira & Astitha (2023) carried out sensitivity experiments by running the WRF-AWR model with two different sets of physics parameterisations, one of which being the NCAR Tropical Suite, to forecast 4 tropical storms — Isaias (2020), Irene (2011), Henri (2021) and Elsa (2021) — impacting Northeast United States. The performances were evaluated against wind speed and wind gust observed by a set of ground stations, NCEP stage IV quantitative precipitation estimates as well as storm track and intensity published by the NHC. The NCAR Tropical Suite shows overall improvement in all performance evaluation metrics in their study. In particular, it produced a better confined band of high precipitation and reduced the shift in storm track by up to 38 km. The two sets of physics parameterisations produced similar minimum mean sea level pressure, wind speed and wind gust. Hence, rather than the storm intensity per se, the improvement in the predicted wind speed and wind gust by the use of the NCAR Tropical Suite is mostly related to improved spatial distribution of the winds. Apparently, the NCAR Tropical Suite better captures the

structural details of tropical cyclones in general.

Chapter 3

Hurricanes as an Enabler of Amazon Fires

3.1 Introduction

South America, together with equatorial Asia, are the 2 major regions contributing to global net fire carbon emission (van der Werf et al. 2010). High-frequency fires have also been shown to impact the unique ecological structure and biodiversity in the Amazon (Cury et al. 2020). The drivers of fires in the Amazon region have gained much interest (Fernandes et al. 2011, Chen et al. 2011, 2013). It is well known that Amazonian fires are ignited by humans (Berenguer et al. 2021, Barlow et al. 2020, Aragão et al. 2018) and are thus not purely meteorological events. In this chapter, the meteorological conditions that enable fires and are thus a cause of interannual variability are the principal concern. Chen et al. (2011) proposed an empirical seasonal prediction model for the total fire count from May onwards using North Atlantic sea surface temperature (SST) during the boreal spring. Fernandes et al. (2011) studied the relationships among West Amazon fires and precipitation (76° W–70° W, 14° S–3° S) from July to September and North Atlantic SST in the preceding months. These predictions are based on the prevailing understanding that anomalously high tropical North Atlantic SST relative to the tropical South Atlantic results in a northward shift of the Atlantic Intertropical Convergence Zone (ITCZ) (Enfield 1996, Moron et al. 1995) and thus reduces the amount of precipitation the Amazon receives (Yoon 2016, Yoon & Zeng 2010, Zeng et al. 2008). Yoon & Zeng (2010) showed that the North Atlantic SST correlates with the mean precipitation of the whole Amazon catchment throughout the year, except

in the height of the boreal winter. However this area is much larger than the active fire region. Reduced Amazon precipitation is thought to promote fire activities there (Chen et al. 2015, Fernandes et al. 2011, Chen et al. 2011). These studies have focused on seasonal prediction and still leave open the question on the direct physical link between the Atlantic and Amazon fires during the actual fire season. This study attempts to answer the question whether the presence of tropical cyclones in the North Atlantic contributes to the occurrence of fires in the Amazon, and if so what is the physical mechanism behind.

SST affects tropical cyclone activities and properties. An increase in SST increases water vapour in the lower troposphere, both of which make more energy available for atmospheric convection and tropical cyclone development (Trenberth 2005). The intensity and the number of tropical cyclones in the North Atlantic could increase with increasing tropical North Atlantic SST (Emanuel 2005, Webster et al. 2005). Dynamical factors are also important as tropical cyclone genesis and intensification are favoured by weak vertical wind shear (Gray 1968), low-level cyclonic circulation (Maloney & Hartmann 2000) and a weakening of the easterly trade wind over the Caribbean (Inoue et al. 2002).

Chen et al. (2015) identified a relationship between June to November Amazon fires, and earlier (March to June) North Atlantic SST anomalies and the number of annual North Atlantic tropical cyclones. Intriguingly, they showed that the correlation between fires and tropical cyclones is actually greater than that between SST and either fires or tropical cyclones. They performed a Monte Carlo analysis and concluded that the correlation between fires and tropical cyclones cannot be fully explained by assuming only a common linkage of the two with the SST. However, they did not identify other possible causes or explanations. This study suggests that rainfall associated with tropical cyclones in the Caribbean could play an active role in promoting Amazon fire conditions and the direct role of SST is actually minor. The anomalous precipitation and associated latent heating in the Caribbean due to tropical cyclones can provide a direct physical link between North Atlantic tropical cyclones and Amazon fires through a thermally direct circulation anomaly.

3.2 Methods

To investigate the relationship between the North Atlantic basin and the Amazon, focus is put on the following 3 regions: the South Amazon (69° W–49° W, 15° S–5° S), which

captures the most fire-active region of the Amazon; the August to October (ASO) Atlantic ITCZ (48° W–17° W, 2° N–13° N), which captures the region of maximum precipitation over the North Atlantic in ASO; and the Caribbean (88° W–52° W, 10° N–25° N), which covers the region with significant precipitation difference between years of Amazon fire extremes. The fire count, FWI, subsidence, surface solar radiation flux and precipitation over the Amazon; the tropical cyclone count and precipitation over the Caribbean; and the precipitation over the ASO Atlantic ITCZ are obtained for analysis.

North Atlantic SST is averaged over the region 90° W–15° W and 0° N–25° N. Horizontal wind at 850 hPa and 850 hPa-200 hPa vertical wind shear over the North Atlantic are also studied for patterns favourable to the genesis and development of tropical cyclones. Composite differences over the periods from 2001 to 2018 and from 1980 to 2019 are taken between the top and bottom 5 and 13 extreme years respectively, corresponding roughly to the top and bottom terciles. The resulting anomalies are considered significant if their 95% confidence intervals produced by bootstrapping do not bracket 0. The number of bootstrap resamples used for the maps and box averages are 1000 and 10000 respectively. All correlation coefficients are Pearson correlation coefficients. Unless otherwise specified, correlation analysis are performed on linearly detrended time series to eliminate long term effects such as global warming. This is achieved by subtracting the linear least squares fitted linear signal from the original time series. Non-detrended correlation results are reported only if the p-value indicates a change in the level of significance across 99% and 95% confidence. In particular, there are in total 3 correlations that move from significant to non-significant ($p > 0.05$) and thus may be considered less robust than those that are significant irrespective of detrending.

3.3 Results

3.3.1 Seasonal cycles of storms and fires

The annual fire count in northern South America is shown in Figure 3.1 (a), from which the most fire-active region in the Amazon is identified. Figure 3.1 (b) shows the seasonal cycles of North Atlantic tropical cyclone number and Amazon fire count from 2001 to 2018. The seasonal cycles of storm and fire are in phase with a clear maximum in September. The 3 months from August to October (ASO) account for more than 75% of North Atlantic

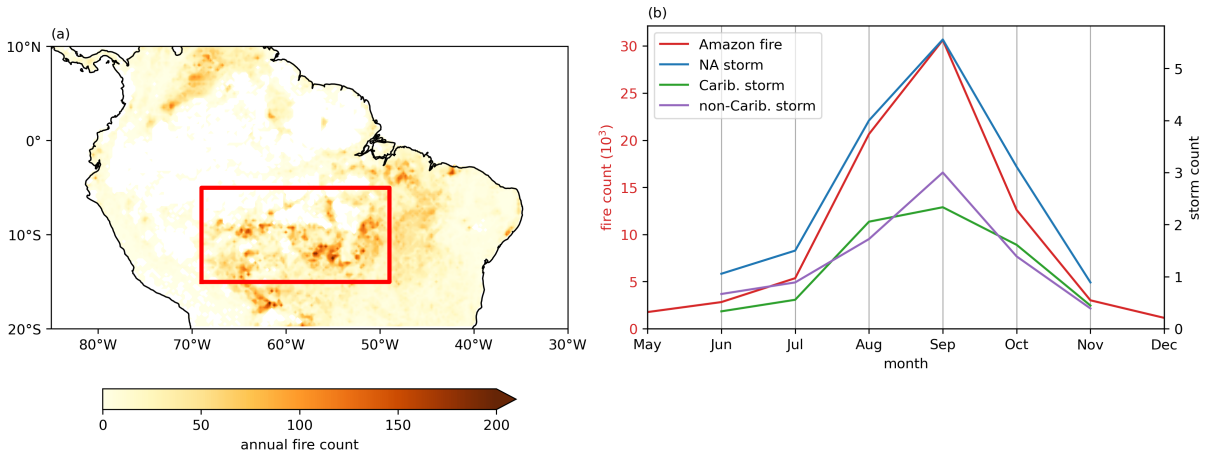


Figure 3.1: (a) Average annual fire count of northern South America between 2001 and 2018. The red box is the most fire-active region. (b) Seasonal cycles of Amazon fire count and North Atlantic (NA), Caribbean (Carib.) and non-Caribbean (non-Carib.) tropical cyclone number computed from 2001 to 2018.

tropical cyclone count, Caribbean storm count, non-Caribbean storm count (count of North Atlantic storms that did not enter the Caribbean box) and Amazon fire count throughout the year. Figure 3.2 shows scatter plots with linear least square fits for ASO Amazon fire count against both Caribbean and non-Caribbean ASO tropical cyclone number. Correlation analysis reveal significance between Amazon fire count and North Atlantic ($r = 0.58$, $p < 0.05$) and Caribbean ($r = 0.56$, $p < 0.05$) storm number but not with non-Caribbean storm number ($r = 0.13$, $p = 0.60$). Further correlation analysis are performed for other 3-month windows between June and November (JJASON) and for JJASON. The results are similar to those for ASO. In particular, across all windows analysed, the correlations between Amazon fire and tropical cyclone remain significant for North Atlantic (except for JJA) and Caribbean storms and insignificant for non-Caribbean storms. For the rest of this chapter, focus is put on ASO, which is the most active season for both fire and storm, motivated by their seasonal cycles.

3.3.2 North Atlantic SST and ITCZ behaviour

Existing works on the relationship between North Atlantic SST and ITCZ behaviour (e.g. Enfield 1996, Moron et al. 1995) focus on the boreal spring and summer, which precedes the Amazon fire season. The behaviour of the two in spring (MAM) however are quite different to the situation in ASO. Ranking the years 2001–2018 by ASO Amazon fire count, the composite anomalies of the precipitation and SST between the highest and lowest 5

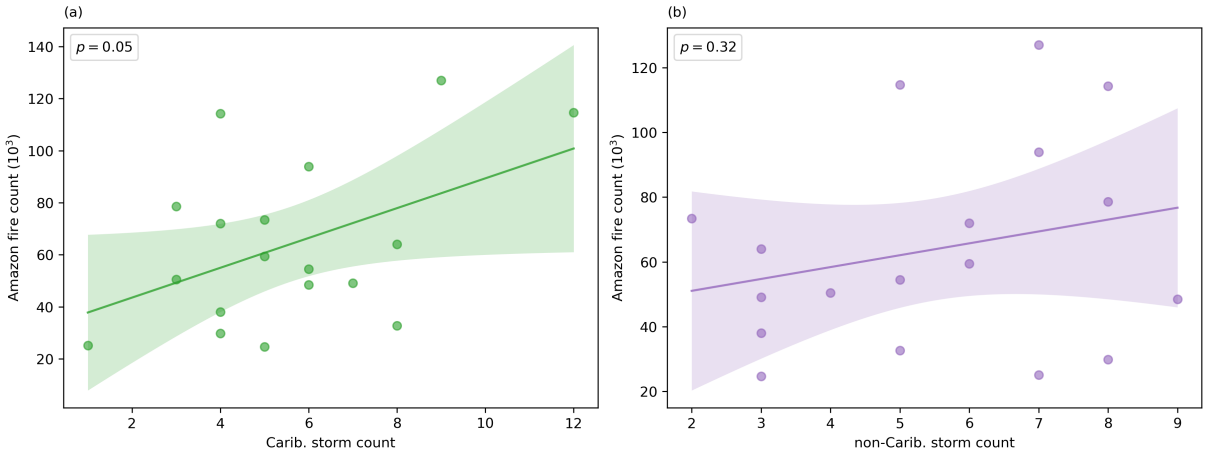


Figure 3.2: (a) Scatter plot with linear least square fit of ASO Amazon fire count against ASO Caribbean tropical cyclone count in the years 2001–2018. Shaded region indicates 95% confidence interval. (b) Same as (a) except against non-Caribbean tropical cyclone count.

years are determined. Correlation maps of both precipitation and SST with ASO Amazon fire count are also produced. They show patterns very similar to those from the composite differences.

In MAM, the fire region is immediately to the south of the ITCZ (Figure 3.3 (a)), thus any meridional shift of the ITCZ will directly affect the amount of precipitation the fire region receives. However, in ASO the ITCZ has shifted much further north (48° W–17° W, 2° N–13° N) and no longer overlaps the fire region (Figure 3.3 (b)). In MAM, there is a clear meridional shift of the Atlantic ITCZ between the high and low fire years (Figure 3.3 (c, e)). However, no such shift is observed in ASO; rather it is the amount of precipitation over the ITCZ that is different (Figure 3.3 (d, f)). The composite precipitation anomaly over the fire region is significant in both MAM and ASO, with the absolute magnitude in ASO being around half of that in MAM. Furthermore, the correlation of ASO Amazon fire count with Amazon precipitation is significant for both MAM ($r = -0.50$, $p < 0.05$) and ASO ($r = -0.55$, $p < 0.05$; non-detrended: $r = -0.40$, $p = 0.10$), although these signals do not show up conspicuously on the correlation maps (Figure 3.3 (e–f)).

Corresponding to positive ASO Amazon fire anomaly, a clear tropical North Atlantic SST warm anomaly is observed in MAM (Figure 3.4 (b, e)). However, this SST signal is barely significant in ASO (Figure 3.4 (d, f)). The SST climatology in these 2 seasons are shown in Figure 3.4 (a–b). North Atlantic SST in MAM does appear to act as a precursor to the precipitations over parts of the North Atlantic in ASO. In particular, Figure 3.5 shows scatter

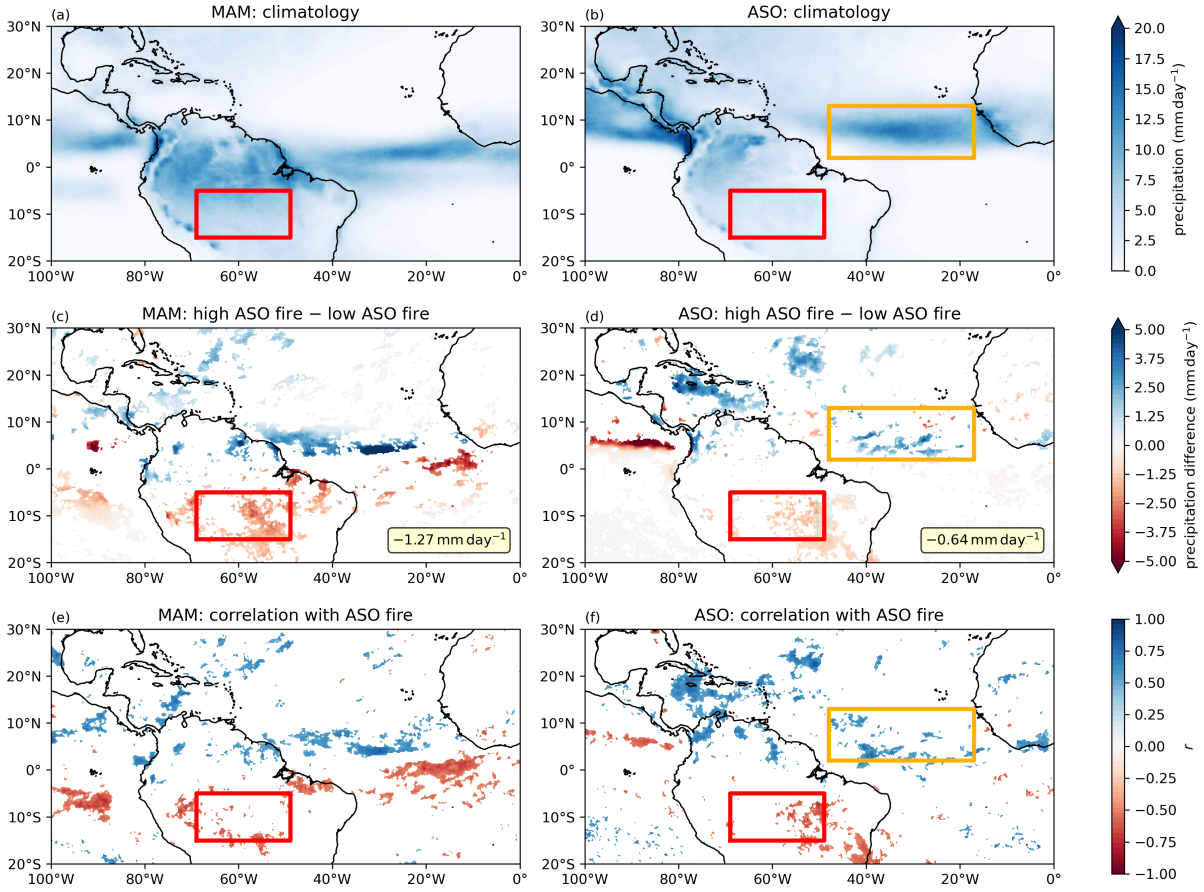


Figure 3.3: (a–b) Climatology of (a) MAM and (b) ASO precipitation between 2001 and 2018. (c–d) Same as (a–b) except for composite difference (significant at 95% confidence interval) of the top and bottom 5 years between 2001 and 2018 ranked by ASO Amazon fire count. Average precipitation difference over the Amazon is given in the lower right. (e–f) Same as (a–b) except for correlation with ASO Amazon fire count. (a–f) The red box is the Amazon fire region. (b, d, f) The orange box includes the Atlantic ITCZ.

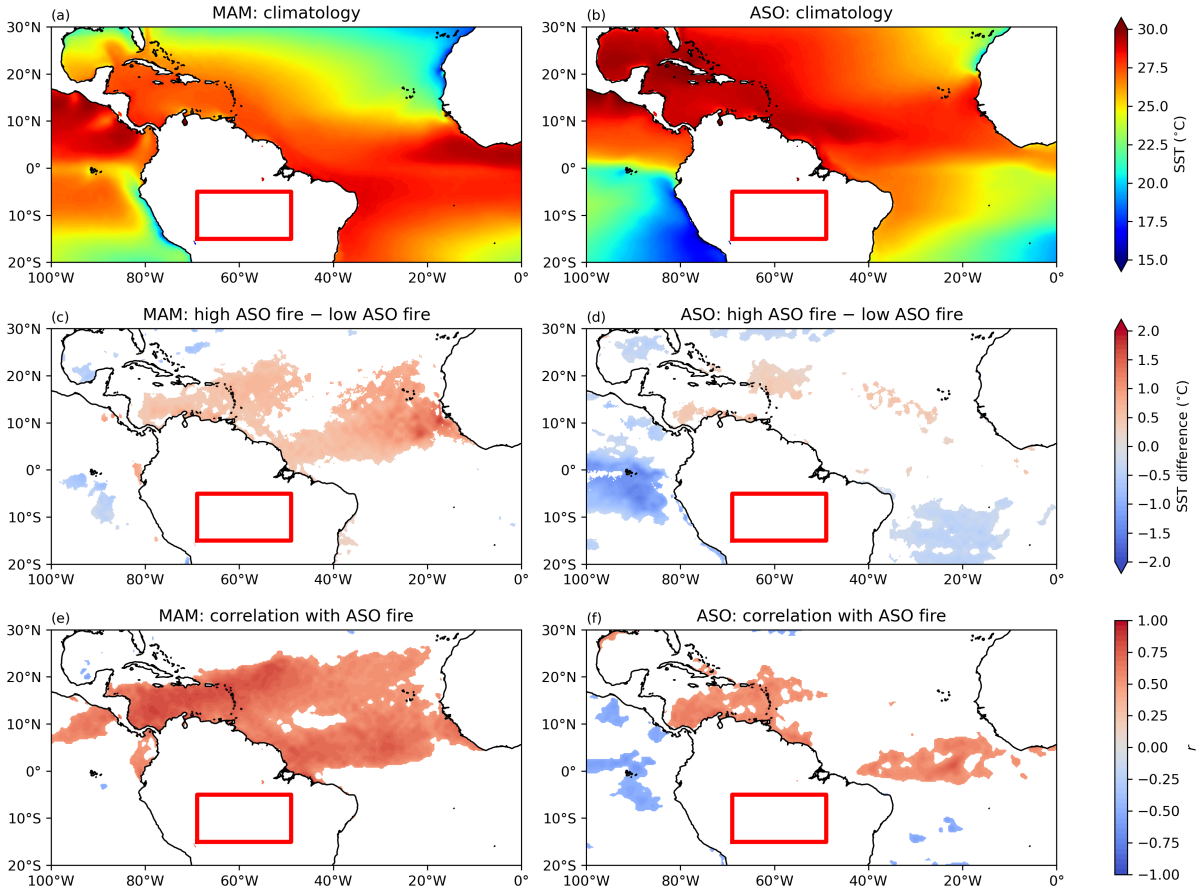


Figure 3.4: Same as Figure 3.3 except for SST. The red box is the Amazon fire region.

plots with linear least square fits for precipitations over the Atlantic ITCZ and the Caribbean in ASO against North Atlantic SST in MAM. Correlation analysis reveal significance for MAM North Atlantic SST with both ASO Atlantic ITCZ precipitation ($r = 0.85$, $p < 0.01$) and ASO Caribbean precipitation ($r = 0.77$, $p < 0.01$).

3.3.3 Atlantic ITCZ and Caribbean precipitation

The relationships between Amazon fire activity, ASO ITCZ precipitation, Caribbean precipitation and North Atlantic tropical cyclones are next explored through composite difference of anomalous years. The years 2001–2018 are ranked by 3 criteria: Amazon fire count, Atlantic ITCZ precipitation and Caribbean precipitation. The composite anomalies of the precipitation, horizontal wind at 850 hPa and 850 hPa-200 hPa vertical wind shear between the highest and lowest 5 years are determined. The anomaly patterns for the variables studied show common features across all 3 criteria. In direction consistent with more fires, there is more precipitation in the Caribbean and the ASO Atlantic ITCZ (Figure 3.6). There

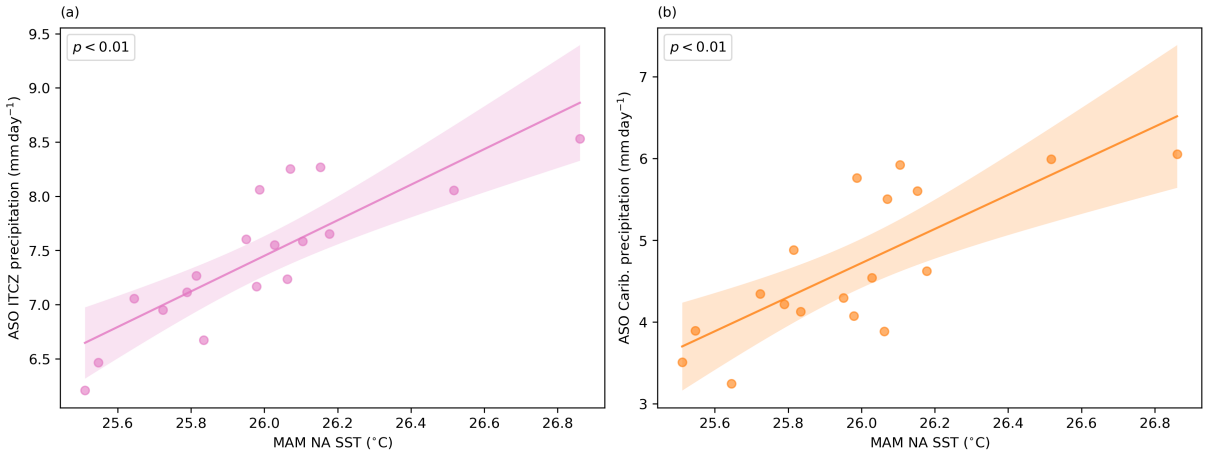


Figure 3.5: (a) Scatter plot with linear least square fit of ASO Atlantic ITCZ precipitation against MAM North Atlantic SST in the years 2001–2018. Shaded region indicates 95% confidence interval. (b) Same as (a) except for ASO Caribbean precipitation.

are also anomalous low-level westerlies which are part of an extended anomalous low-level cyclonic circulation over the entire Caribbean. Reduced vertical wind sheer is found along a corridor where much of the North Atlantic tropical cyclones develop, although between the high and low fire years a large part of this reduction is deemed insignificant by bootstrapping. These conditions of enhanced low level vorticity and reduced vertical wind shear favour tropical cyclone genesis and intensification. Anomalous convergence is found in the Atlantic ITCZ including strong inflow from the south driving enhanced precipitation. The precipitation over the Atlantic ITCZ and the Caribbean are highly correlated ($r = 0.84$, $p < 0.01$), showing coherence of these 2 regions.

3.3.4 Caribbean storms and Amazon fires

The relationships between Caribbean storm count and Amazon fires are next explored. The fire count and the Caribbean precipitation ($r = 0.59$, $p < 0.01$; non-detrended: $r = 0.52$, $p < 0.05$), the Caribbean tropical cyclone number and the Caribbean precipitation ($r = 0.66$, $p < 0.01$) and the fire count and the Caribbean tropical cyclone number ($r = 0.56$, $p < 0.05$) all show significant correlations. The fire count also correlates with the Atlantic ITCZ precipitation ($r = 0.56$, $p < 0.05$; non-detrended: $r = 0.45$, $p = 0.06$) but not with non-Caribbean storm number ($r = 0.13$, $p = 0.60$).

If an active role for tropical cyclones is hypothesised, it is important to estimate the tropical cyclone contribution to Caribbean precipitation anomalies. To test this, the precipitation

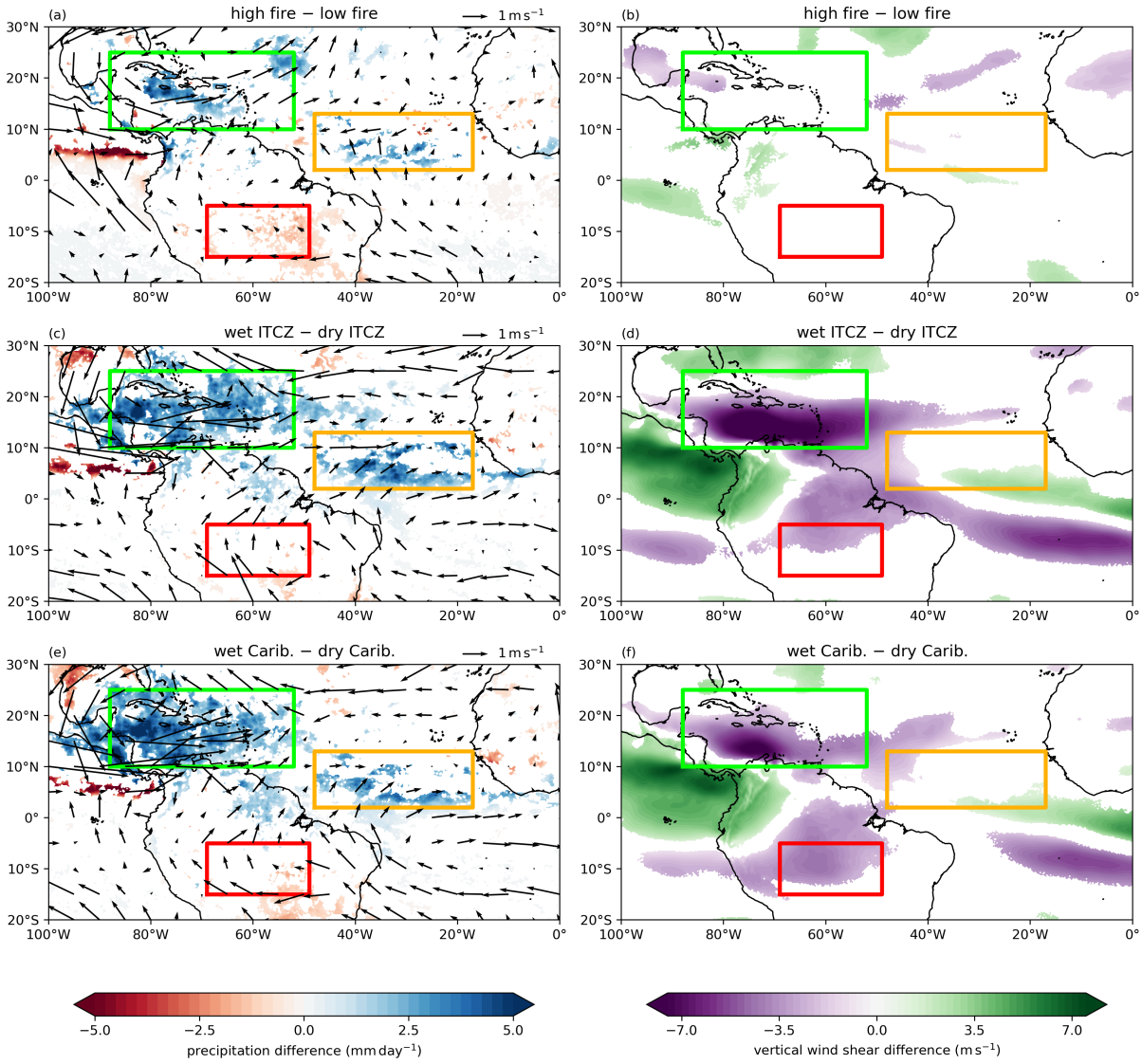


Figure 3.6: (a, c, e) Composite difference of ASO horizontal wind at 850 hPa and precipitation (significant at 95% confidence interval) of the highest and lowest 5 years between 2001 and 2018 ranked by (a) ASO Amazon fire count, (c) ASO Atlantic ITCZ precipitation and (e) ASO Caribbean precipitation. (b, d, f) Same as (a, c, e) except for 850 hPa-200 hPa vertical wind shear. (a–f) The boxes are Amazon (red), Atlantic ITCZ (orange) and Caribbean (green).

of Caribbean tropical cyclone days is replaced with the n-day moving average non-storm day climatology. By taking the difference, it is inferred that the tropical cyclones account for 35–36% (n between 3 and 15) of the precipitation anomaly between the wettest and driest 5 years in the Caribbean. Replacing storm days with zero precipitation boosts the result to 65%. Therefore, tropical cyclones contribute substantially to precipitation anomalies in the Caribbean. Examination on individual years also support the relationship. For example, 2010 is a year with record (over the years studied here) Atlantic ITCZ precipitation, record Caribbean precipitation and record storm count. It is also the year with the second highest Amazon fire count.

3.3.5 Atmospheric Amazon fire risk factors

The connection between the Caribbean and the Amazon can be further explored by examining the tropical cyclones and precipitation over the Caribbean and the vertical velocity, surface solar radiation flux and the FWI over the Amazon. While TRMM precipitation data and MODIS Active Fire Products are respectively available only from 1998 and 2001 onwards, ERA5 precipitation and ERA5-based FWI data enable a much longer period for analyse from 1980 to 2019. For the common period with both MODIS and ERA5-based FWI data, the fire count and risk index are positively correlated with significance ($r = 0.58$, $p < 0.05$; non-detrended: $r = 0.31$, $p = 0.21$). As with fire count, the FWI is significantly correlated to both Caribbean precipitation ($r = 0.58$, $p < 0.01$) and Caribbean storm number ($r = 0.33$, $p = 0.05$; non-detrended: $r = 0.50$, $p < 0.01$) but not with non-Caribbean storms ($r = 0.13$, $p = 0.41$) between 1980 and 2019. During the same period, the vertical velocity at 600 hPa shows significant correlations with the FWI ($r = 0.83$, $p < 0.01$), Caribbean precipitation ($r = 0.49$, $p < 0.01$) and Caribbean storm number ($r = 0.32$, $p < 0.05$; non-detrended: $r = 0.43$, $p < 0.01$) but not with non-Caribbean storms ($r = 0.08$, $p = 0.62$). Figure 3.7 shows that suppressed ascent and enhanced FWI over the Amazon is associated with more Caribbean storms and precipitation but not with non-Caribbean storms. The vertical velocity at 600 hPa is correlated with surface solar radiation flux ($r = 0.93$, $p < 0.01$), which is in turn correlated with the FWI ($r = 0.85$, $p < 0.01$). The years 1980–2019 are further ranked by Amazon FWI, Caribbean tropical cyclone count and Caribbean precipitation to determine the composite anomalies of the precipitation and vertical velocity at 600 hPa between the highest and lowest 13 years. Fig-

ure 3.8 shows that when there is higher FWI in the Amazon and more precipitation and ascent over the Caribbean, there is also significant anomalous descent and reduced precipitation over the Amazon. The anomalous subsidence can reduce any local mean ascent. This in turn reduces the cloud cover and enhances the surface solar radiation flux. The FWI is then enhanced by lower relative humidity and higher surface temperature.

3.4 Discussion

The seasonal cycles of North Atlantic tropical cyclones and South Amazon fires are in phase and both peak in September (Figure 3.1). Furthermore, most of the Amazon's fires and North Atlantic tropical cyclones are found within ASO. This establishes ASO as a critical season for understanding a possible teleconnection between the two. The Amazon fire count is significantly correlated only with Caribbean tropical cyclone number ($r = 0.56$, $p < 0.05$) but not with non-Caribbean ones ($r = 0.13$, $p = 0.60$), even though the Caribbean and non-Caribbean tropical cyclones both account for around half of all North Atlantic tropical cyclones on average. Correlation and composite analysis further reveal a link between Caribbean tropical cyclone count and Amazon fires via Caribbean and Amazon vertical atmospheric motion. Much of the ASO precipitation and ascent anomalies in the Caribbean can be accounted for by the tropical cyclones in the region. It is also seen that anomalous atmospheric conditions favourable to North Atlantic tropical cyclone genesis and intensification are found when there are more fires in the Amazon. An intensification of Atlantic ITCZ precipitation is also associated with more Amazon fires.

The current paradigm links Amazon fire variability to the varying amount of precipitation over the Amazon (Chen et al. 2015, Fernandes et al. 2011, Chen et al. 2011). The Amazon precipitation variability is in turn attributed to meridional Atlantic ITCZ shifts in response to Atlantic SST anomalies (Enfield 1996, Moron et al. 1995). These existing studies aim to predict fire activity and thus are focused on precursor variables in the boreal spring and summer. The study in this chapter focuses exclusively on the peak fire season (ASO) and concurrent atmospheric conditions. A meridional shift in the Atlantic ITCZ is not found during this season between high and low fire years. Instead, anomalous precipitation over the Caribbean (and the ITCZ) is observed. These findings are consistent with the current understanding of South America precipitation variability (de Souza et al. 2021),

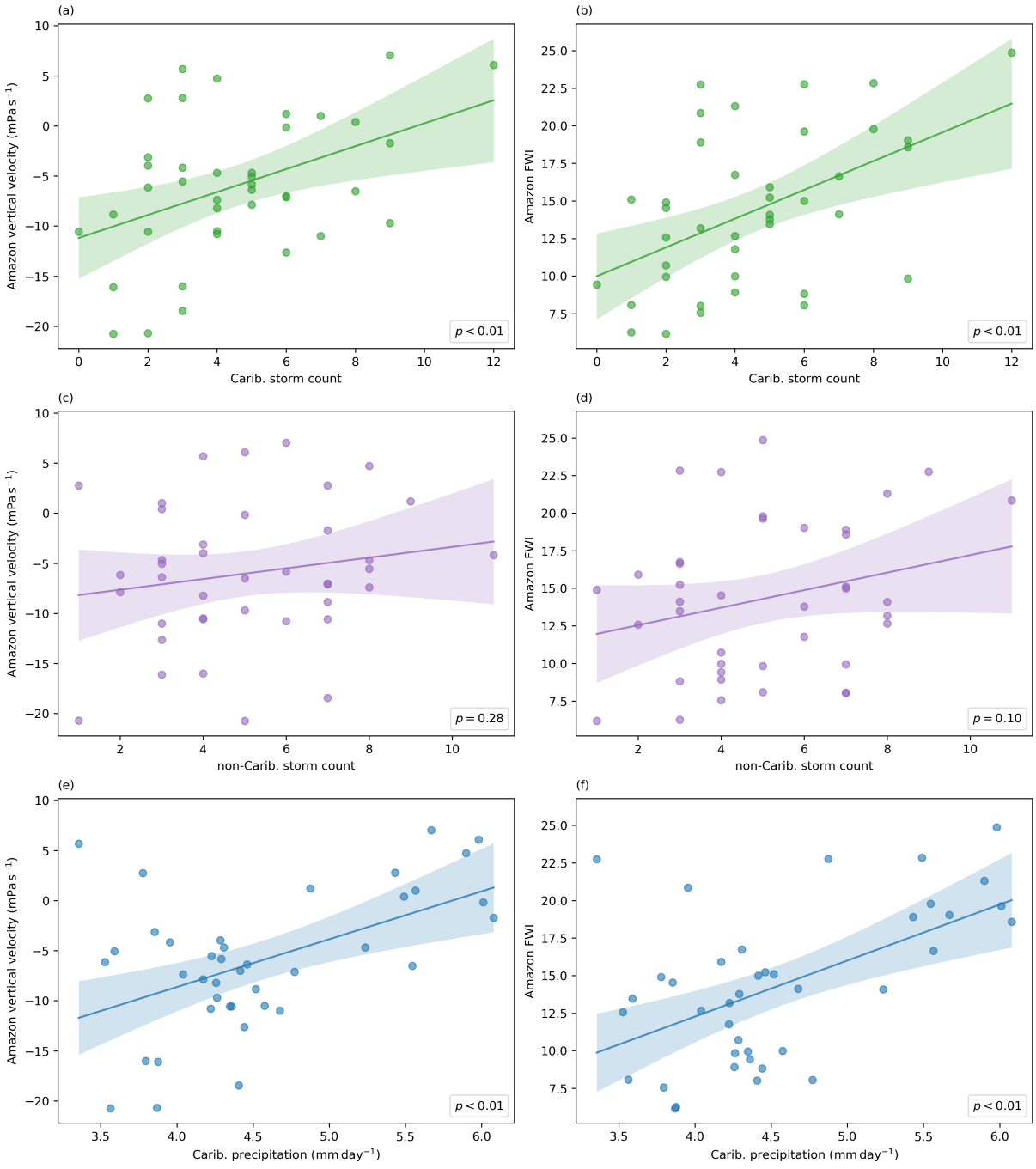


Figure 3.7: (a) Scatter plot with linear least square fit of ASO Amazon vertical velocity at 600 hPa against ASO Caribbean tropical cyclone count computed from 1980 to 2019. Shaded region indicates 95% confidence interval. (c) Same as (a) except against ASO non-Caribbean tropical cyclone count. (e) Same as (a) except against ASO Caribbean precipitation. (b, d, f) Same as (a, c, e) except for ASO Amazon FWI.

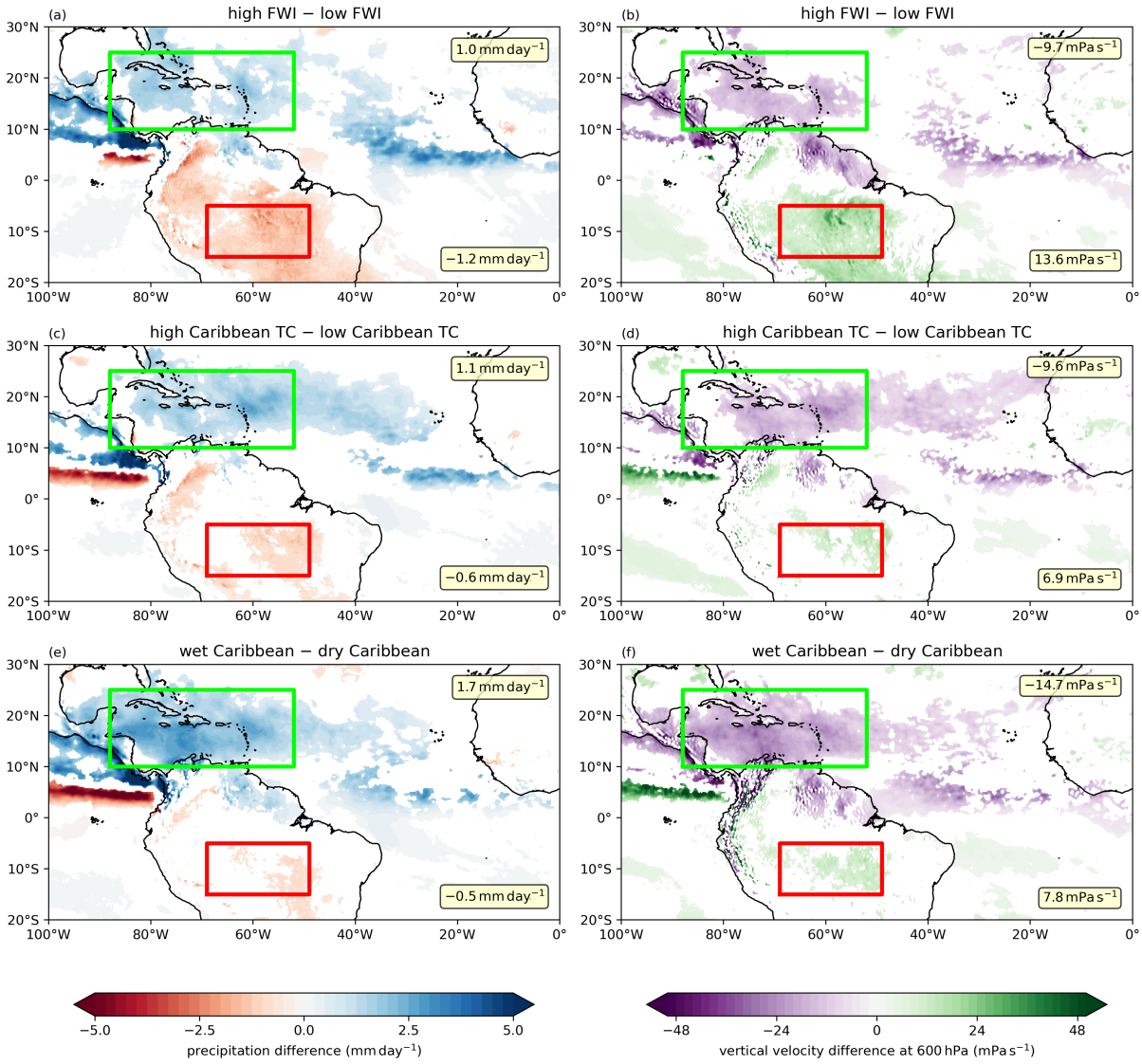


Figure 3.8: (a, c, e) Composite difference (significant at 95% confidence interval) for ASO precipitation of the top and bottom 13 years between 1980 and 2019 ranked by (a) ASO Amazon FWI, (c) ASO Caribbean tropical cyclone count and (e) ASO Caribbean precipitation. Average precipitation difference (significant at 95% confidence interval) over the Caribbean and the Amazon are given in the upper right and lower right respectively. (b, d, f) Same as (a, c, e) except for vertical velocity at 600 hPa.

where the meridional shift of the Atlantic ITCZ is attributed to the precipitation variability in the boreal spring but not autumn. It is clear from these results that the Amazon fire count and precipitation in the peak fire season (ASO) have very different relationships with the Atlantic precipitation and SST than those studied previously for pre-seasons.

El Niño-Southern Oscillation (ENSO) has been reported to affect Amazon fires (Alencar et al. 2011, Ferreira Barbosa et al. 2021). The authors argued that this is due to ENSO-induced droughts over the Amazon via its impact on the precipitation there in the dry season (June to October), which largely coincides with the fire season. However, Amazon droughts can occur under both a warming or cooling of the Pacific (Silva Junior et al. 2019). Yoon & Zeng (2010) advocated considering Amazon precipitation variability as the result of a complex interplay between Atlantic and Pacific influences, with the former being the primary driver. They also pointed out that while North Atlantic SST anomalies consistently influence Amazon precipitation throughout the year except in the wet season (December to April), the direct influence of ENSO on Amazon precipitation is over the wet season and has very limited effect over the dry season. It is likely that previous studies linking Amazon fires with ENSO via droughts actually picked up on Atlantic SST signals that may be partly influenced by the Pacific. Indeed, Chen et al. (2011) observed that in general, Amazon fires are correlated with the Atlantic Multidecadal Oscillation index (AMO) at shorter lead-times and much more strongly than with the Ocean Niño Index (ONI). When constructing their statistical prediction model for Amazon fire using both AMO and ONI as predictors, the former is given a weight that is at least 3.8 times that of the latter. This could partly be understood based on the seasonality of the Atlantic and Pacific influences on Amazon precipitation variability shown by Yoon & Zeng (2010).

While ENSO appears to have complex and indirect influence on Amazon fires, its impacts on North Atlantic tropical cyclone activities are much better understood. It has been observed that ENSO is negatively correlated to the occurrence of both hurricanes and major hurricanes in the Atlantic basin (Gray 1984, Shapiro 1987, Goldenberg & Shapiro 1996, Wilson 1999, Goldenberg et al. 2001). During the warm phase of ENSO, upper-tropospheric westerlies over the tropical North Atlantic is intensified, leading to increased vertical wind shear over the main development region of tropical cyclogenesis in the Atlantic (10° N–20° N), suppressing the formation of both hurricanes (Gray 1984, Shapiro 1987) and major hurricanes (Goldenberg & Shapiro 1996, Goldenberg et al. 2001). The warming of the free

troposphere over the Atlantic due to El Niño has been proposed as an additional pathway for ENSO to influence Atlantic tropical cyclone activities based on the idea that a troposphere that is warm relative to SST tends to discourage tropical cyclone intensification (Tang & Neelin 2004). Furthermore, Tartaglione et al. (2003) showed that the probability of hurricanes making landfall in the Caribbean is increased in ENSO cold phase years but similar in warm phase and neutral years, although responsible mechanisms have not been identified.

Overall, although ENSO could affect both Amazon fires and North Atlantic tropical cyclone activities, it is difficult to consider it to serve as a link between the two even as a common driver, let alone establishing a direct physical pathway. From the study here, a more complete understanding of the drivers of Amazon fires emerges and possible sources of seasonal Amazon fire predictability are identified. The MAM Atlantic SST anomalies could be a persistent precursor to an enhanced ASO Atlantic ITCZ, which favours tropical cyclones. This is supported by a significant correlation between the two ($r = 0.85, p < 0.01$). As explained below, this study leads to the conclusion that it is the ASO Caribbean precipitation and tropical cyclones that can provide a plausible direct physical link to the Amazon fires via a Hadley-type circulation anomaly. Another example of tropical cyclones and fires as a pair of remote compound extreme events with teleconnection in the zonal rather than meridional direction via the amplification of atmospheric wave train has recently been reported by Stuivenvolt Allen et al. (2021).

An active hurricane season in the Caribbean brings anomalous precipitation and therefore latent heating to the region. Such localised heating and ascent to the north of the equator is hypothesised to drive a thermally direct circulation causing raised pressure and anomalous subsidence in the Southern Hemisphere akin to the Hadley Cell circulation. This anomalous subsidence then reduces precipitation and cloud cover, promotes surface solar heating and leads to higher surface temperatures, all of which are favourable to fire.

In the classic Hadley Cell, warm rising air near the equator reaches the stable tropopause and travels down the high-level pressure gradient polewards, cools and sinks in the subtropics. Studies have found that similar circulation can develop with an off-equatorial ascending branch to the north and a corresponding descending branch to the south of the equator. Simulations by Rodwell & Hoskins (2001) incorporating orography and forced with heating from monsoon precipitation showed that in both the Americas and West Africa, off-equatorial heating in the Northern Hemisphere induces local thermally direct, Hadley-type,

circulation with an ascending branch around the heating region and a descending branch to the south across the equator. Krishnan et al. (2003) simulated the Indian summer monsoon with a precipitation field that peaks over the Bay of Bengal (7° N–23° N) and a thermally direct circulation with a descending branch between 35° S and 15° S.

The thermally direct cell circulation is also captured by the simplified Matsuno-Gill model (Gill 1980, Phlips & Gill 1987). In the solution presented by Phlips & Gill (1987) in their Figure 10D, the area of subsidence is equidistant from the equator and zonally displaced slightly east of the heating region. In another idealised simulation by Wang et al. (2020), with heating centred at 10° N, subsidence is observed between 20° S and 5° S, centred further from the equator than the heating region. However, the pressure contour and flow pattern resulting from the idealised Matsuno-Gill model can be modified considerably by factors such as the shape and equatorial off-set of the heating region and the presence of background zonal wind (Phlips & Gill 1987). In our case, the area of anomalous subsidence over South Amazon has a slight zonal off-set to the east of and is closer to the equator than the heating in the Caribbean, similar to the results by Rodwell & Hoskins (2001).

3.5 Conclusions

The seasonal cycles of North Atlantic tropical cyclones and South Amazon fires are in phase with a maximum around September and have significant interannual correlation driven exclusively by Caribbean tropical cyclones. Years of high fire activity are associated with atmospheric conditions over the Caribbean which favour tropical cyclones, enhanced precipitation, local ascent and remote anomalous Amazon subsidence. It is hypothesised here that a direct physical link of tropical cyclones in the Caribbean to fires in the South Amazon could be established through a thermally direct, Hadley-type, circulation response driven by off-equatorial heating partly caused by the storms. Anomalous precipitation over the Caribbean, regardless of cause, releases latent heat there and contributes to the thermally direct circulation. However, Caribbean tropical cyclones play an important role based on the analysis in this chapter as they account for much of the precipitation anomalies in the region. The anomalous Amazon subsidence observed promotes fire-favourable atmospheric conditions over the region. Anthropogenic drivers, such as deforestation, are a major contributor to fires in the Amazon (Marengo et al. 2018, Aragão et al. 2018). Some of the

interannual variability is therefore due to the interaction of man-made burning with environmentally favourable conditions. By focusing on the fire season, this study leads to a deeper understanding of Amazon fire variability than previous studies which considered the pre-season. This study helps build a more complete understanding of the meteorological drivers of Amazon fires and provides evidence for a case of remote physically linked compound extreme events.

Chapter 4

Pacific Subsurface Temperature as a Long-range Indicator of El Niño, Regional Precipitation, and Fire

4.1 Introduction

On interannual time scales, ENSO plays a dominating role in modulating climates throughout the tropics and beyond. SST signals that capture the state of ENSO are often central to the prediction of many atmospheric responses driven by ENSO. On the other hand, the ENSO cycle itself consists of a subsurface branch which is essential to bringing the surface ENSO state to maturity. This chapter explores the possibility of achieving long-range prediction of ENSO-driven atmospheric responses by tracing the maturing of the surface ENSO state back to any preceding signals in the subsurface temperature or heat content anomalies in the Pacific basin.

Bjerknes (1966, 1969) first proposed that El Niño and La Niña are brought to a mature state by a positive feedback among equatorial Pacific SST anomaly, equatorial Pacific zonal wind anomaly via SST gradient, Hadley circulation, Walker circulation and ocean circulation. Since then, various negative feedback mechanisms have been put forward to allow for the oscillatory behaviour of ENSO, giving rise to 4 different self-sustained oscillator models for ENSO — the delayed oscillator model (Suarez & Schopf 1988, Battisti & Hirst 1989), the recharge-discharge oscillator model (Jin 1997*a*,*b*), the western Pacific oscillator model (Weisberg & Wang 1997, Wang et al. 1999) and the advective-reflective oscillator model

(Picaut et al. 1997) (see Section 1.2.2 for details). The unified oscillator model (Wang 2001, 2018) nicely summarises the 4 self-sustained oscillator models, suggesting that all proposed negative feedback mechanisms are at work together, the relative importance of which could vary with time. It has been identified that a build-up of ocean heat content resulting from advective processes is necessary for the onset of El Niño (Timmermann et al. 2018, Ramesh & Murtugudde 2013, Ballester et al. 2016). In particular, Ramesh & Murtugudde (2013) showed that a subsurface discharge of warm water always begins prior to an El Niño event and can precede the peak by up to 18 months. Thus, successful capturing of such processes holds the key to long-range ENSO forecast (Timmermann et al. 2018, Ramesh & Murtugudde 2013, McPhaden 2004, McGregor et al. 2012, Ballester et al. 2016, Petrova et al. 2017).

The incorporation of subsurface temperature into statistical ENSO oceanic surface state predictions has been explored previously (e.g. Drosdowsky 2006, Petrova et al. 2017, 2020). In this chapter, the idea is extended to study directly the relationship between subsurface temperature and atmospheric responses throughout the tropics identified to have teleconnection with the ENSO oceanic surface state. In particular, the western Pacific warm water volume (WWV_W) has been used as a long-range predictor for ENSO (e.g. Zhao et al. 2021, Izumo et al. 2019, Planton et al. 2018). Here, an index similar to WWV_W but based on subsurface potential temperature (SubT) around the thermocline is proposed. The SubNiño4 index is defined to be the SubT anomaly averaged beneath the Niño4 region between the depths of 100 m and 300 m. Sparks & Toumi (2020) first constructed a similar index, which they called the subNiño4 index, as the mean June to August "subsurface ocean temperature anomaly" averaged over the same region, and showed that it is capable of predicting tropical cyclone landfall in South China with a lead-time of 1 year. They attributed this success to the surfacing of the temperature anomaly around the SubNiño4 region, establishing SST patterns which influence atmospheric circulation patterns.

It will be shown in this chapter that the SubNiño4 index captures the subsurface heat advection around half-way between the mature El Niño and La Niña phases of the ENSO cycle. The lagged correlation between observed SubNiño4 and Niño3.4 can exceed the simultaneous correlation between observed and dynamically predicted ENSO at a lead-time of around 12 months. It will also be shown that the SubNiño4 index may be more reliable than the WWV_W indicator. Using regional precipitations and fires as examples, it

will be demonstrated that the SubNiño4 index can further serve as a long-range indicator of ENSO-driven atmospheric phenomena in many regions throughout the tropics.

4.2 Methods

To obtain the time series of the Niño3.4 index, the HadISST1 monthly SST data is averaged over the Niño3.4 region (170° W–120° W, 5° S–5° N) and then the seasonal cycle computed from the 30-year period from 1986 to 2015 is removed. The time series of the SubNiño4 index is obtained similarly from the EN4.2.2 monthly SubT data, averaging over the Niño4 region (160° E–150° W, 5° S–5° N) and between the depths of 100 m and 300 m. The 20 °C isotherm is used as a proxy for the thermocline and the monthly average 20 °C isotherm depth (Z20) profiles are determined by interpolating the monthly SubT data vertically. The Niño4-Z20 anomaly time series is then obtained from the monthly Z20 profiles using the same procedure for the Niño3.4 index, averaging over the Niño4 region. The WWV_W is the volume of water above the 20 °C isotherm within 120° E to 160° W and 5° S to 5° N and its anomaly time series is obtained as above. The time series of the surface zonal wind stress anomaly over the Niño4 region is obtained from the ERA5 monthly eastward turbulent surface stress data similarly.

To study the behaviour of the Niño3.4 and SubNiño4 time series, their 3-month moving average time series are considered, mirroring the definition of surface Niño indices. Their mean, standard deviation, skewness and excess kurtosis are computed. Discrete Fourier transform is performed on the time series to obtain their frequency spectra. Peaks are considered significant if their amplitude is above the 95-th percentile from an ensemble of 10000 first-order autoregression (AR(1)) model simulations. The AR(1) model time series is given by the recurrence relation

$$\hat{x}_{t+1} - \hat{\mu} = \hat{\phi}\,(\hat{x}_t - \hat{\mu}) + \varepsilon_{t+1}, \tag{4.1}$$

where $\hat{\mu}$ is the mean, $\hat{\phi}$ the autoregressive parameter and the ε's random, independent and follow $\mathcal{N}\left(0, \sigma_\varepsilon^2\right)$. The parameters $\hat{\mu}$, $\hat{\phi}$ and σ_ε^2 are estimated from the original time series by

$$\hat{\mu} = \overline{x} = \frac{1}{n}\sum_{t=1}^{n} x_t, \tag{4.2}$$

$$\hat{\phi} = \frac{\sum_{t=1}^{n-1} (x_t - \overline{x}_-)(x_{t+1} - \overline{x}_+)}{\sqrt{\sum_{t=1}^{n-1} (x_t - \overline{x}_-)^2} \sqrt{\sum_{t=2}^{n} (x_t - \overline{x}_+)^2}}, \tag{4.3}$$

$$\sigma_\varepsilon^2 = \frac{1 - \hat{\phi}^2}{n-2} \sum_{t=1}^{n} (x_t - \overline{x})^2, \tag{4.4}$$

where $\overline{x}_-$ ($\overline{x}_+$) is the mean of the first (last) $n-1$ data from the original time series. A subsurface warm (cold) episode is defined to be the period when the SubNiño4 3-month moving average time series exceeds 0.5 °C (−0.5 °C) for at least 5 consecutive 3-month periods, mirroring the definition of El Niño and La Niña episodes with surface Niño indices.

To study the time evolution of the SubT anomaly profile, the monthly SubT profile is first averaged between the latitudes of 5° S and 5° N and linearly detrended. The seasonal cycle computed from the 30-year period from 1986 to 2015 is then removed and the 3-month moving average is considered. The peak of each subsurface warm and cold episode is identified and used as anchor to align all episodes. The composite difference between warm and cold episodes is taken at various 3-month periods before and after the peak for up to 1 year and significance is determined by bootstrapping with 5000 resamples. Correlation analysis is performed between the SubNiño4 index at the peak 3-month period and the processed subsurface profile with various lead/lag for up to 1 year.

To investigate the connection between the surface and subsurface, the lagged correlations between the SubNiño4 index and various surface variables, including the Niño3.4 index, global and regional precipitations and FWI are computed. Figure 4.1 gives an overview of the regions considered in this chapter.

The Niño3.4 index and the GPCP global precipitation field are averaged over the 4 main seasons of December to February (DJF), March to May (MAM), June to August (JJA) and September to November (SON). The Niño3.4 index is correlated with the SubNiño4 index and, for benchmarking purposes, the WWV_W anomaly in the 25 overlapping 3-month periods leading up to each of the 4 main seasons. The global precipitation field is correlated with the SubNiño4 index in the 3-month period exactly 1 year before each of the 4 main seasons.

The GPCP precipitation over the Maritime Continent (95° E–150° E, 12° S–5° N) DJF (King & Vincent 2018), Northeast Brazil (47° W–35° W, 10° S–0°) MAM (Folland et al.

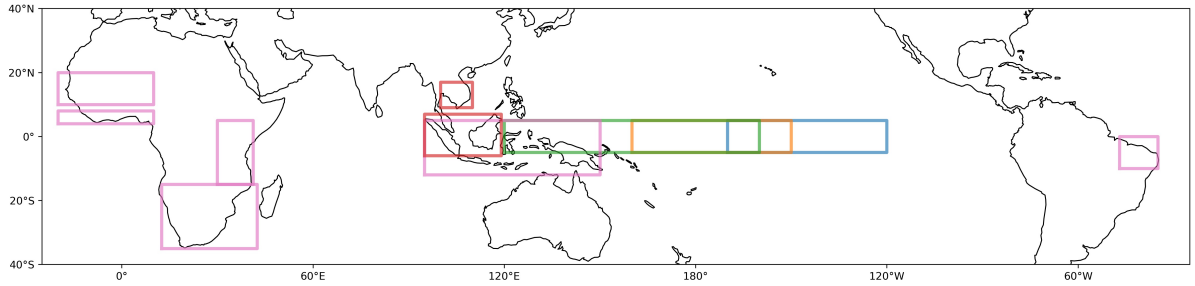


Figure 4.1: Blue box is the Niño3.4 region. Orange box shows the horizontal extant of the SubNiño4 region. Green box shows the horizontal extant of the region over which WWV_W is defined. Pink boxes are the domains considered for regional precipitations, except for that covered by the IITM all-India dataset. Red boxes are the domains considered for Southeast Asian fires.

2001), Gulf of Guinea (20° W–10° E, 4° N–8° N) and Sahel (20° W–10° E, 10° N–20° N) from June to September (JJAS) (Losada et al. 2012), South Africa (12.5° E–42.5° E, 35° S–15° S) from December to March (DJFM) (Hoell et al. 2017) and East Africa (30° E–41.25° E, 15° S–5° N) from October to December (OND) (Mutai et al. 1998) are correlated with the SubNiño4 index and, for benchmarking purposes, the WWV_W anomaly and the Niño3.4 index for the 25 overlapping 3-month periods leading up to the relevant precipitation season. The analysis is also performed on the Maritime Continent over the remaining 3 main seasons of MAM, JJA and SON; on East Africa MAM; and on the IITM all-India rainfall JJAS.

The analysis described above for regional precipitation is repeated for the FWI averaged over the most fire-active part of Maritime Southeast Asia (95° E–119° E, 6° S–7° N) from June to October (JASO) and Continental Southeast Asia (100° E–110° E, 9° N–17° N) DJFM. The 2 regions are chosen to capture most of the fire and the corresponding peak season for the FWI over the respective region is chosen for study.

All time series are linearly detrended before correlation analysis. All correlation coefficients in this study are Pearson correlation coefficients.

4.3 Results

4.3.1 Connection between sea surface and subsurface temperatures

The Niño3.4 and SubNiño4 time series between 1979 and 2020 are shown in Figure 4.2 (a). In general, the SubNiño4 index leads the Niño3.4 index by a fairly constant time of about 6 to 12 months. The subsurface warm and cold episodes identified are shaded in pink and

cyan respectively. Figure 4.2 (b) shows the frequency spectra of the Niño3.4 and SubNiño4 time series together with corresponding benchmark amplitude from an AR(1) ensemble with 10000 members. Both frequency spectra have significant peaks above the 95-th percentile amplitude corresponding to periods of 1.46 yr and 4.53 yr. In between, Niño3.4 shows 6 more significant peaks but only 2 are matched by SubNiño4; just beyond the high frequency end, Niño3.4 displays 2 more significant peaks, none of which are matched by SubNiño4. The 2 frequency spectra are similar overall but that of SubNiño4 is less noisy. Normalised histograms of the 2 indices are shown in Figure 4.2 (c). The SubNiño4 index displays a higher mean, lower standard deviation and higher kurtosis than the Niño3.4 index. The SubNiño4 index is negatively skewed while the Niño3.4 index is positively skewed, with the former having a higher absolute skewness. The normalised histograms of the SubNiño4 index and the Niño4-Z20 anomaly resemble each other (Figure 4.2 (c–d)). They are highly correlated ($r = 0.99$, $p < 0.01$) and have similar negative skewness. The normalised histogram of the surface zonal wind stress anomaly over the Niño4 region is shown in Figure 4.2 (e). It is positively skewed and significantly correlated with the SubNiño4 index in December ($r = -0.34$, $p < 0.05$) and January ($r = -0.49$, $p < 0.01$). Figure 4.2 (f) shows the SubT observation weights for 27 points inside the SubNiño4 region and the region-averaged observation weight from 1960 to 2020. To ensure data quality, only data from 1979 onwards are used in this study unless otherwise specified.

Figure 4.3 shows the time evolution of the composite difference of the SubT profiles between subsurface warm and cold episodes aligned at their peaks with significance determined by bootstrapping. Figure 4.4 shows the correlation between the SubNiño4 index over the anchor 3-month period and the SubT profiles with various lead/lag with significance determined by p-value. The patterns displayed in the 2 figures resemble each other, revealing the spatial-temporal evolution of equatorial Pacific ocean heat content during a generic ENSO cycle. The cycle begins around half a year before a subsurface warm/cold episode with a temperature anomaly centred westward of the SubNiño4 region and connected to the surface. The temperature anomaly then extends into the SubNiño4 region to establish a subsurface warm/cold episode while disconnecting itself from the surface. It then propagates eastwards and upwards along the climatological 20 °C isotherm fully decoupled from the surface. After around half a year, the subsurface temperature anomaly starts to leave the SubNiño4 region and spreads to the surface. 1 year from the subsurface



Figure 4.2: (a) Time series of the SubNiño4 and Niño3.4 indices. Subsurface warm (cold) events are indicated with pink (cyan) shading. (b) Frequency spectra of SubNiño4 and Niño3.4. The dashed lines indicate the 95-th percentile amplitude from an ensemble of 10000 AR(1) model simulations. (c) Normalised histogram of SubNiño4 and Niño3.4 with mean (μ), standard deviation (σ), skewness (g_1) and excess kurtosis (β_2). (d) Same as (c) but for Niño4-Z20 anomaly. (e) Same as (c) but for surface zonal wind stress anomaly over the Niño4 region. (f) Observation weights for SubT at 27 different points within the SubNiño4 region (grey) and the average (pink). The red line marks the beginning of 1979.

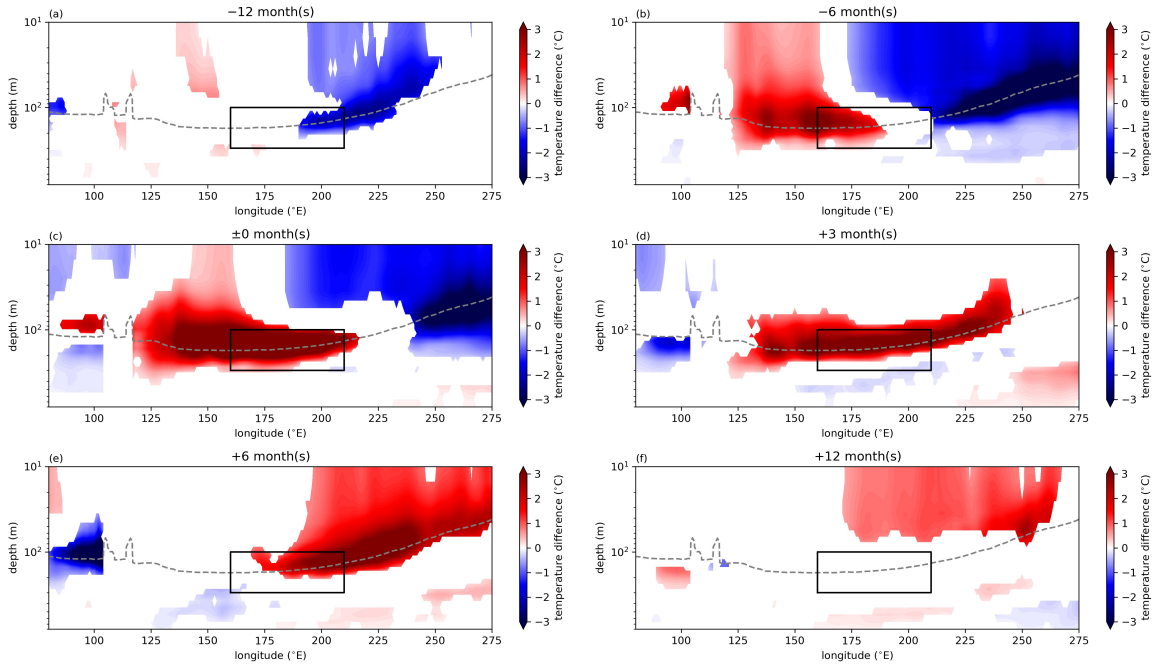


Figure 4.3: Composite difference of SubT profile averaged between 5° S and 5° N between subsurface warm and cold events with various lead/lag times. Only difference deemed significant at 95% confidence or above by bootstrapping with 5000 resamples is shown. The dashed grey line and the black box indicate the climatological 20 °C isotherm and the extent of the SubNiño4 region respectively. Anchor for subsurface warm events: February 1981, May 1986, March 1989, October 1989, February 1997, July 2004, December 2007, August 2018; anchor for subsurface cold events: August 1983, July 1987, February 1992, May 1993, January 1995, December 1997, March 2010, January 2016.

warm/cold episode, the temperature anomaly becomes disconnected from the isotherm and manifests itself as a purely surface temperature anomaly, replacing the temperature anomaly of opposite sign which existed there around 2 years ago.

Figure 4.5 shows the lagged correlations (r) of the SubNiño4 index and the WWV_W anomaly averaged over various 3-month periods with the Niño3.4 index averaged over each of the 4 main seasons. For a broad time window 1 year ahead of each main season, the SubNiño4 index is significantly correlated with the Niño3.4 index over the main season. This long-range correlation is robust across the 4 main seasons and various lead-times, with the correlation coefficient generally staying above 0.4. The correlation between WWV_W anomaly and Niño3.4 is less robust, especially at shorter lead-times. It is however similar to SubNiño4 at time scales of about 1 year. Not only does this show that SubT anomalies in the equatorial West Pacific precede SST anomalies further east, confirming the delayed connection between the subsurface and surface temperature anomalies hinted at in Figure 4.2 (a) and observed in the generic deseasonalised cycle shown in Figures 4.3

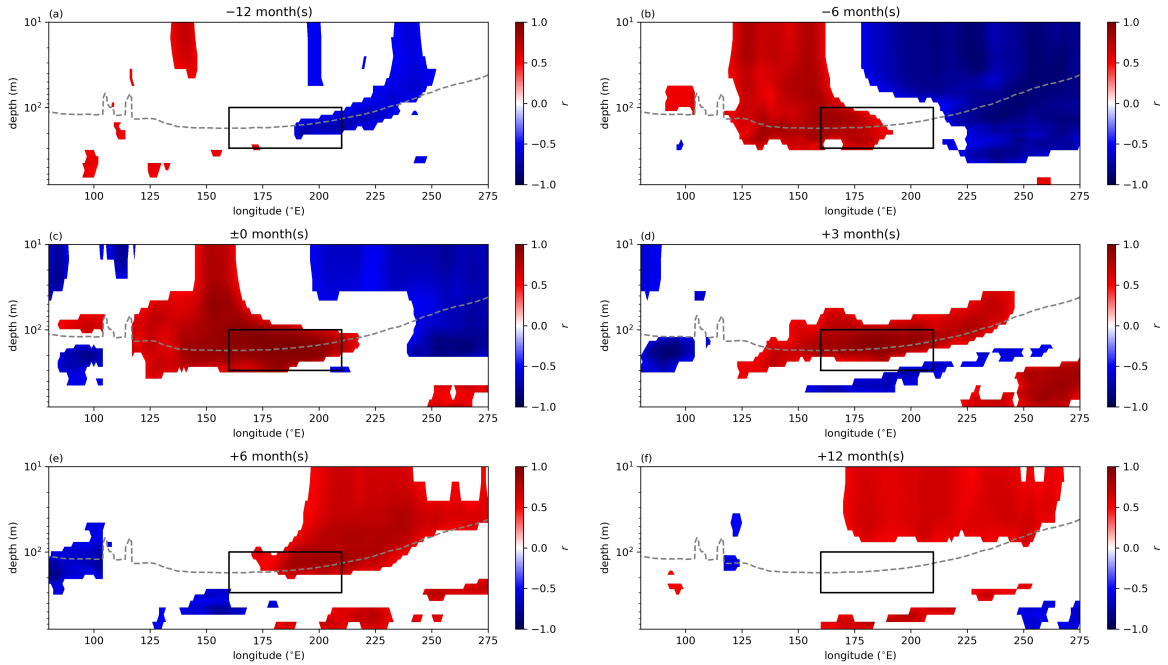


Figure 4.4: Similar to Figure 4.3 but showing correlation ($p < 0.05$) between the SubNiño4 index and SubT profile averaged between 5° S and 5° N with various lead/lag times from the peak of subsurface warm/cold events.

and 4.4, it also suggests that the SubNiño4 index is a simple indicator more robust with time than WWV_W anomaly for ENSO and hence atmospheric phenomena driven by it. SubNiño4 has very similar correlation also with Niño3, Niño3.4 and Niño4 (e.g. 0.40, 0.46 and 0.48 respectively at 12 months lead-time for DJF).

4.3.2 Delayed teleconnections of SubNiño4

4.3.2.1 Regional precipitation

The lagged correlation maps between the precipitation in the 4 main seasons and the SubNiño4 index 1 year ahead of each are shown in Figure 4.6. The most conspicuous feature is the year-round anti-correlation over Southeast Asia. There is also a clear anti-correlation signal during the boreal spring (MAM) in Northeast Brazil extending eastwards into the Atlantic.

Figures 4.7 to 4.11 show the lagged squared correlation coefficients (r^2) between various regional precipitations and the Niño3.4 index, the SubNiño4 index and the WWV_W anomaly to better exhibit, by removing the sign, the handover of significant correlation with precipitation from the subsurface to the surface. Corresponding plots showing the

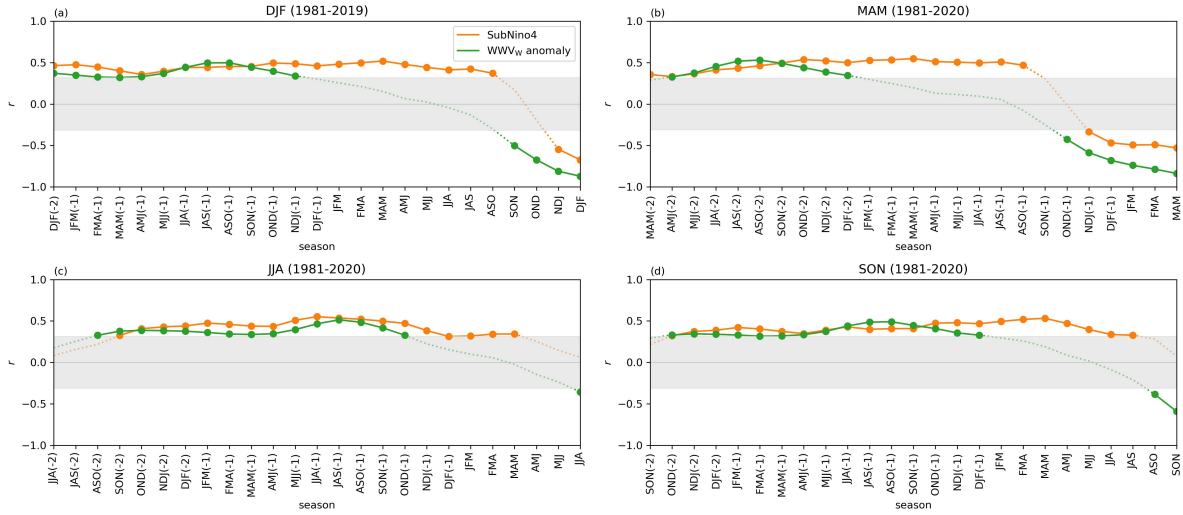


Figure 4.5: (a) Correlation, r, between Niño3.4 in DJF and SubNiño4 (orange) and WWV_W anomaly (green) in the 25 overlapping 3-month periods immediately prior. (b) Same as (a) but for MAM. (c) Same as (a) but for JJA. (d) Same as (a) but for SON. (a–d) Correlations with $p < 0.05$ are indicated with solid dot markers and connected with solid line. Grey shading indicates correlation levels with $p \geq 0.05$.

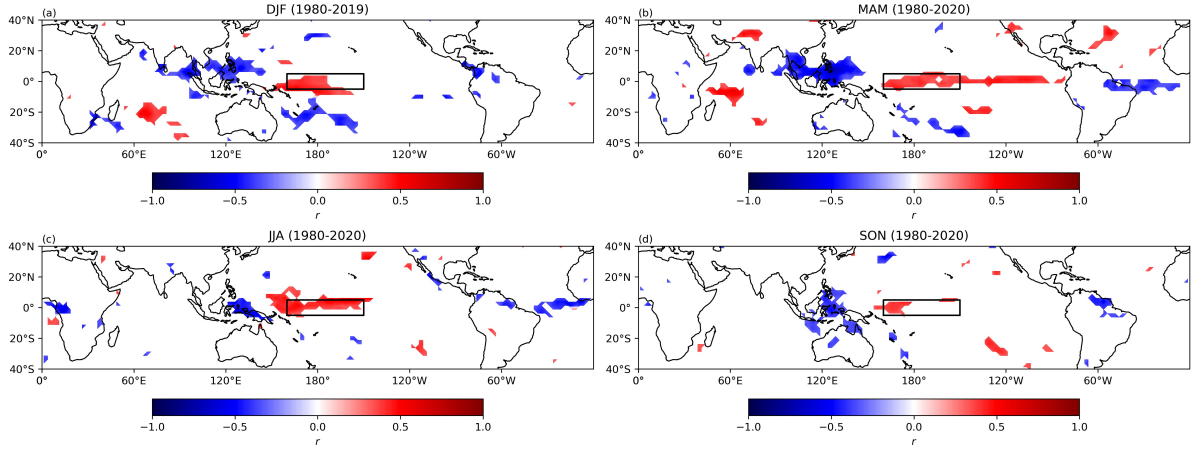


Figure 4.6: (a) Correlation ($p < 0.05$) between precipitation in DFJ and the SubNiño4 index 12 months prior. (b) Same as (a) but for MAM. (c) Same as (a) but for JJA. (d) Same as (a) but for SON. (a–d) The black box indicates the extent of the SubNiño4 region.

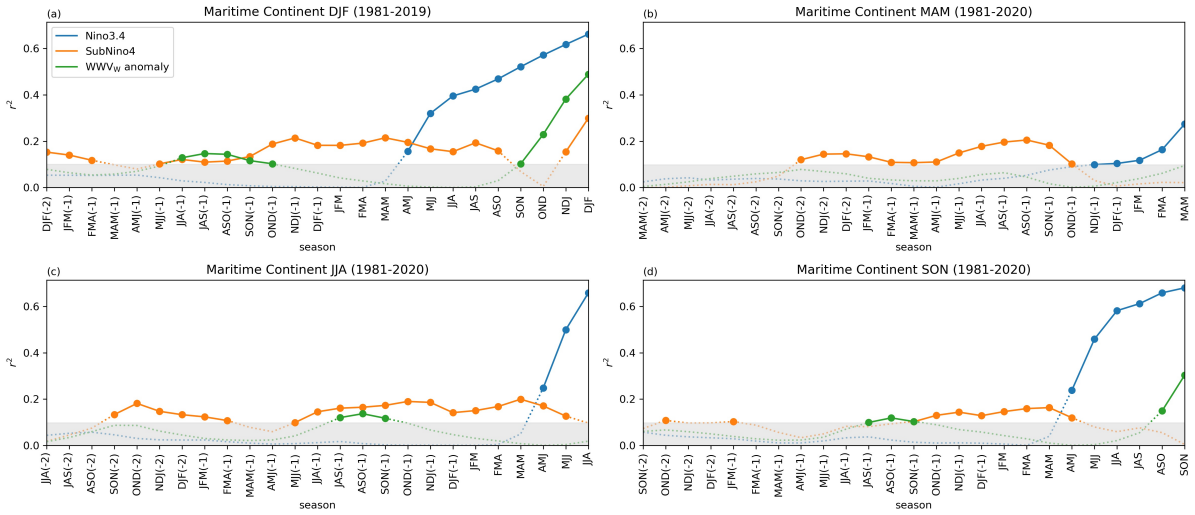


Figure 4.7: (a) Correlation, r^2, between Maritime Continent precipitation in DJF and SubNiño4 (orange), WWV_W anomaly (green) and Niño3.4 (blue) in the 25 overlapping 3-month periods immediately prior. (b) Same as (a) but for MAM. (c) Same as (a) but for JJA. (d) Same as (a) but for SON. (a–d) Correlations with $p < 0.05$ are indicated with solid dot markers and connected with solid line. Grey shading indicates correlation levels with $p \geq 0.05$.

correlation coefficients without squaring are included in Appendix A (Figures A.1 to A.5).

Figure 4.7 shows the squared correlation coefficients (r^2) between the precipitation over the Maritime Continent in the 4 main seasons and the Niño3.4 index, the SubNiño4 index and the WWV_W anomaly in the 25 overlapping 3-month periods leading up to each of the 4 main seasons. SubNiño4 becomes significantly correlated with precipitation much earlier than Niño3.4. The correlations between SubNiño4 around 6 to 12 months ahead and precipitation in all 4 main seasons stand at a level of around -0.4. The WWV_W anomaly in general gives weaker correlations than SubNiño4 with precipitation in all 4 main seasons. It fails to correlate significantly with precipitation in MAM while in the other 3 main seasons significance is sustained over a much smaller window of lead-times compared to SubNiño4. Meanwhile, the simultaneous correlations between Niño3.4 and precipitation in DJF, JJA and SON all exceed $r = -0.81$ ($p < 0.01$) while that in MAM is at $r = -0.52$ ($p < 0.01$). The simultaneous correlation with Niño3.4 in MAM is particularly lower than those in the other 3 main seasons while the lagged correlations with SubNiño4 are similar across all 4 main seasons, being least robust in SON.

Figure 4.8 shows the squared correlation coefficients (r^2) between the precipitation over Northeast Brazil and South Africa in MAM and DJFM respectively and the Niño3.4 index, the SubNiño4 index and the WWV_W anomaly in the 25 overlapping 3-month periods leading

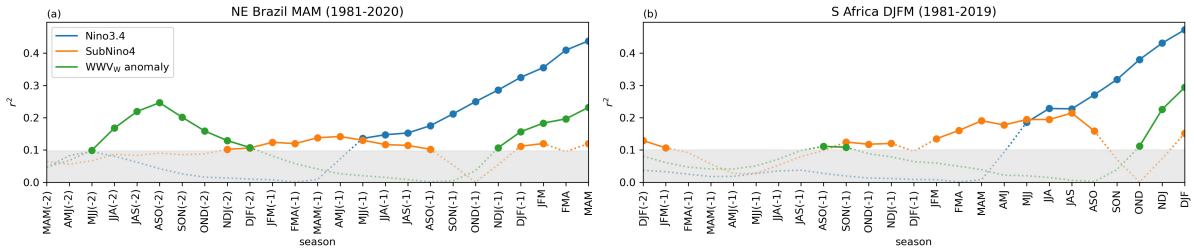


Figure 4.8: (a) Same as Figure 4.7 (a) but for Northeast Brazil precipitation in MAM. (b) Same as (a) but for South Africa precipitation in DJFM.

up to the precipitation seasons considered. In both cases, SubNiño4 becomes significantly correlated with precipitation around 15 months ahead of the relevant precipitation season, half a year earlier than Niño3.4. At long lead-times, the WWV_W anomaly is significantly correlated with the precipitation over Northeast Brazil in MAM from nearly 2 years earlier, but then SubNiño4 has stronger correlations at around 1 year lead. Only SubNiño4 shows robust significant correlation with the precipitation over South Africa in DJFM. The simultaneous correlations between Niño3.4 and precipitation in Northeast Brazil and South Africa are $r = -0.66$ ($p < 0.01$) and $r = -0.69$ ($p < 0.01$) respectively; while the lagged correlations with SubNiño4 around 1 year ahead stand at a level of about -0.35.

Figure 4.9 shows the squared correlation coefficients (r^2) between the precipitation over 2 regions in West Africa — the Gulf of Guinea and Sahel — in JJAS and the Niño3.4 index, the SubNiño4 index and the WWV_W anomaly in the 25 overlapping 3-month periods leading up to the precipitation season considered. In both regions, Niño3.4 becomes significantly correlated with the precipitation in JJAS 2 months ahead, remaining at a level of around -0.4. Interestingly, for the Gulf of Guinea, the precipitation is also significantly correlated to Niño3.4 more than 19 months ahead at a level of around 0.4. The precipitation over the Gulf of Guinea shows significant correlation with SubNiño4 10 to 21 months ahead ranging from $r = -0.32$ ($p < 0.05$) to $r = -0.47$ ($p < 0.01$). The correlation pattern with the WWV_W anomaly is similar to that of SubNiño4 but shifted earlier by 2 months. Meanwhile, the precipitation over Sahel does not show robust significant correlation with either SubNiño4 or the WWV_W anomaly.

Figure 4.10 shows the squared correlation coefficients (r^2) between the precipitation over East Africa during the so-called short rains (OND) and long rains (MAM) seasons and the Niño3.4 index, the SubNiño4 index and the WWV_W anomaly in the 25 overlapping 3-month periods leading up to the 2 precipitation seasons. For the short rains season,

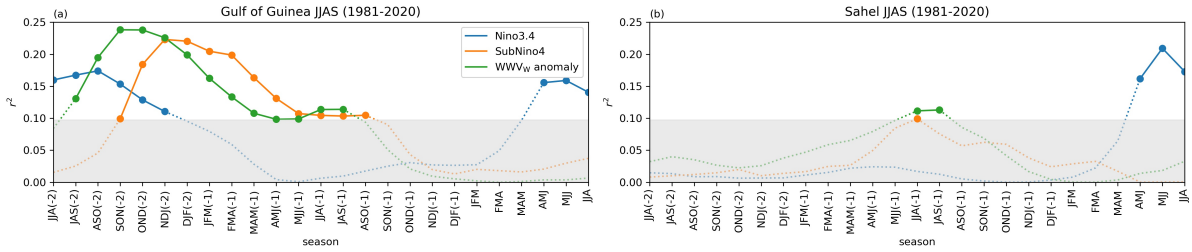


Figure 4.9: (a) Same as Figure 4.7 (a) but for Gulf of Guinea precipitation in JJAS. (b) Same as (a) but for Sahel precipitation.

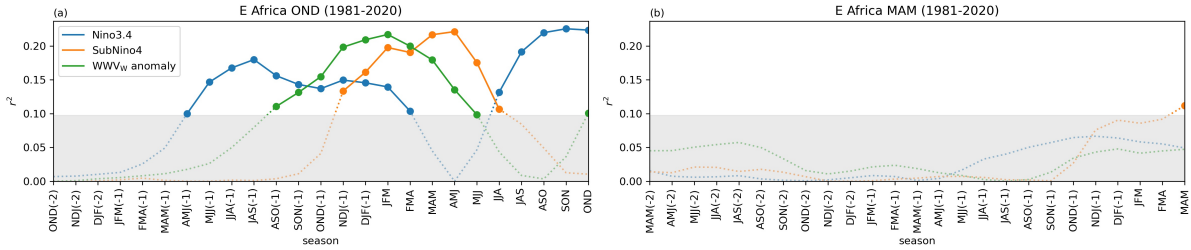


Figure 4.10: (a) Same as Figure 4.7 (a) but for East Africa precipitation in OND. (b) Same as (a) but for MAM.

the simultaneous correlation between precipitation and Niño3.4 is $r = 0.47$ ($p < 0.01$). The precipitation also shows significant correlation with SubNiño4 4 to 11 months ahead ranging from $r = 0.33$ ($p < 0.05$) to $r = 0.47$ ($p < 0.01$) and with Niño3.4 8 to 18 months ahead ranging from $r = -0.32$ ($p < 0.05$) to $r = -0.42$ ($p < 0.01$). The correlation pattern with the WWV_W anomaly is similar to that of SubNiño4 but shifted earlier by 2 months. On the other hand, there are no robust significant correlations between long rains season precipitation and either Niño3.4, SubNiño4 or the WWV_W anomaly.

Figure 4.11 shows the squared correlation coefficients (r^2) between the precipitation over India in JJAS and the Niño3.4 index, the SubNiño4 index and the WWV_W anomaly in the 25 overlapping 3-month periods leading up to the precipitation season considered, computed using data from 1960 to 2016 (Figure 4.11 (a)) and from 1979 to 2016 (Figure 4.11 (b)). Since the IITM all-India dataset is only available up to 2016, it is not possible to keep the same period of study as the other regional precipitations. With data from 1960 to 2016, the simultaneous correlation between precipitation and Niño3.4 is $r = -0.56$ ($p < 0.01$). The precipitation also shows significant correlation with SubNiño4 0 to 7 months ahead ranging from $r = -0.27$ ($p < 0.05$) to $r = -0.31$ ($p < 0.05$) and with Niño3.4 10 to 15 months ahead ranging from $r = 0.27$ ($p < 0.05$) to $r = 0.37$ ($p < 0.01$). The WWV_W anomaly gives significant correlation with the precipitation at lead-times of

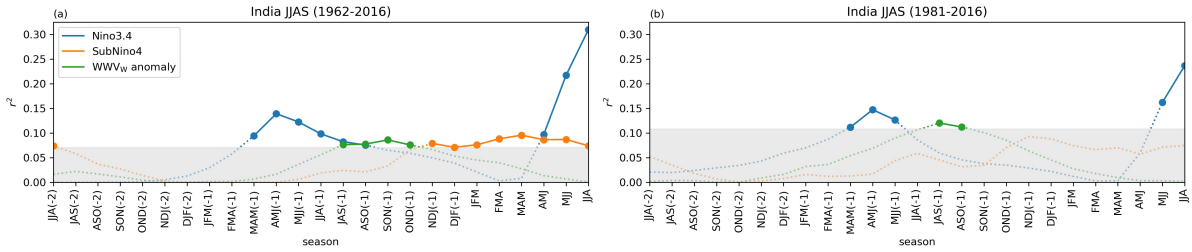


Figure 4.11: (a) Same as Figure 4.7 (a) but for India precipitation in JJAS computed with data from 1960 to 2016. (b) Same as (a) but computed with data from 1979 to 2016.

around 10 months. With data from 1979 to 2016, the simultaneous correlation between precipitation and Niño3.4 is slightly lower ($r = -0.47$, $p < 0.01$). The correlations with SubNiño4 however are similar to those computed with data from 1960 to 2016. Nonetheless, they are not deemed statistically significant mostly due to a reduction in sample size.

In general, for all cases where there is significant simultaneous correlation between precipitation and Niño3.4 except for Sahel JJAS, the correlations between precipitation and SubNiño4 become significant before Niño3.4; moving closer to the precipitation seasons considered, correlations with Niño3.4 kick in while those with SubNiño4 fade. Around 6 to 12 months (or even further into the past) prior to the precipitation seasons considered, correlations with SubNiño4 are significant but not with Niño3.4. The WWV_W anomaly gives weaker, less robust and less reliable correlation with precipitation overall. It leads earlier than SubNiño4 in some cases but can fail completely for some others. For consistency, the results presented are for precipitation regions and seasons based on, if not taken directly from, existing studies. It is worthwhile to note that both the regions and seasons could be further fine-tuned to achieve higher correlations with both surface and subsurface signals. The main purpose of this study however is to confirm the existence of basic robust relationships.

4.3.2.2 Fires in Southeast Asia

The relationship of SubNiño4 with fire, which has high impact and is partially linked to precipitation, is next explored. Figure 4.12 (a) shows the average annual fire count from 2001 to 2018 over Southeast Asia. Continental and Maritime Southeast Asia, with most of the fire captured by the red and purple boxes respectively, have distinct fire seasonal cycles. Since MODIS fire data only cover 2001 to 2018, to keep the period of study same as

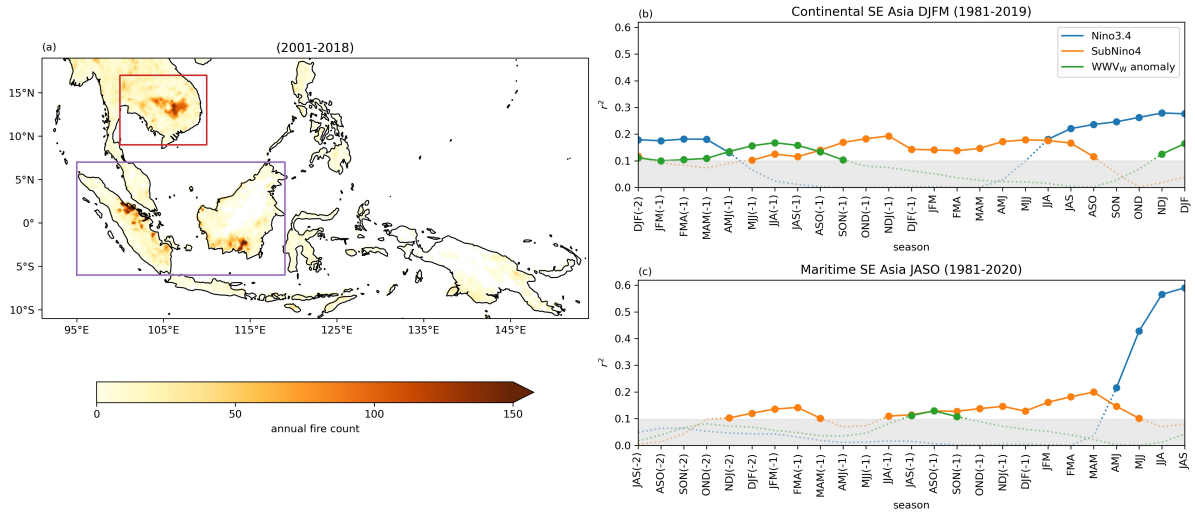


Figure 4.12: (a) Annual mean fire count over Southeast Asia. The red and purple boxes are for Continental and Maritime Southeast Asia respectively. (b) Same as Figure 4.7 (a) but for Continental Southeast Asia FWI in DJFM. (c) Same as (b) but for Maritime Southeast Asia FWI in JASO.

that for precipitation, the FWI produced from ERA5 data is used. The FWI seasonal cycles of Continental and Maritime Southeast Asia peak in DJFM and July to October (JASO) respectively. For the period when both MODIS and FWI data are available, the fire count and FWI are highly correlated — Continental Southeast Asia DJFM (annual): $r = 0.84$, $p < 0.01$ ($r = 0.88$, $p < 0.01$); Maritime Southeast Asia JASO (annual): $r = 0.96$, $p < 0.01$ ($r = 0.89$, $p < 0.01$).

Figure 4.12 (b–c) shows the squared correlation coefficients (r^2) between the FWI for Continental and Maritime Southeast Asia in DJFM and JASO respectively and the Niño3.4 index, the SubNiño4 index and the WWV_W anomaly in the 25 overlapping 3-month periods leading up to the fire seasons considered. Here, r^2 are shown to again exhibit more clearly the handover of significant correlation from the subsurface to the surface than showing r as in Appendix A (Figure A.6). For Continental Southeast Asia, the simultaneous correlation between Niño3.4 and FWI in DJFM is $r = 0.53$ ($p < 0.01$). The FWI also shows significant correlation with SubNiño4 4 to 19 months ahead ranging from $r = 0.32$ ($p < 0.05$) to $r = 0.44$ ($p < 0.01$) and with the WWV_W anomaly at lead-times of around 18 months at a lower level overall. For Maritime Southeast Asia, the simultaneous correlation between Niño3.4 and FWI in JASO is $r = 0.77$ ($p < 0.01$). The FWI also shows significant correlation with SubNiño4 2 to 20 months ahead ranging from $r = 0.31$ ($p < 0.05$) to $r = 0.45$ ($p < 0.01$) with a break at 14 and 15 months ahead and with the WWV_W anomaly 10 to

12 months ahead again at a lower level overall. Although the simultaneous correlation between Niño3.4 and FWI for Maritime Southeast Asia JASO is much higher than that for Continental Southeast Asia DJFM, the lagged correlations with SubNiño4 for the FWI in both cases are at a similar level.

4.4 Discussion

The SubNiño4 index, Niño4-Z20 anomaly and WWV_W anomaly are essentially measures of the same state of the ENSO cycle capturing the essential feature of the recharge cycle, specifically in the subsurface equatorial West Pacific on longer time scales. Izumo et al. (2019) showed that the variability of this state is primarily a consequence of wind-forced slow Rossby waves. It can be seen from Figure 4.2 (a) that the SubNiño4 index leads the Niño3.4 index. This is consistent with the lead relationship between the thermocline and surface ENSO variabilities established through, for example, studies of the WWV_W (Ballester et al. 2016, Izumo et al. 2019). Figure 4.2 (a) also shows that there is interdecadal variability in the relationship. The amplitude of the SubNiño4 index is much reduced post-2000, especially for cold anomalies, and has become less periodic compared to pre-2000. Furthermore, after 2000 the warm/cold events on the surface follow those in the subsurface less closely than before as reported previously by Zhao et al. (2021).

Composite analysis of subsurface warm and cold episodes (Figures 4.3 and 4.4) reveals how the subsurface temperature anomalies in the equatorial West Pacific evolve to become surface temperature anomalies in the equatorial East Pacific after around 6 to 12 months. The fact that the occurrence of the subsurface temperature anomaly in the west is accompanied by SST anomaly of the opposite sign in the east in the beginning (Figures 4.3 to 4.5) sheds light on how the subsurface temperature anomaly might have formed in the first place. A positive (negative) SST anomaly in the equatorial East Pacific is associated with a weakening (strengthening) of the easterly trade winds (Dijkstra 2006). Since the trade winds causes sea water to pile up along the eastern coasts of the equatorial Pacific, its weakening (strengthening) encourages (suppresses) upwelling and lifts (deepens) the thermocline there, leading to a negative (positive) temperature anomaly. Indeed, a positive (negative) SST anomaly in the east is associated with a negative (positive) thermocline depth anomaly in the west (Figure 2 in Dijkstra (2006)).

The evolution of the subsurface temperature anomalies observed following subsurface warm/cold episodes is consistent with that during a generic ENSO cycle as reported by others (e.g. Timmermann et al. 2018, Lin & Qian 2019). Such delayed connection between the subsurface and surface temperature anomalies is confirmed by correlation analysis between the SubNiño4 and Niño3.4 indices shown in Figure 4.5 and appears to be a robust year-round feature. Figure 4.5 also shows that the SubNiño4 index correlations are more stable with respect to lead-time than the widely used WWV_W. In particular, they decrease much less quickly at shorter lead-times than WWV_W. A further merit of the SubNiño4 index, or alternatively Niño4-Z20, over WWV_W is that unlike the latter, the (Sub)Niño4 region is completely free of land, making it more directly relevant to the ocean dynamics. The SubNiño4 index or Niño4-Z20 is a practical and stable index that captures well-known ENSO physics and can serve as a long-range indicator of surface ENSO and thus atmospheric phenomena driven by it.

The Fourier spectrum of the Niño3.4 index obtained here (Figure 4.2 (b)) is consistent with that in Petrova et al. (2017) for Niño3.4 and in Latif et al. (1998) and Rasmusson & Carpenter (1982) for Niño3. The dominant quasi-quadrennial peak and the secondary quasi-biennial peak are well-established features also present in the SubNiño4 spectrum here. The SubNiño4 index may be less noisy than the Niño3.4 index because of a lack of direct atmospheric coupling with the subsurface compared to the surface, making the SubT less prone to influences from high frequency or stochastic atmospheric forcings than the SST. The normalised histogram of the SubNiño4 index resembles that of the Niño4-Z20 anomaly (Figure 4.2 (c–d)); the two have similar negative skewness and are essentially interchangeable variables ($r = 0.99$, $p < 0.01$), effectively being equivalent measures of the thermocline-mixed layer interface. The surface zonal wind stress anomaly over the Niño4 region is positively skewed with lower absolute skewness than the SubNiño4 index and is significantly correlated to it in December and January only. The reason why the SubNiño4 index displays such pronounced (negative) skewness not exhibited by the Niño3.4 index is not clear but the skewed surface zonal wind stress anomaly (Planton et al. 2018) and subsurface nonlinear dynamical heating (e.g. Hayashi et al. 2020) may be contributing factors. Izumo et al. (2019) also noted the importance of multi-month integrated wind forcing rather than just considering single month correlations.

Dynamical ENSO predictions show both interdecadal (Zhang, Wang, Jiang & Ma 2021,

Barnston et al. 2012) and seasonal (Sun et al. 2018, Barnston et al. 2012, Jin et al. 2008) variations in predictive skill and different models are not always available at lead-times of more than 12 months. For those that are, the typical correlation skill is at the level of 0.5 on average for 12-month forecasts. At such a long lead-time, ENSO correlation with the lead observed SubNiño4 index (Figure 4.5) is on par with the simultaneous correlation from typical dynamical predictions. Together with the established ocean heat content advective processes necessary for the onset of El Niño (Timmermann et al. 2018, Ramesh & Murtugudde 2013, Ballester et al. 2016), this confirms that initialisation of equatorial Pacific SubT profile is a major source of long-range ENSO predictive skill from dynamical models. The importance of equatorial Pacific thermocline has been demonstrated by data assimilation and ensemble prediction methods that target optimal equatorial Pacific subsurface temperature disturbances for dynamical ENSO prediction (e.g. Yang et al. 2008, O'Kane et al. 2019). Furthermore, predictions of ENSO-driven atmospheric phenomena at such lead-times afforded by observed SubNiño4 index can be expected to be no worse than those by predicated SST from dynamical models. Takaya et al. (2021) demonstrated skilful long-range dynamical large ensemble monsoon predictions. They attributed the skill to SST anomalies and did not further explore the role of the Pacific subsurface highlighted here. It could be that it is their subsurface initialisation that is the dominant factor for their long-range skill. The potential of the SubNiño4 index is demonstrated here by establishing robust lagged correlations with regional precipitations and fires. One way to directly evaluate its performance against dynamically predicted ENSO is to compare the mutual information between the atmospheric response to be predicted and lead observed SubNiño4 and simultaneous dynamically predicted Niño3.4 respectively, provided that time series of predicted Niño3.4 are available. This reveals the amount of information about the atmospheric response to be predicted that can be learnt from the 2 predictors respectively.

ENSO's effects on precipitation has been studied on the global scale in detail by Lenssen et al. (2020), Davey et al. (2014), Ropelewski & Halpert (1987, 1989) and Kiladis & Diaz (1989) for example. They mapped out regions around the globe where the precipitation over various time windows are strongly and coherently correlated with ENSO. While it is neither aimed nor can it be expected that the correlation analysis here with global precipitation over the 4 main seasons and SubNiño4 with a very long lead-time of 12 months (Figure 4.6) will exactly reproduce the patterns identified by say Lenssen et al. (2020), it

suggests that the SubNiño4 index has strong potential as a long-range predictor for ENSO-driven precipitations.

The effects of ENSO on precipitations on a regional level have also been extensively studied. Some of the regions and seasons where ENSO is known to play an important role in their interannual precipitation variability are summarised as follows. Over the Maritime Continent, the precipitation and ENSO signal are anti-correlated throughout the year (As-Syakur et al. 2016, King & Vincent 2018, Yanto et al. 2016); in Northeast Brazil, the precipitation and ENSO signal are anti-correlated in the wet season (MAM) (Folland et al. 2001, Andreoli & Kayano 2006); in West Africa, the precipitation and ENSO signal are anti-correlated in the wet season (JJAS) (Srivastava et al. 2019, Losada et al. 2012); in South Africa, the precipitation and ENSO signal are anti-correlated in the wet season (DJFM) (Hoell et al. 2017, Yuan et al. 2014); in East Africa, the precipitation and ENSO signal are positively correlated in the so-called short rains season (OND) but have insignificant correlation in the so-called long rains season (MAM) (Mutai et al. 1998, Park et al. 2020, Vellinga & Milton 2018, Vigaud et al. 2017).

The simultaneous correlations between Niño3.4 and precipitation from the analysis here agree with all these reported ENSO-precipitation relationships. The lagged correlations between SubNiño4 and precipitation have the same sign as the simultaneous correlations with Niño3.4. As expected, the long-range correlation is generally smaller than that for in-season, but it is significant over many lead-times. In some cases, the long-range correlation is even as large as the in-season correlation.

It is worth noting that for the Maritime Continent, while the simultaneous correlation with Niño3.4 in MAM is particularly lower than those in the other 3 main seasons, consistent with the northward shift in ENSO influence in the region observed by As-Syakur et al. (2016), the lagged correlations with SubNiño4 are similar throughout the year, and is the least robust in SON. For West Africa JJAS, although the simultaneous correlations with Niño3.4 for both the Gulf of Guinea and Sahel are similar, the SubNiño4 index as an indicator is much more reliable and robust for the Gulf of Guinea than Sahel. Although the correlation analysis performed by Losada et al. (2012) employed Niño3 and their period of study stopped just before that in here, the simultaneous correlations between Niño3.4 and precipitation in the Gulf of Guinea and Sahel from the analysis here agree with the values towards the end of their study period. Losada et al. (2012) used Monte Carlo test

to determine significance and interestingly, towards the end of their study period, although the correlations between Niño3 and precipitation in the Gulf of Guinea and Sahel are at the same level, only the former was deemed significant. As for East Africa, significant simultaneous (lagged) correlations with Niño3.4 (SubNiño4) are observed for the short rains season (OND) but not for the long rains season (MAM) as expected, indicating that the SubNiño4 index correlates only when there is also significant simultaneous correlation with Niño3.4.

The correlation patterns of fire with Niño3.4 and SubNiño4 resemble those of precipitation. This verified that the SubNiño4 index is useful as an indicator not just of precipitations but other ENSO-driven anomalies in general as well. Sparks & Toumi (2020) originally proposed the Pacific subsurface heat content to be a predictor of South China tropical cyclone landfall because the index can anticipate changes in the steering level winds. SubNiño4 as a long-range predictor is therefore of potential interest to a broad range of atmospheric phenomena.

The domains and seasons chosen to study Southeast Asia fires do not correspond exactly to those used to study Maritime Continent precipitation. In particular, Maritime Southeast Asia represents only a small part of the Maritime Continent and Continental Southeast Asia is completely separate from the Maritime Continent. Nonetheless, the correlation patterns for fires in both cases appear to be consistent with those for precipitation. Maritime Southeast Asia fires are known to be strongly driven by local precipitation and ENSO (Fanin & van der Werf 2017, Wooster et al. 2012, Liew 2013). However, there is a lack of literature on the relation among Continental Southeast Asia fires, local precipitation and ENSO. In a global study on burnt area forecast with SST by Chen et al. (2016), among the 14 ocean climate indices considered, ENSO-related ones are optimal for correlation with the annual burnt area of 6 out of 12 hotspot regions identified. However, their clustering algorithm failed to capture the most severely burnt region in Continental Southeast Asia. The study here suggests that ENSO also plays a role in the regulation of fire activities over Continental Southeast Asia.

Compared with the SubNiño4 index, the correlations of WWV_W anomaly with the Niño3.4 index are similar in strength and have similar long lead-times but are less well sustained into shorter lead-times. The SubNiño4 index, Niño4-Z20 anomaly and WWV_W anomaly all essentially capture of the same state of the ENSO cycle. In this sense, the study here does not point to any novel fundamental aspects about the dynamics of ENSO. However, the

SubNiño4 index has temporally more stable and sustained and at times stronger correlations with the Niño3.4 index while covering a smaller domain compared with the WWV_W anomaly. It may therefore identify more precisely the critical point of action of the subsurface branch of established ENSO dynamics.

The implications of Pacific subsurface temperature anomaly on atmospheric anomalies, in particular regional precipitations throughout the tropics and fires in Southeast Asia, have been studied in detail here. The correlations of the WWV_W anomaly with the regional precipitation and fire investigated are overall weaker, less robust and sustained over less lead-times compared with the SubNiño4 index. In a few cases, the correlation patterns resemble those of SubNiño4 but with a slight shift towards longer lead-times. This is consistent with the eastward propagation of SubT anomaly in the equatorial Pacific and the WWV_W region being centred westward of the (Sub)Niño4 region. In many of the other cases, the WWV_W anomaly is less correlated with regional precipitation and fire over a smaller time window compared to SubNiño4. Sometimes the WWV_W anomaly dose not work at all when the SubNiño4 index is still a useful indicator. The utility of the WWV_W anomaly may also be limited because of its domain of definition, which could be problematic as it includes considerable land mass to the west. The (Sub)Niño4 region does not have this issue.

4.5 Conclusions

The SubNiño4 index originally proposed by Sparks & Toumi (2020) is extended and given a fuller investigation revealing its relation to surface Niño indices. It has been shown that the SubNiño4 index captures the evolution of subsurface ocean heat content between the El Niño and La Niña phases of the ENSO cycle, thus allowing it to serve as a long-range indicator of Niño3.4 and ENSO-driven atmospheric phenomena. It achieves this with temporally more stable correlations compared to the commonly used WWV_W anomaly. The ENSO correlation with the SubNiño4 index is demonstrated to match that with the WWV_W anomaly and becomes significant at around the same lead-time. However, the SubNiño4 correlation is sustained further into shorter lead-times. At lead-times of the order of 12 months, observed Niño3.4 correlations with the lead observed SubNiño4 index become similar to and can exceed those produced with typical dynamical model ENSO predictions. This study confirms that an important source of long-range predictive skill for ENSO in dynamical

models can be understood to stem from good initialisation of the subsurface temperature profile in the western equatorial Pacific. The potential value and viability of the SubNiño4 index as a long-range indicator of atmospheric phenomena driven by ENSO, particularly regional precipitation anomalies throughout the tropics and fires in Continental and Maritime Southeast Asia, is further established.

Chapter 5

The Effects of Changing Surface Conditions on the Boundary Layer Structure of Weak Tropical Cyclones Near Landfall

5.1 Introduction

The vertical profile and azimuthal asymmetry of tropical cyclones in the boundary layer and above have been studied (e.g. Kepert 2001, Kepert & Wang 2001, Shapiro 1983, Ren et al. 2019, Thomsen et al. 2015, Knupp et al. 2000). Zhang & Uhlhorn (2012) and Zhang, Li, Perrie & Zhang (2021) focused on the surface; Rogers et al. (2013), Liao et al. (2019) and He et al. (2022) studied the effects of cyclone intensity change; while Powell (1982), Knupp et al. (2006) and Hlywiak & Nolan (2022) studied the effects of landfall. These studies, with the exception of Knupp et al. (2006), mostly involve relatively strong cyclones at or above Category 1 on the Saffir-Simpson hurricane wind scale (hereafter TC). Because of the greater risks stronger cyclones pose to society, it is understandable that weaker cyclones receive somewhat less attention in the tropical cyclone research community. When there is a lack of study focused on weak cyclones, it is tempting to just extrapolate results form corresponding studies focused on strong cyclones. However, tropical cyclone properties may not follow a linear relation with respect to intensity, and may even be bifurcated between weak and strong cyclones. Therefore, there is a need to study weak cyclones despite

their being less impactful to society in general. Inflow is a fundamental property of tropical cyclones and is associated to their evolution (e.g. Wang & Toumi 2022, Sparks & Toumi 2022*b*,*a*). Both the wind speed and the inflow angle contribute to the radial velocity, all 3 of which are standard variables to consider when studying tropical cyclone inflow. Here, their vertical profiles within the boundary layer will be studied, focusing on tropical cyclones with intensities at Tropical Storm (TS) level. The existence of structural differences among intensifying, steady-state and decaying TSs near landfall will be explored. The goal is to identify the dominating factor affecting the boundary layer profile of relatively weak tropical cyclones near landfall and any qualitative difference in their behaviour to stronger systems.

Shapiro (1983) observed stronger winds on the left of translating TCs with maximum inflow in the front-right quadrant. Ren et al. (2019) reported that the low-level radial velocity is larger in the front and the inflow layer depths in all 4 quadrants are well below 1500 m, ranging from below 500 m to slightly over 1000 m. Knupp et al. (2000) observed strong inflow below 1000 m for Hurricane Georges (1998) at landfall. In the cyclone motion-relative frame of reference, Zhang & Uhlhorn (2012) reported an average near-surface inflow angle between 18° and 30° with azimuthal asymmetry that grows in amplitude and shifts counterclockwise in phase as cyclone translation speed increases but not very sensitive to cyclone intensity. At low translation speeds, the largest (smallest) inflow angle is found in the rear-right (front-left).

Rogers et al. (2013) reported that intensifying TCs show stronger near-surface inflow and have deeper inflow layer compared to steady-state ones. This is consistent with Kepert (2001) that inertially less stable cyclones have larger depth scales. In the observations of Liao et al. (2019), intensifying cyclones are characterised by a boundary layer either dominated by inflow or with inflow that strengthens towards the cyclone centre; while weakening cyclones by a boundary layer dominated by outflow. On the other hand, He et al. (2022) observed weak inflow in the boundary layer of the weakening TS Khanun (2017). The inlfow angle is also important in controlling the size of cyclones (Wang & Toumi 2022).

Powell (1982) observed from the landfalling Hurricane Frederic (1979) that landfall shifts the region of maximum inflow angle from the rear-right to the landward side due to increased surface friction over land. Knupp et al. (2006) studied TS Gabrielle (2001) during

landfall and reported that changes in the boundary layer wind profile occurred within 5 km of the upstream side of the coastline. Hlywiak & Nolan (2022) performed simulations of TCs making perpendicular landfall with a straight coastline. They found high inflow angle and weakening winds over land, and an enhanced and deepened inflow layer in the offshore flow. These are attributed to the difference in surface friction over land (high) and water (low). The described responses begin 6 to 9 hours before landfall when the cyclone is about 200 km from land.

Based on wind profiler measurements provided by the HKO, a new perspective is introduced in this chapter regarding the boundary layer structural differences among intensifying, steady-state and decaying TSs near landfall as manifested in their vertical profiles of wind speed, inflow angle and radial velocity. It is found that intensifying and steady-state TSs have fairly similar boundary layer wind profiles which are distinct from that of decaying TSs closer to land. The decaying TSs have stronger inflow in the middle to bottom of the boundary layer mainly driven by higher inflow angle under near identical reduction in wind speed from the top of the boundary layer compared to intensifying and steady-state TSs. It is likely that such differences in the behaviour of decaying TSs to that of intensifying and steady-state TSs arise from the effects of enhanced surface friction due to their proximity to land.

5.2 Methods

In total, 690 HKO wind profiler measurements taken from 12 individual cyclones over the 10-year observation period from 2010 to 2019 entered into this study. Figure 5.1 shows the spatial distribution of cyclone centre at the times of measurement. Summary statistics of the corresponding cyclone properties are shown in Tables 5.1 to 5.4. The data are sorted into quadrants and classified by intensity and intensification rate as explained later. Notice that the intensifying and steady-state cyclones are located further away from land while the decaying cyclones are considerably closer to or even over land when measurements were taken. This point is further illustrated in Figure B.1, which shows the TS data classified by the cyclone centre's distance to land with a threshold of 80 km. In addition, the measurements are biased in terms of azimuthal angle relative to cyclone translation direction, with the majority having been taken in the front-left.

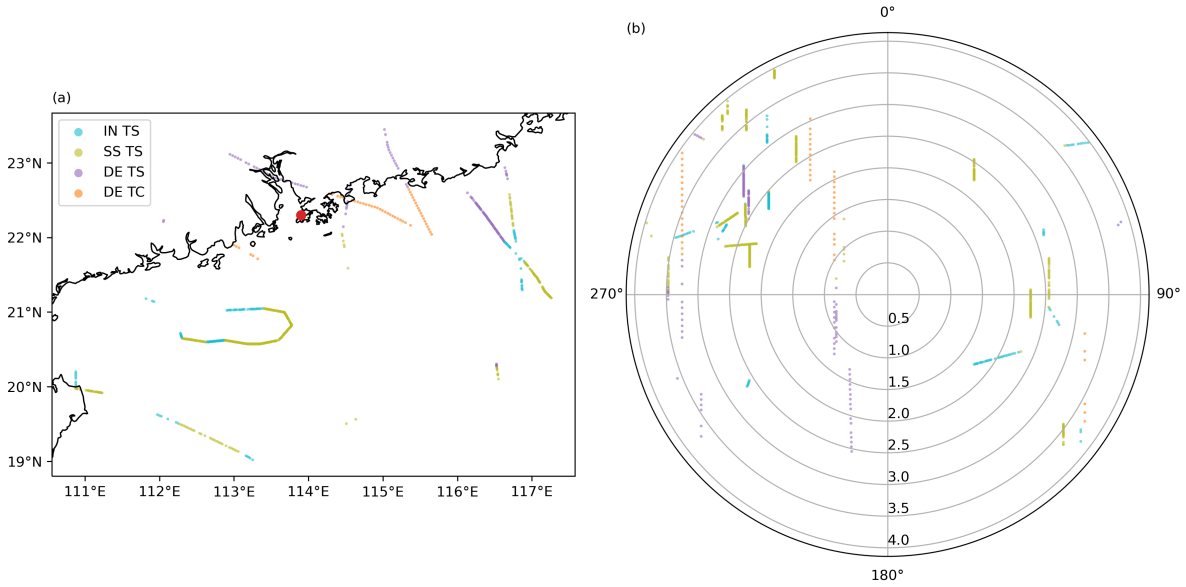


Figure 5.1: Spatial distribution of wind profiler samples, classified into intensifying (IN) TS, steady-state (SS) TS, decaying (DE) TS and DE TC. (a) Geographic location of cyclone centre at the time of measurement. Location of the Sha Lo Wan weather station is indicated by the red dot. (b) Azimuthal angle (relative to the direction of cyclone translation) and distance (normalised by R_{max}) of the Sha Lo Wan weather station from cyclone centre at the time of measurement.

	n	cyclone	V_{max} (kt)			r			V_{trans} ($m\,s^{-1}$)		
			min	median	max	min	median	max	min	median	max
ALL	131	5	34	41	50	1.8	2.6	4.0	1.2	2.3	5.3
FR	**14**	**1**	**34**	**40**	**41**	**2.6**	**3.7**	**4.0**	**3.8**	**4.2**	**4.2**
RR	**37**	**3**	**34**	**42**	**45**	**1.8**	**2.0**	**3.8**	**2.5**	**2.5**	**5.3**
RL	7	1	34	34	35	2.6	2.6	2.7	1.9	1.9	1.9
FL	**73**	**3**	**35**	**40**	**50**	**2.3**	**2.7**	**3.5**	**1.2**	**1.6**	**2.7**

Table 5.1: Intensifying TS measurements summary statistics. Bold for quadrants with at least 10 samples.

	n	cyclone	V_{max} (kt)			r			V_{trans} ($m\,s^{-1}$)		
			min	median	max	min	median	max	min	median	max
ALL	384	7	35	40	60	0.9	2.6	4.0	0.8	1.3	5.3
FR	**61**	**2**	**35**	**40**	**40**	**2.3**	**2.5**	**3.7**	**1.0**	**1.0**	**4.6**
RR	**56**	**2**	**35**	**40**	**40**	**2.3**	**2.3**	**3.7**	**1.3**	**1.7**	**5.3**
RL	0	0	–	–	–	–	–	–	–	–	–
FL	**267**	**6**	**35**	**40**	**60**	**0.9**	**2.7**	**4.0**	**0.8**	**1.3**	**4.6**

Table 5.2: Steady-state TS measurements summary statistics. Bold for quadrants with at least 10 samples.

	n	cyclone	$V_{\max}$ (kt)			r			V_{trans} ($\mathrm{m\,s^{-1}}$)		
			min	median	max	min	median	max	min	median	max
ALL	124	7	34	44	64	0.8	2.8	4.0	1.4	2.7	7.3
FR	2	1	34	34	34	3.8	3.8	3.9	2.9	2.9	2.9
RR	0	0	—	—	—	—	—	—	—	—	—
RL	**53**	**4**	**38**	**58**	**63**	**0.8**	**1.7**	**3.7**	**2.6**	**6.9**	**7.3**
FL	**69**	**5**	**35**	**42**	**64**	**0.8**	**2.8**	**4.0**	**1.4**	**2.2**	**7.3**

Table 5.3: Decaying TS measurements summary statistics. Bold for quadrants with at least 10 samples.

	n	cyclone	$V_{\max}$ (kt)			r			V_{trans} ($\mathrm{m\,s^{-1}}$)		
			min	median	max	min	median	max	min	median	max
ALL	51	3	64	69	114	1.0	2.9	3.9	6.4	6.9	7.3
FR	0	0	—	—	—	—	—	—	—	—	—
RR	6	1	106	110	114	3.2	3.4	3.7	6.4	6.4	6.4
RL	0	0	—	—	—	—	—	—	—	—	—
FL	**45**	**2**	**64**	**68**	**74**	**1.0**	**2.7**	**3.9**	**6.7**	**6.9**	**7.3**

Table 5.4: Decaying TC measurements summary statistics. Bold for quadrants with at least 10 samples.

All boundary layer profiles are considered in a frame of reference translating with the cyclone and are obtained from the wind velocities $(\tilde{u}, \tilde{v})$ after subtracting the cyclone translation velocity determined using IBTrACS data from the wind velocities (u, v) measured by the wind profiler. For each measured wind profile, at a certain altitude the full wind speed is the magnitude of the wind velocity at that altitude while the radial velocity is the component along the direction pointing from the cyclone centre to the weather station (negative for inflow). The inflow angle α at altitude h is computed using

$$\alpha(h) = -\operatorname{atan2}[\tilde{v}(h), \tilde{u}(h)] - \Phi, \tag{5.1}$$

mapped onto $(-180°, 180°]$, where Φ is the compass bearing from the weather station to the cyclone centre. This gives the angle of deviation of the wind from the tangential direction relative to the cyclone centre (negative for anticlockwise deviation, i.e. inflow in the Northern Hemisphere). The reduction factor ξ at altitude h is computed with respect to a

reference altitude h_{ref} according to

$$\xi(h) = \sqrt{\frac{[\tilde{u}(h)]^2 + [\tilde{v}(h)]^2}{[\tilde{u}(h_{\text{ref}})]^2 + [\tilde{v}(h_{\text{ref}})]^2}}. \tag{5.2}$$

It describes the ratio by which the wind speed has reduced between h_{ref} and h. A proper h_{ref} should be set high enough so that all measured wind profiles are near geostrophic at h_{ref}. If this is the case, ξ should be near constant around h_{ref}. Throughout this study, h_{ref} is set to be 1250 m, which is justified retrospectively. By doing so, the chosen h_{ref} is implicitly considered to be representative of the boundary layer height, which is reasonable (Ren et al. 2019).

The processed boundary layer profiles are grouped by whether at the time of measurement the cyclone is weak (TS intensity, $34\,\text{kt} \leq V_{\text{max}} < 64\,\text{kt}$) or strong (TC intensity, $V_{\text{max}} \geq 64\,\text{kt}$) and whether the cyclone is intensifying, in steady-state or decaying. Following Rogers et al. (2013), the cyclone is deemed intensifying (decaying) if V_{max} is increasing (decreasing) faster than $20\,\text{kt}\,\text{day}^{-1}$ and in steady-state if V_{max} is changing at a rate between $\pm 10\,\text{kt}\,\text{day}^{-1}$. The individual boundary layer profiles of the same variable are then composited by averaging. To account for the azimuthal asymmetry of translating cyclones and the directional bias in sampling, both full-sample average and individual quadrant averages are considered. For full-sample average, at each altitude the arithmetic mean with equal weight is taken across all individual profiles with available data. For individual quadrant averages, the arithmetic means are computed similarly but separately for profiles measured with the weather station respectively located in the front-right, rear-right, rear-left and front-left of the cyclone relative to translation direction. Throughout this study, data points averaged from less than 10 individual boundary layer profiles are discarded. The analysis is repeated on just the profiles from TSs sorted by distance to land.

5.3 Results

The inflow angle, reduction factor and radial velocity boundary layer profiles are computed from the HKO wind profiler measurements. Based on the data available, only the full-sample and front-left quadrant averages of intensifying TS, steady-state TS, decaying TS and decaying TC are compared. While the full-sample averages generally agree with the

front-left quadrant averages, due to the azimuthal asymmetry and sampling bias, the front-left quadrant averages should be more reliable quantitatively.

As can be seen from Figure 5.2, the boundary layer inflow angle profiles of intensifying and steady-state TS are fairly similar while that of decaying TS stands out. The full-sample average (Figure 5.2 (a)) suggests that the inflow angle of decaying TS at 200 m is nearly double that of intensifying and steady-state TS. This approximate doubling of inflow angle towards the bottom of the boundary layer is confirmed by the front-left quadrant analysis (Figure 5.2 (b)). There, it is seen that the inflow angle of intensifying TS remains fairly constant at around 20° throughout much of the boundary layer. It increases to around 30° as altitude descends from 600 m to 200 m. The inflow angle of steady-state TS is around 28° towards the top of the boundary layer. Descending into the boundary layer, it decreases to converge with intensifying TS at around 1100 m and remains close to intensifying TS down to around 600 m. It then increases more steeply than intensifying TS to around 46° as altitude further descends to 200 m. As for decaying TS, its inflow angle is similar to those of intensifying and steady-state TS towards the top of the boundary layer and increases throughout the boundary layer to around 80° as altitude descends to 200 m. Although there is a lack of data nearer the surface, it seems likely that decaying TS will also have a much larger near-surface inflow angle than intensifying and steady-state TS.

Despite marked differences in the boundary layer inflow angle profile of decaying TS from intensifying and steady-state TS, Figure 5.3 (a) shows similar boundary layer reduction factor profile for all intensifying, steady-state and decaying TS. The similarity is even more striking if one focuses on the front-left quadrant (Figure 5.3 (b)). Staying at around 1 above the reference altitude of 1250 m, the reduction factor decreases at a fairly constant rate below to around 0.55 as altitude descends to 200 m.

Figure 5.4 shows the boundary layer radial velocity profiles of intensifying, steady-state and decaying TS. As would be expected based on the inflow angle and reduction factor profiles (Figures 5.2 and 5.3), the radial velocity profiles of intensifying and steady-state TS are fairly similar while that of decaying TS stands out. The radial velocities of intensifying, steady-state and decaying TS appear to have similar values, especially taking uncertainties into account, towards the top of the boundary layer. Those of intensifying and steady-state TS generally decrease throughout the boundary layer as altitude descends to 200 m. Over the same altitude range, the radial velocity of decaying TS tends to increase, showing sign

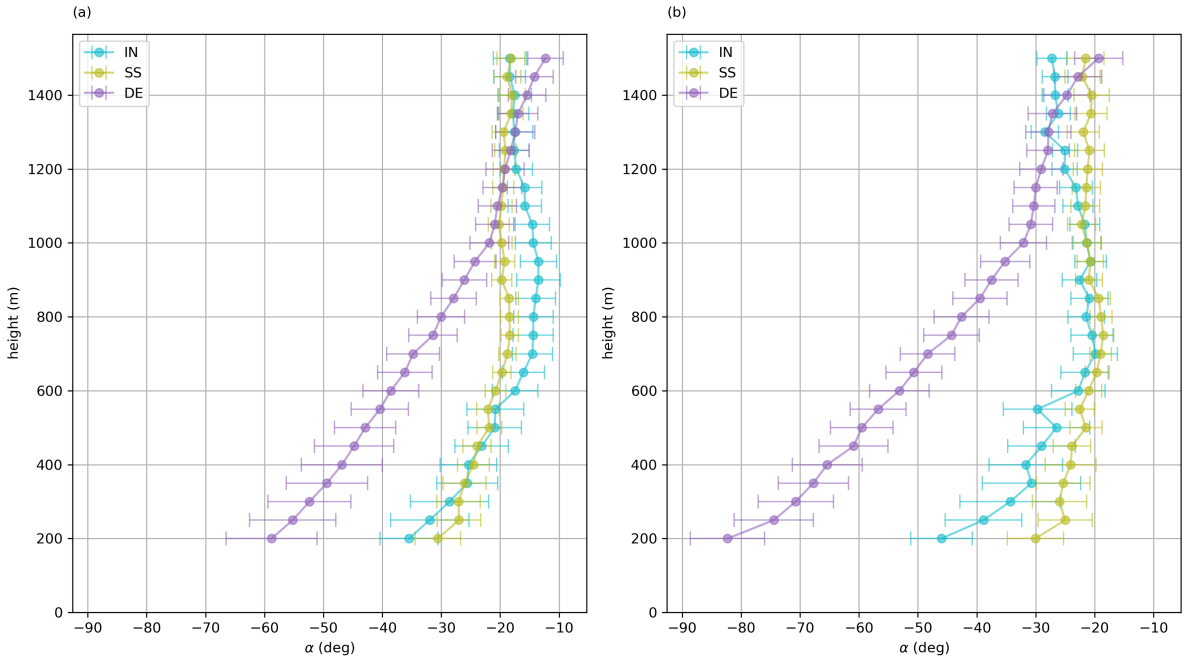


Figure 5.2: Boundary layer profile of inflow angle for intensifying (IN), steady-state (SS) and decaying (DE) TS averaged over (a) all samples and (b) samples in the front-left quadrant.

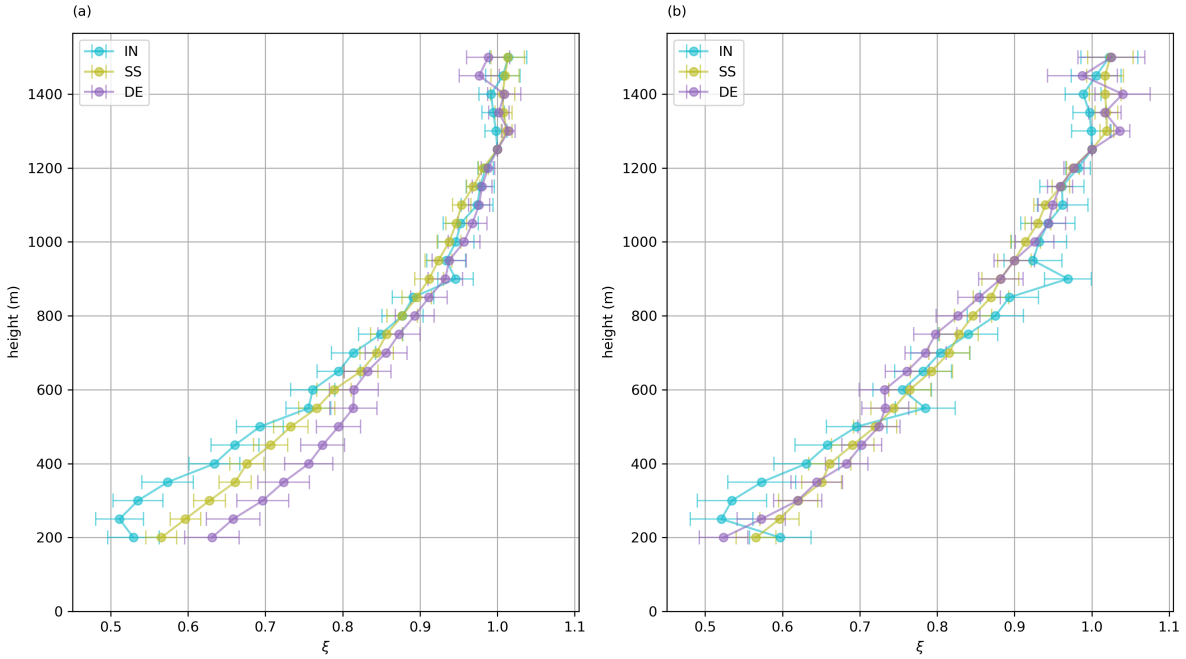


Figure 5.3: Same as Figure 5.2 but for reduction factor.

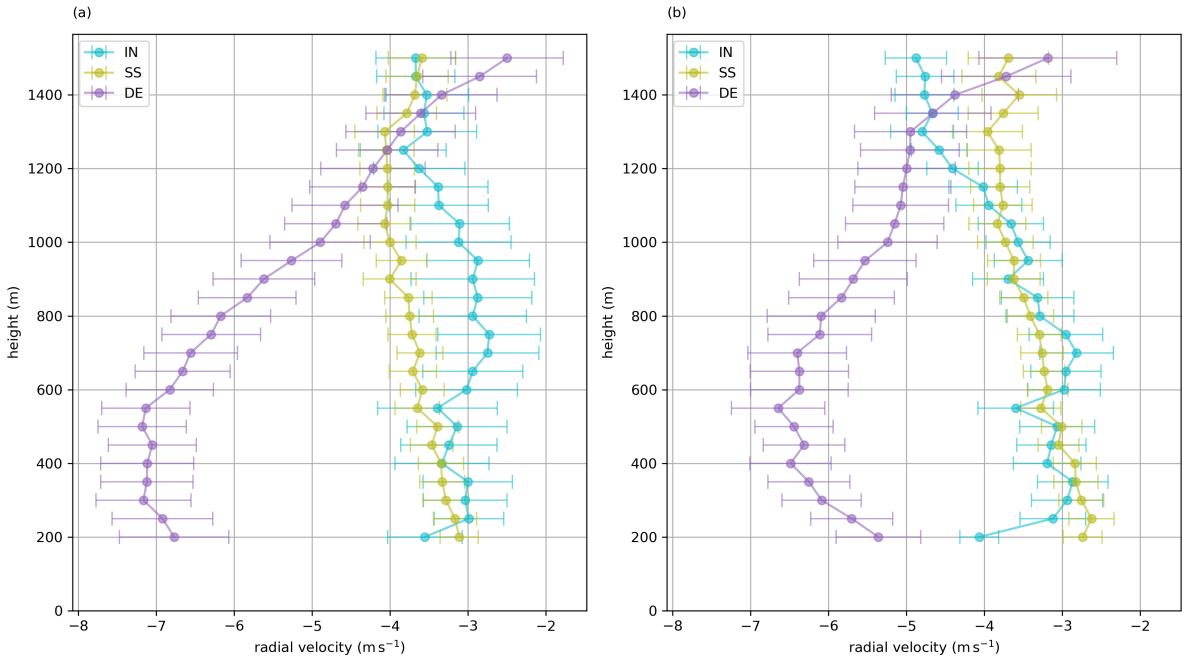


Figure 5.4: Same as Figure 5.2 but for radial velocity.

of recurve in the lower part of the boundary layer. In the middle to bottom of the boundary layer, the radial velocity of decaying TS is clearly larger than those of intensifying and steady-state TS. This means decaying TS has a stronger inflow layer than intensifying and steady-state TS.

Sorting the TS boundary layer profiles by the centre's distance to land produces results that resemble the above. This is robust across different threshold distances from 50 km to 140 km, where a threshold of 80 km (Figures B.2 to B.4) gives the closest match in behaviour between the close to (far from) land group and the decaying (intensifying and steady-state) group. However, this is neither surprising nor very helpful as for example with 80 km threshold, around 71.2% (93.6%) of the front-left quadrant profiles in the close to (far from) land group are also from decaying (intensifying and steady-state) TS. A comparison between Figures 5.1 and B.1 also illustrates this point.

Looking at decaying TS and TC, it is clear that all basic features in the boundary layer profiles are common across the two, differing only in size and scale. The inflow angle of decaying TC is smaller than that of decaying TS throughout the boundary layer (Figure B.5). Descending through the boundary layer, the reduction in wind speed in decaying TC is weaker than in decaying TS (Figure B.6). Finally, decaying TC has stronger inflow than decaying TS throughout the boundary layer with a peak in radial velocity at a lower altitude

(Figure B.7).

5.4 Discussion

12 storms making landfall near Hong Kong are analysed, from which a difference in the boundary layer inflow angle profiles between decaying and non-decaying (intensifying and steady-state) TS is observed. Starting with similar values at the top of the boundary layer, the inflow angle of decaying TS increases steadily as altitude descends through the boundary layer while that of non-decaying TS only starts to increase pass 600 m, reaching only about half that of decaying TS at 200 m. Meanwhile, the reduction factors of decaying and non-decaying TS are similar throughout the boundary layer. These combine to give a stronger inflow layer in decaying TS than in non-decaying TS. This result can be reproduced by separating the profiles based on the TS centre's distance to land, where the close to (far from) land group matches with the decaying (non-decaying) group. Comparing decaying TS and TC, all basic features in the boundary layer profiles are common across the two, differing only in size and scale.

Unlike Knupp et al. (2006) with landfalling TS Gabriel (2001), the presence of jets (large enhancement of wind speed over a thin layer in the middle of the boundary layer) is not observed in any of the composite TS boundary layer profiles here. The absence of jets from TC near Hong Kong based on HKO data has previously been reported by Tse et al. (2013). The decaying TC boundary layer radial velocity profile observed here (Figure B.7) appears to agree with Ren et al. (2019) that the inflow layer of a TC is well below 1500 m. It is also compatible with that observed by Knupp et al. (2000) from landfalling Hurricane Georges (1998) and with the simulation results by Hlywiak & Nolan (2022) and Kepert & Wang (2001).

Although Rogers et al. (2013) observed stronger near-surface inflow and deeper inflow layer in intensifying TCs compared to steady-state ones, citing larger depth scales for inertially less stable cyclones (Kepert 2001), such differences are not seen in the TS observations here. Furthermore, unlike Liao et al. (2019), there is no sign of outflow in the boundary layer of the decaying TS or TC here. The observations here show that intensifying and steady-state TS have similar inflow throughout the middle to bottom of the boundary layer while that of decaying TS is clearly stronger (Figure 5.4). Meanwhile, the individ-

ual boundary layer wind profiles of intensifying, steady-state and decaying TS, especially for the front-left quadrant, are taken from TS with similar V_{max} (Tables 5.1 to 5.3), hence largely similar inertial stability.

Sparks & Toumi (2022*b*) showed how surface pressure increases are driven by the net inflow into the column for a weakening storm. The pressure tendency depends on both the inflow and the size of the cyclone (Sparks & Toumi 2022*a*). Their framework does not invoke inertial stability and is consistent with the observations here. The difference in inflow strength between decaying and non-decaying TS is then hypothesised here to be due to the cyclone's differing proximity to land (Figure 5.1 (a) and Figure B.1 (a)) rather than their inertial stability.

Measurements of decaying cyclones are taken when their centres are considerably closer to or even over land. This is not the case for non-decaying cyclones. The boundary layer profiles are also compared based on the TS centre's distance to land and it is found that the behaviour of the close to (far from) land group matches with the decaying (non-decaying) group. However, given the large overlap of profiles across these 2 classifications, this cannot be considered a robust independent result.

The effect of inertial stability of the cyclone can be assessed by comparing the decaying TS (weaker) and TC (stronger) in this study. Decaying TC are inertially more stable due to their higher wind speeds. Nevertheless, they have similar but scaled boundary layer profiles compared to decaying TS. The way in which the boundary layer profiles, described by the reduction factor (Figure B.6) and radial velocity (Figure B.7), scale between the two appear to agree with Kepert (2001) that inertially less stable cyclones have larger depth scales. However, while the boundary layer profiles of decaying TS and TC are similar, non-decaying TS behave differently.

The stronger inflow in the middle to bottom of the boundary layer in the decaying TS here compared to non-decaying TS is driven by larger inflow angle throughout the boundary layer under similar wind reduction (normalised wind speed profile). It is then important to understand how enhanced surface friction due to land can modify the inflow angle without affecting the normalised wind speed profile. The eddy diffusivity, through its effect on the production of turbulence kinetic energy, plays a central role in governing the shape of the wind speed profile and the boundary layer height. Surface friction affects the atmosphere by causing mesoscopic turbulence and modifying the eddy diffusivity

near the surface. However, above this surface layer, atmospheric properties such as the shear and stability rather than surface roughness are dominant in determining the eddy diffusivity. In other words, the primary effect of surface friction on the atmosphere is in modulating its surface layer thickness. Grisogono (2011) showed that for a boundary layer with altitude-dependent eddy diffusivity, both the near-surface wind deflection angle and boundary layer height can depend on such parameters as the overall strength of the eddy diffusivity and the surface layer thickness. It was shown for the eddy diffusivity profile $K(z) = K_0 (z/h) \exp\left[-0.5 (z/h)^2\right]$ that when $K_0 > 1\,\mathrm{m^2\,s^{-1}}$, the near-surface wind deflection angle is sensitive to changes in both the surface layer thickness and K_0. However, the boundary layer height is only weakly sensitive to such changes. Changing the surface friction can lead to a different inflow angle while maintaining similar normalised wind speed profile shape in the boundary layer. Therefore, enhanced surface friction due to land is a plausible explanation for the observed differences in the boundary layer of decaying and non-decaying TS in this study.

Previous studies used data collected from fairly evenly spatially distributed dropsondes. The distance of the cyclone centre from land at measurement, the distance of measurement from the cyclone centre, and the azimuthal angle of measurement relative to cyclone translation direction can all be controlled to eliminate bias in sampling. In contrast, the use of a ground-based instrument at a fixed weather station in this study means that the 3 parameters just mentioned are not independent for the samples in the dataset here. The most significant drawbacks are that there is inevitable bias in sampling rate through the azimuthal angle of measurement relative to cyclone translation direction and that certain quadrants will have a markedly higher proportion of data taken post-landfall. As a result, simply taking the sample mean is inappropriate due to azimuthal asymmetry in translating tropical cyclones. Attempt has been made to overcome this bias by analysing the 4 quadrants relative to cyclone translation direction separately. However, there is enough data to study the front-left quadrant only. The deficiency in data hindered attempts to study the azimuthal asymmetry in TS near landfall and the effect of the flow being onshore or offshore. Finally, the lack of non-decaying (decaying) TS close to (far from) land in the HKO wind profiler dataset means that results from sorting the TSs by their centre's distance to land should not be taken as an independent piece of evidence to support the hypothesis raised.

5.5 Conclusions

The boundary layer wind profiles measured within $4R_{\max}$ from 12 tropical cyclones making landfall near Hong Kong are analysed. These profiles are acquired with a wind profiler between 2010 and 2019 at the Sha Lo Wan weather station in Hong Kong. These measurements reveal that the inflow angles of intensifying and steady-state TS are similar to each other throughout the boundary layer but smaller than those of decaying TS, especially in the middle to bottom of the boundary layer. Converging towards the top of the boundary layer, the inflow angle of decaying TS is roughly double that of intensifying and steady-state TS at an altitude of 200 m. On the other hand, the wind speed reduces through the boundary layer in a similar way in all 3 cases. The stronger inflow in decaying TS compared to intensifying and steady-state TS is then mainly driven by the larger inflow angle of decaying TS throughout the boundary layer. Inertial stability has been put forward to explain the differences in boundary layer profile between stronger cyclones that are intensifying and in steady-state (e.g. Rogers et al. 2013). Here, differences are observed between decaying and non-decaying TS instead and it is argued that the effects of enhanced friction by land due to proximity in the decaying TS is the likely main driver of the observed differences. In general, the flow being onshore or offshore could also have an effect. This however could not be and is not assessed here limited by the HKO wind profiler dataset. The discussed effects should also apply to other coastal locations.

Chapter 6

The Re-intensification of Tropical Cyclones Re-entering Ocean from Land

6.1 Introduction

After making landfall, a tropical cyclone is cut off from the supply of heat and moisture from the ocean and experiences enhanced surface friction, generally leading to its weakening. However, if such a perturbed system then re-enters ocean (hereafter seafall), it can re-intensify. In fact, tropical cyclones in the West Pacific and North Atlantic basins often pass over land and re-intensify over the ocean before making another landfall. For example, Typhoon Mangkut (2018) passed through Luzon Island before making landfall at Jianmen, Guangdong; Hurricane Ian (2022) passed through Cuba and then Florida before making its third and final landfall at Georgetown, South Carolina. They both re-intensified upon making seafall. However, the seafall of tropical cyclones has not been thoroughly explored by existing works in the literature. This chapter addresses the question what is the baseline structural evolution tropical cyclones perturbed by landfall go through as they make seafall.

The only mechanism proposed for the seafall re-intensification of tropical cyclones is that of land-induced eyewall replacement cycle as part of the following case studies by full simulation: Typhoon Zeb (1998) passing through the Philippines (Wu et al. 2009, 2003), Typhoon Megi (2010) passing through the Philippines (Wang & Wang 2014, 2021), and Typhoon Fanapi (2010) passing through Taiwan (Yang et al. 2018). However, as the set of statistics on seafalling tropical cyclones produced by Chou et al. (2011) points out, only 57% of the tropical cyclones passing through the Philippines experience land-induced eyewall

replacement cycle, and the figure is even lower for those passing through Taiwan. This chapter is devoted to the study of the baseline structural evolution of seafalling tropical cyclones by a series of idealised WRF-AWR simulations. A clearer understanding of the details of the baseline structural evolution experienced by seafalling tropical cyclones as they re-intensify is a first step to allow for better predictions of their behaviour leading up to their next landfall and could aid operational forecast and risk mitigation efforts.

6.2 Methods

The idealised simulation experiment for the study of seafalling tropical cyclones begins with a "development" run with the entire simulation domain over an ocean surface with a fixed SST of 29 °C. An initial bogus vortex (see Section 2.11) with $V_{0,\max} = 18\,\mathrm{m\,s^{-1}}$ and $R_{0,\max} = 100\,\mathrm{km}$ is allowed to develop and mature over 15 days. This provides tropical cyclones of varying initial states for landfall runs. Then, a set of 10 landfall runs are created from the development run every 24 hours beginning 6 days into the development run by switching the ocean surface in the entire domain into land making use of WRF-AWR's restart function. The land surface type of "croplands" in the modified IGBP MODIS 20-category land-use dateset (Friedl et al. 2010) is chosen in these landfall runs, each lasting 24 hours. Finally, a set of 26 seafall runs are obtained from the set of landfall runs by similarly switching the land in the entire domain back into ocean surface with a fixed SST of 29 °C. The 26 seafall runs each lasts for 72 hours and are initiated when the maximum near-surface wind speed of the tropical cyclones decays to around 34, 44, 54 and 64 kt. All simulations are performed at a latitude of 22.3° N. With idealised simulations, the layer of complexity originating from the full details of the geometry and topography of the land and seafloor is avoided, making it easier for the assessment of the baseline structural evolution experienced by seafalling tropical cyclones and to focus on the effects due to the intrinsic properties of the tropical cyclone.

To study the seafall re-intensification behaviour of the simulated tropical cyclones, the following characteristic quantities of the tropical cyclones in both the development and seafall runs are determined hourly: the maximum near-surface wind speed ($V_{\max}$), the minimum surface pressure ($p_{\min}$), the magnitude of the angular momentum per unit mass at the point of maximum near-surface wind speed with respect to the tropical cyclone cen-

tre ($l_{\max}$), the radius of maximum near-surface wind speed ($R_{\max}$), the radius of maximum azimuthally averaged near-surface wind speed ($\tilde{R}_{\max}$), the inflow angle at the point of maximum near-surface wind speed ($\alpha_{\max}$), the gradient wind speed at the point of maximum near-surface wind speed (V_{gwb}) and the inertial stability (I). The location of $p_{\min}$ is considered to be the tropical cyclone centre, V_{gwb} is estimated by

$$V_{\text{gwb}} = -\frac{f R_{\max}}{2} + \sqrt{\frac{f^2 R_{\max}^2}{4} + \frac{R_{\max} |\nabla_{\text{h}} p|}{\rho}}, \tag{6.1}$$

where $|\nabla_{\text{h}} p|$ is the magnitude of the horizontal gradient of pressure obtained using central difference and ρ the air density, all evaluated at the point of $V_{\max}$, and I is estimated by (Wang et al. 2021)

$$I = f + \frac{2V_{\max}}{R_{\max}}. \tag{6.2}$$

Furthermore, the rate of change of $V_{\max}$ ($\dot{V}_{\max}$) is determined by linearly regressing an appropriate section of the time series of $V_{\max}$.

To study the post-seafall structural evolution of the simulated tropical cyclones, the change in $\tilde{R}_{\max}$ with respect to its value at seafall ($\Delta\tilde{R}_{\max}$), and the azimuthal averages of the near-surface wind speed (V_{surf}), the logarithmic radar reflectivity (Ladwig 2017) at an altitude of 5 km ($L_Z^{5\,\text{km}}$) and the vertical profile of the vertical velocity (w) are computed at various times after seafall.

6.3 Results

Figure 6.1 illustrates the development, landfall and seafall runs of the experiment, showing the time-evolution of $V_{\max}$, $p_{\min}$, $R_{\max}$ and $\tilde{R}_{\max}$. The initial intensification of the bogus vortex in the development run lasts around 3 days as can been seen from both Figure 6.1 (a) and Figure 6.1 (b). Meanwhile, its inner-core size as indicated by both $R_{\max}$ and $\tilde{R}_{\max}$ (Figure 6.1 (c, d)) first contracts from the initial assigned value of 100 km to around 20 km over the course of around 1 day following which it slowly expands to and settles at around 100 km, with a jump in the 9-th day of the development run. The maximum $V_{\max}$ achieved under the environment of the experiment setup is around 125 kt, while the lowest $p_{\min}$ reached is around 925 hPa. Across the 26 seafall runs, the time the tropical cyclones spend over land ranges from 2 to 22 hours. Both landfall and seafall cause a 2-stage evolution

of V_{max}. After landfall (seafall), V_{max} first drops (increases) abruptly within the first hour, and then continues to decay (intensify) much more gradually. In contrast, the evolution of p_{min} after landfall and, especially, seafall is much smoother. Both the intensity and inner-core size of the tropical cyclones in the seafall runs appear to relax to the values in the development run at the corresponding simulation time.

The time-evolution of V_{max}, p_{min}, V_{max}/V_{gwb} and inflow angle at the point of V_{max} (α_{max}) in the seafall runs are shown in Figure 6.2 (a, d, g, h). In addition, the change in V_{max} and p_{min} with respect to their values at (Figure 6.2 (b, e)) and 1 hour after (Figure 6.2 (c, f)) seafall are also shown. Figure 6.2 (g) shows that in the development run, V_{max} matches almost exactly V_{gwb}. By the time of seafall, V_{max} has dropped to around $0.6V_{gwb}$, irrespective of the time the tropical cyclone had spent over land, but recovers to V_{gwb} within 1 hour of seafall. Correspondingly, α_{max} at seafall is larger than that in the development run and decreases afterwards towards the development run value as shown in Figure 6.2 (h). Note that the quick alignment of V_{max} with V_{gwb} within 1 hour of seafall is due to an abrupt leap of V_{max} as shown in Figure 6.2 (a–c); while p_{min} has hardly changed during this process as Figure 6.2 (d–f) illustrate.

Figure 6.3 compares the time-evolution of V_{max}, p_{min} and specific angular momentum at the point of V_{max} (l_{max}) in the seafall runs of tropical cyclones of different intensities, determined by V_{max} 1 hour after seafall, to those in the initial intensification in the development run from a similar V_{max}. The time-series of V_{max} after subtracting the values at hour 1 are also shown. The intensification rate of V_{max} beyond the first hour after seafall could not exceed that in the development run from a similar intensity. Again, p_{min} does not change appreciably during the first hour despite an abrupt leap in V_{max}. It does however decrease gradually as V_{max} continues to grow at a reduced rate beyond the first hour. Notice that l_{max} is always higher in the seafall runs compared to the development run. Also, it tends to increase as the tropical cyclone re-intensifies post-seafall but is essentially conserved in the initial intensification over the ocean. To quantify how much the initial ocean intensification out runs the seafall re-intensification, the signed areas bounded above by the development run curve and below by the averaged seafall run curve between hour 1 and hour 72 in Figure 6.3 (b, f, j, n, r) are computed and shown in Table 6.1. It suggests that tropical cyclones that are stronger 1 hour after seafall intensify at a rate that is slower than that in the initial ocean intensification from a similar intensity by a greater extent.

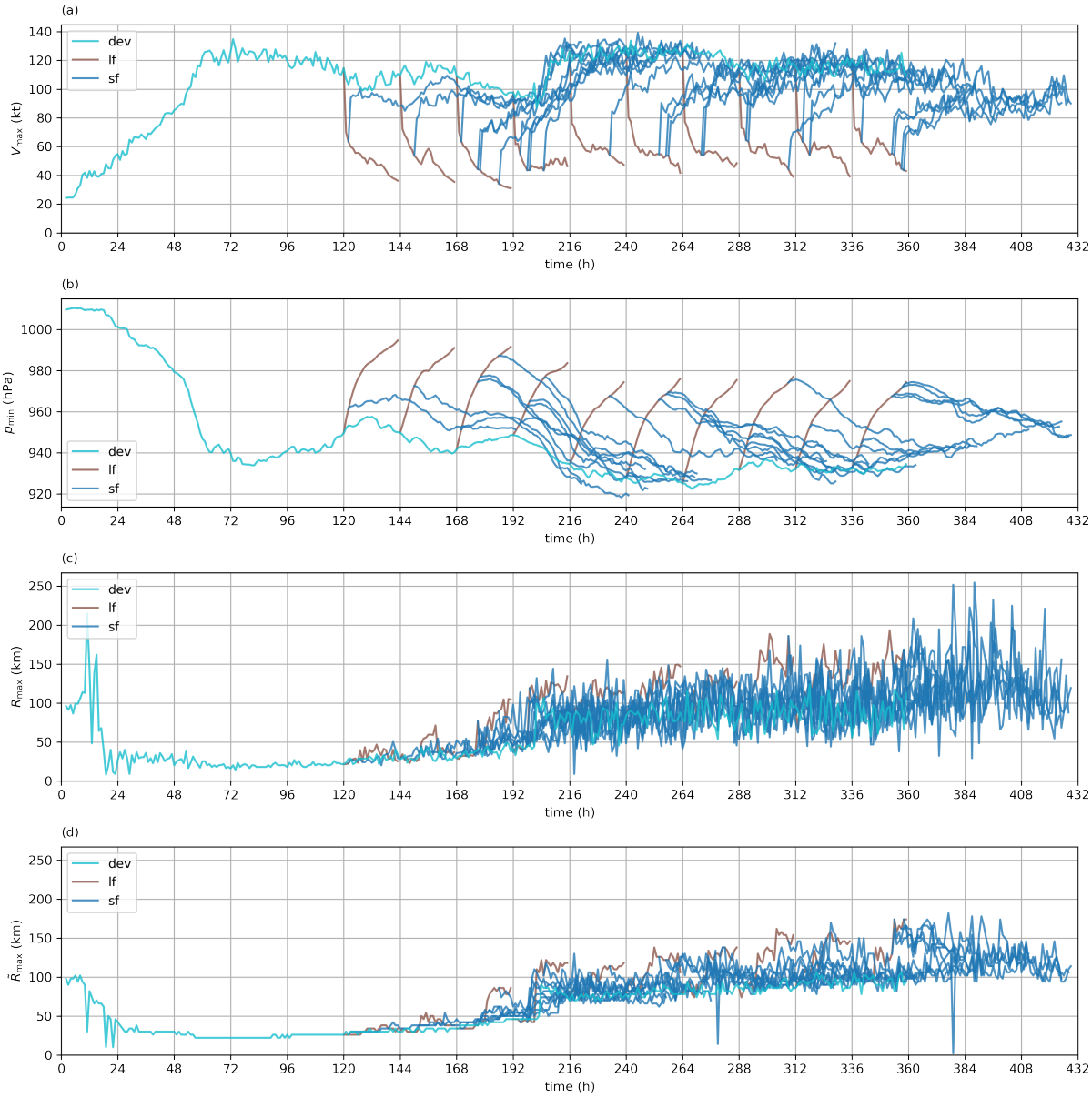


Figure 6.1: Overview of the development (dev, cyan), landfall (lf, brown) and seafall (sf, blue) runs of the experiment, showing the time-evolutions of (a) $V_{\max}$, (b) $p_{\min}$, (c) $R_{\max}$ and (d) $\tilde{R}_{\max}$.

$V_{\max}(1\,\mathrm{h})$ (kt)	62.4	72.7	83.0	93.2	103.5
area (kt h)	4770	5912	6808	7517	8046

Table 6.1: Areas bounded above by the development run curve and below by the averaged seafall run curve between hour 1 and hour 72 in Figure 6.3 (b, f, j, n, r).

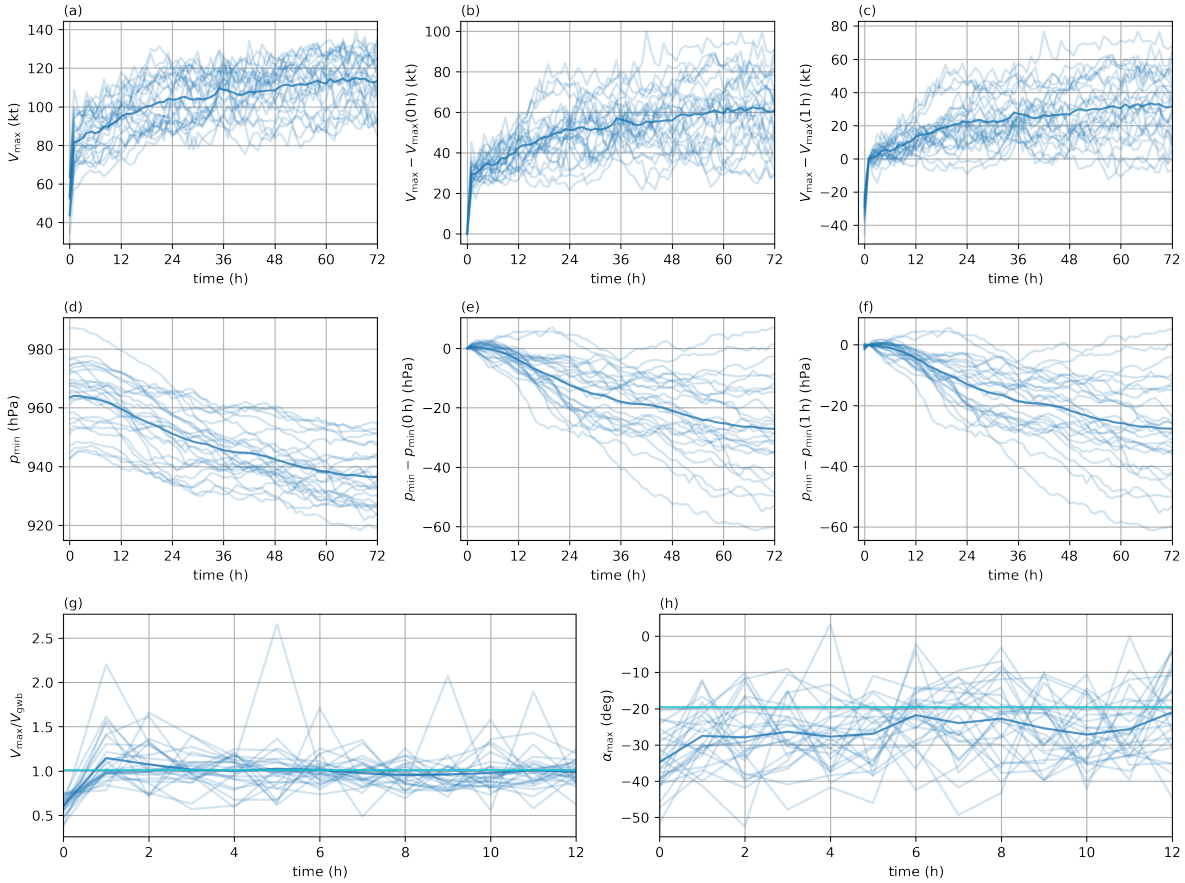


Figure 6.2: Post-seafall time-evolution of certain tropical cyclone properties in the individual seafall runs (light blue) and average (solid blue) — (a) $V_{\max}$; (b) difference in $V_{\max}$ with respect to the value at seafall; (c) same as (b) but with respect to the value 1 hour after seafall; (d–f) same as (a–c) but for $p_{\min}$; (g) $V_{\max}/V_{\mathrm{gwb}}$; (h) $\alpha_{\max}$. (a–h) Cyan line indicates the average value between the 5-th and 8-th days in the development run as a representative value.

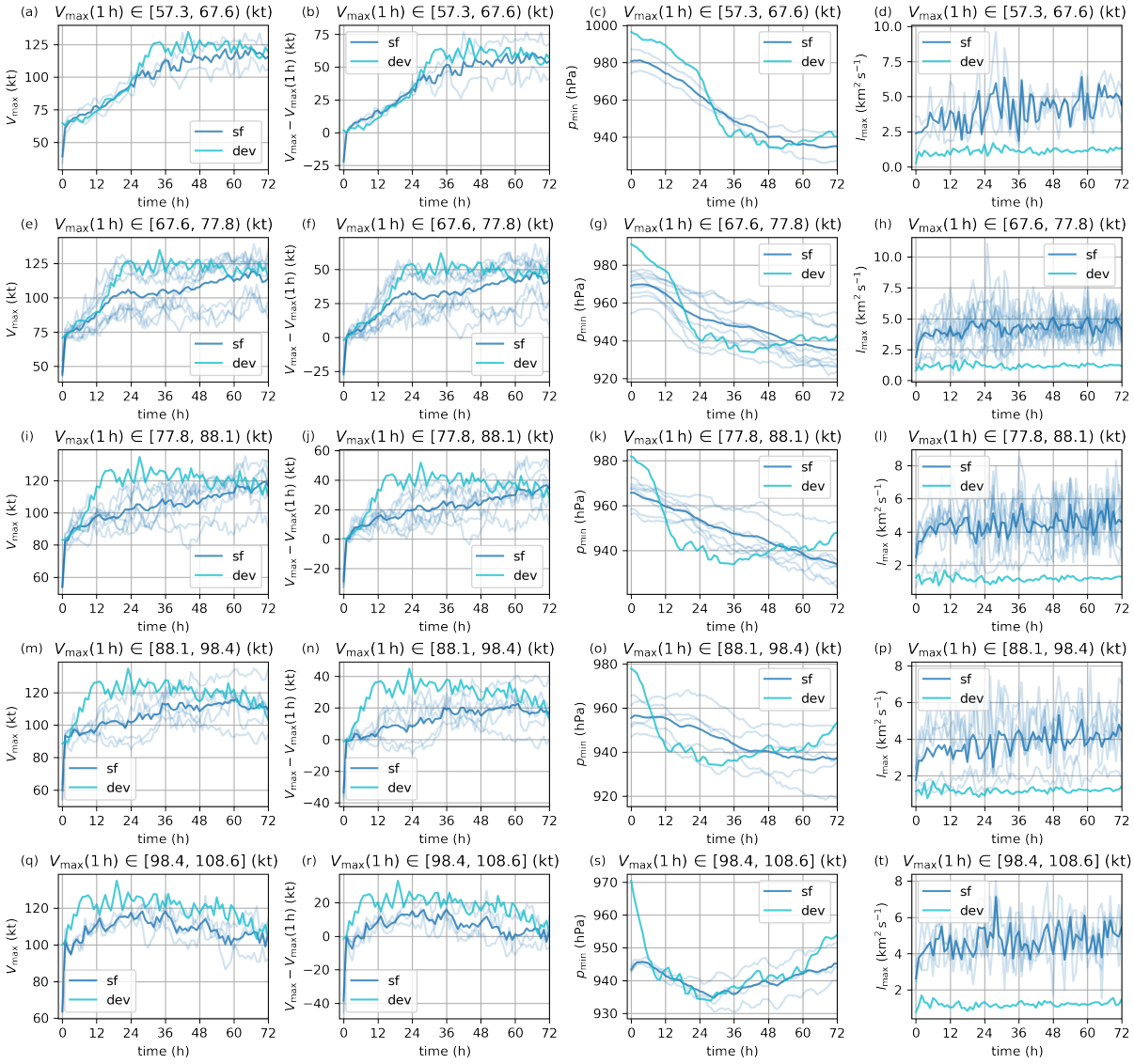


Figure 6.3: Post-seafall time-evolution of certain tropical cyclone properties in the individual seafall runs (light blue) and average (solid blue) for groups classed by V_{max} 1 hour after seafall. (a) V_{max} for cyclones with 57.3 kt $\leq V_{max} <$ 67.6 kt 1 hour after seafall. (b) Same as (a) but showing the difference of V_{max} with respect to the value 1 hour after seafall. (c) Same as (a) but showing p_{min}. (d) Same as (a) but showing l_{max}. (e–h), (i–l), (m–p), (q–t) Same as (a–d) except for cyclones with 67.6 kt $\leq V_{max} <$ 77.8 kt, 77.8 kt $\leq V_{max} <$ 88.1 kt, 88.1 kt $\leq V_{max} <$ 98.4 kt, 98.4 kt $\leq V_{max} <$ 108.6 kt 1 hour after seafall. (a–t) Cyan line shows the time-evolution of the corresponding tropical cyclone property over a window in the initial intensification stage of the development run such that the V_{max} at hour 1 corresponds to the seafall group average value.

Figures 6.4 and 6.5 show scatter plots of the post-seafall $\dot{V}_{\max}$ against $V_{\max}$, $p_{\min}$, $R_{\max}$, $\tilde{R}_{\max}$ and inertial stability (I) at seafall and $V_{\max}$ 1 hour after seafall. In Figure 6.4 (Figure 6.5), the post-seafall $\dot{V}_{\max}$ is determined by linearly regressing the time series of $V_{\max}$ within the 6-hour (24-hour) window beginning 1 hour after seafall. With the 6-hour window, the post-seafall $\dot{V}_{\max}$ does not correlate significantly ($p > 0.05$) with any of the considered tropical cyclone properties around seafall. However, with the 24-hour window, although the post-seafall $\dot{V}_{\max}$ still does not correlate significantly with $p_{\min}$, $R_{\max}$, $\tilde{R}_{\max}$ and I at seafall, it does, albeit weakly, with $V_{\max}$ at ($r^2 = 0.26$, $p < 0.01$) and 1 hour after ($r^2 = 0.25$, $p < 0.01$) seafall, with slopes of -0.05 ± 0.03 ($\mathrm{kt\,h^{-1}\,kt^{-1}}$) and -0.03 ± 0.02 ($\mathrm{kt\,h^{-1}\,kt^{-1}}$) respectively.

Figure 6.6 (a–m) are scatter plots of $\Delta\tilde{R}_{\max}$ at certain times after seafall against $\tilde{R}_{\max}$ at seafall. Figure 6.6 (n) shows the sensitivity of $\Delta\tilde{R}_{\max}$ against $\tilde{R}_{\max}$ at seafall as a function of time from seafall. The sensitivities are obtained by linear regressions, whose squared Pearson correlation coefficient (r^2) and p-value are shown in Figure 6.6 (o). $\Delta\tilde{R}_{\max}$ is always significantly ($p < 0.05$) anti-correlated with $\tilde{R}_{\max}$ at seafall. The sensitivity grows with time after seafall while the correlation becomes stronger, with r^2 saturating at around 0.8 36 hours after seafall. Based on the fitted lines in Figure 6.6 (a–m), tropical cyclones with $\tilde{R}_{\max}$ of around 100 km at seafall do not change in inner-core size, while smaller (larger) ones expend (contract). In the long run, $\tilde{R}_{\max}$ tends to around 100 km (see also Figure 6.1 (d)). From Figure 6.6 (a–m), a group of tropical cyclones with $\tilde{R}_{\max} < 75$ km at seafall that expands in inner-core size can be clearly identified from the rest and will be the focus of this study.

Figures 6.7 to 6.9 show the composite post-seafall time-evolution of the azimuthal average radial profile of V_{surf}, logarithmic radar reflectivity at 5 km altitude ($L_Z^{5\,\mathrm{km}}$) and w of the expanding group. The peak in the radial profile of V_{surf} (Figure 6.7) grows from around 50 kt to around 100 kt as it moves away form the cyclone centre from around 35 km to around 80 km over the course of 3 days. The width of the peak remains fairly constant throughout the process. The peak in the radial profile of $L_Z^{5\,\mathrm{km}}$ (Figure 6.8) also moves away from the centre from around 60 km to around 120 km over the course of 3 days. Unlike V_{surf} however, the width of the $L_Z^{5\,\mathrm{km}}$ peak shrinks throughout the process. The radial profile of w (Figure 6.9) shows an overall strengthening of updraft over the course of 3 days. The region of strong updraft shifts outwards, shrinks and increases in tilt throughout the process.

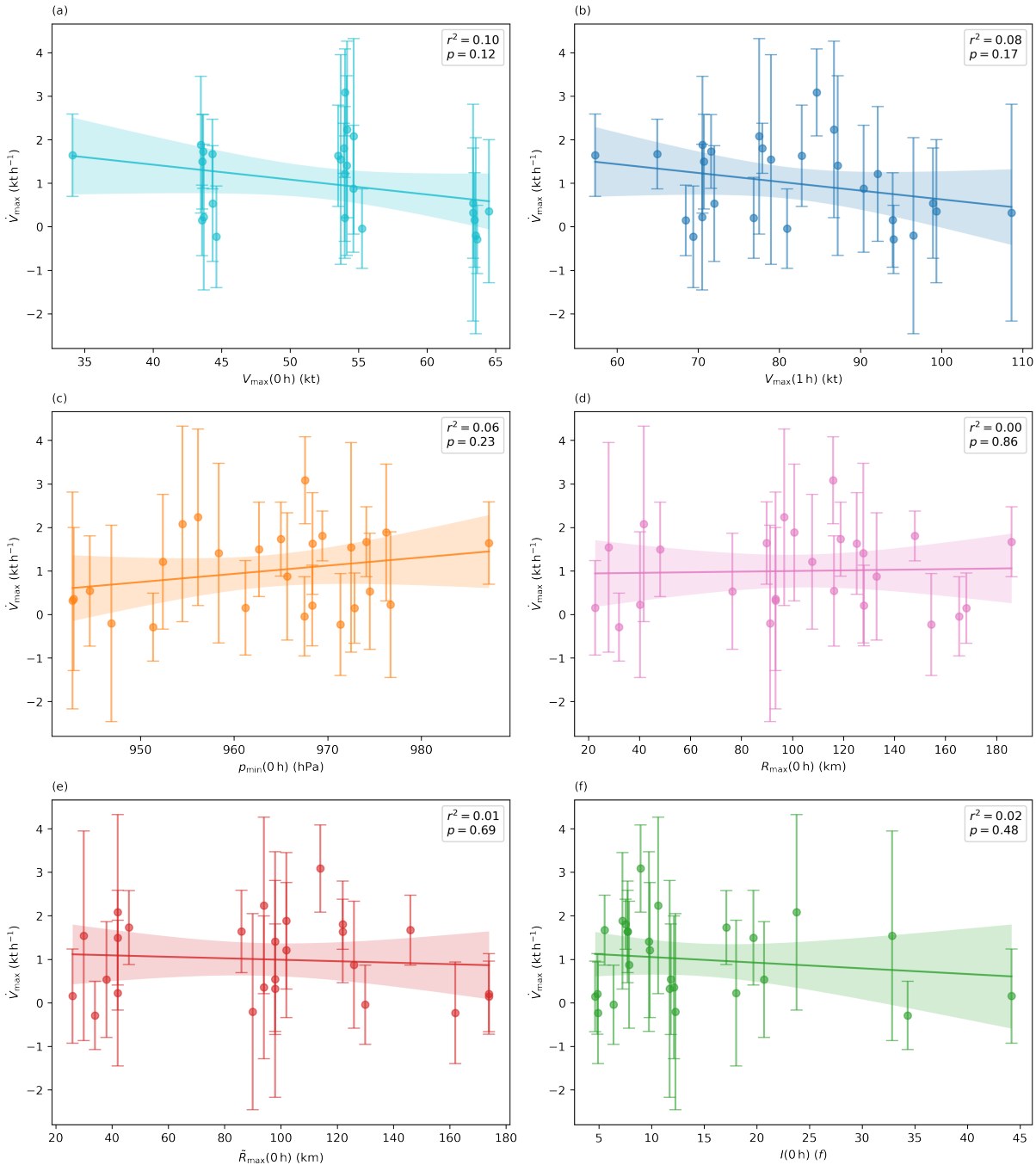


Figure 6.4: Scatter plots with linear least square fit of post-seafall $\dot{V}_{\text{max}}$ against (a) V_{max}, (c) p_{min}, (d) R_{max}, (e) $\tilde{R}_{\text{max}}$ and (f) I at seafall and (b) V_{max} 1 hour after seafall, where the post-seafall $\dot{V}_{\text{max}}$ are obtained by linearly regressing the time series of V_{max} within the 6-hour window beginning 1 hour after seafall. Shaded regions indicate 95% confidence interval.

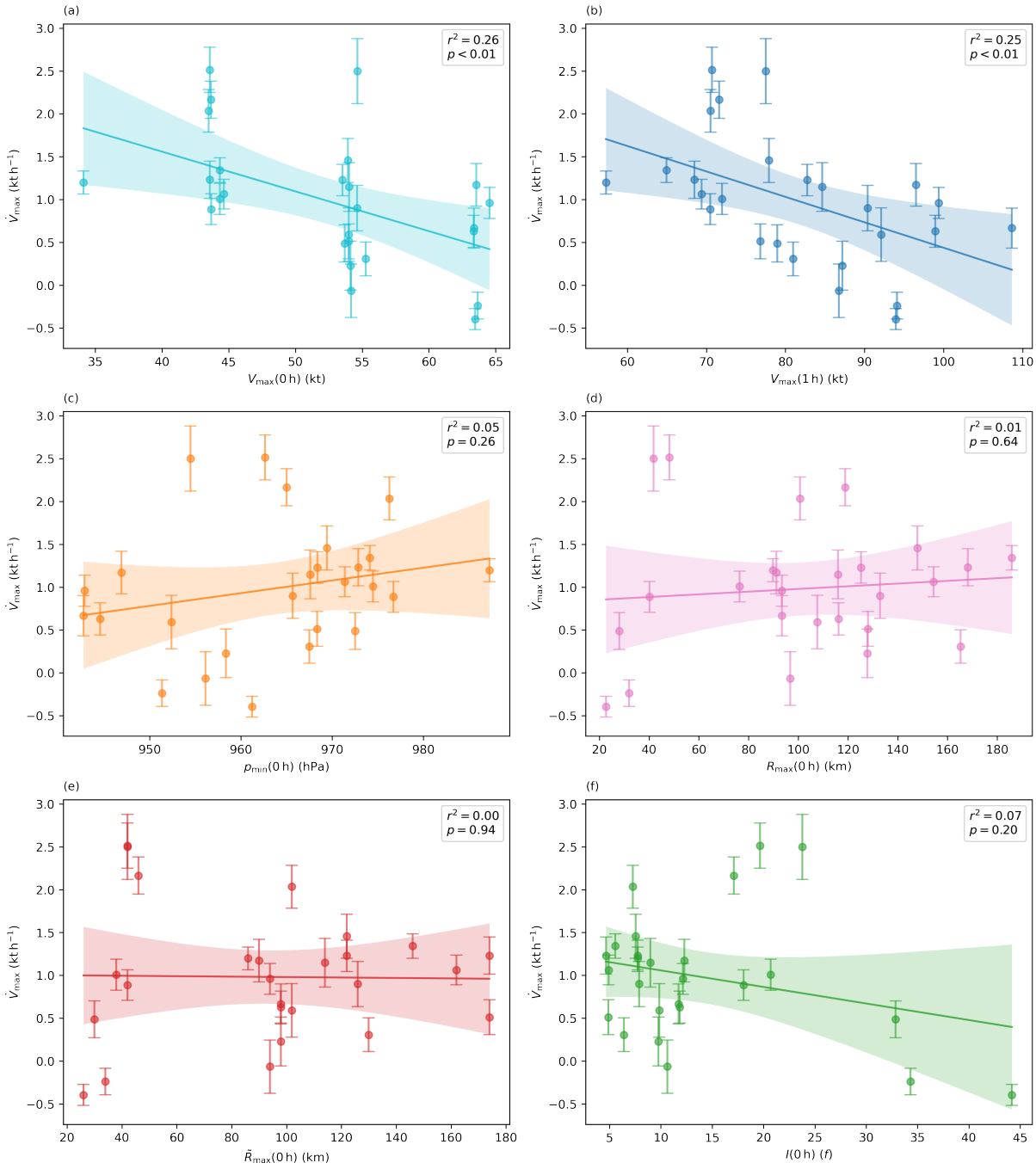


Figure 6.5: Same as Figure 6.4 but with post-seafall $\dot{V}_{\text{max}}$ obtained by linearly regressing the time series of V_{max} within the 24-hour window beginning 1 hour after seafall.

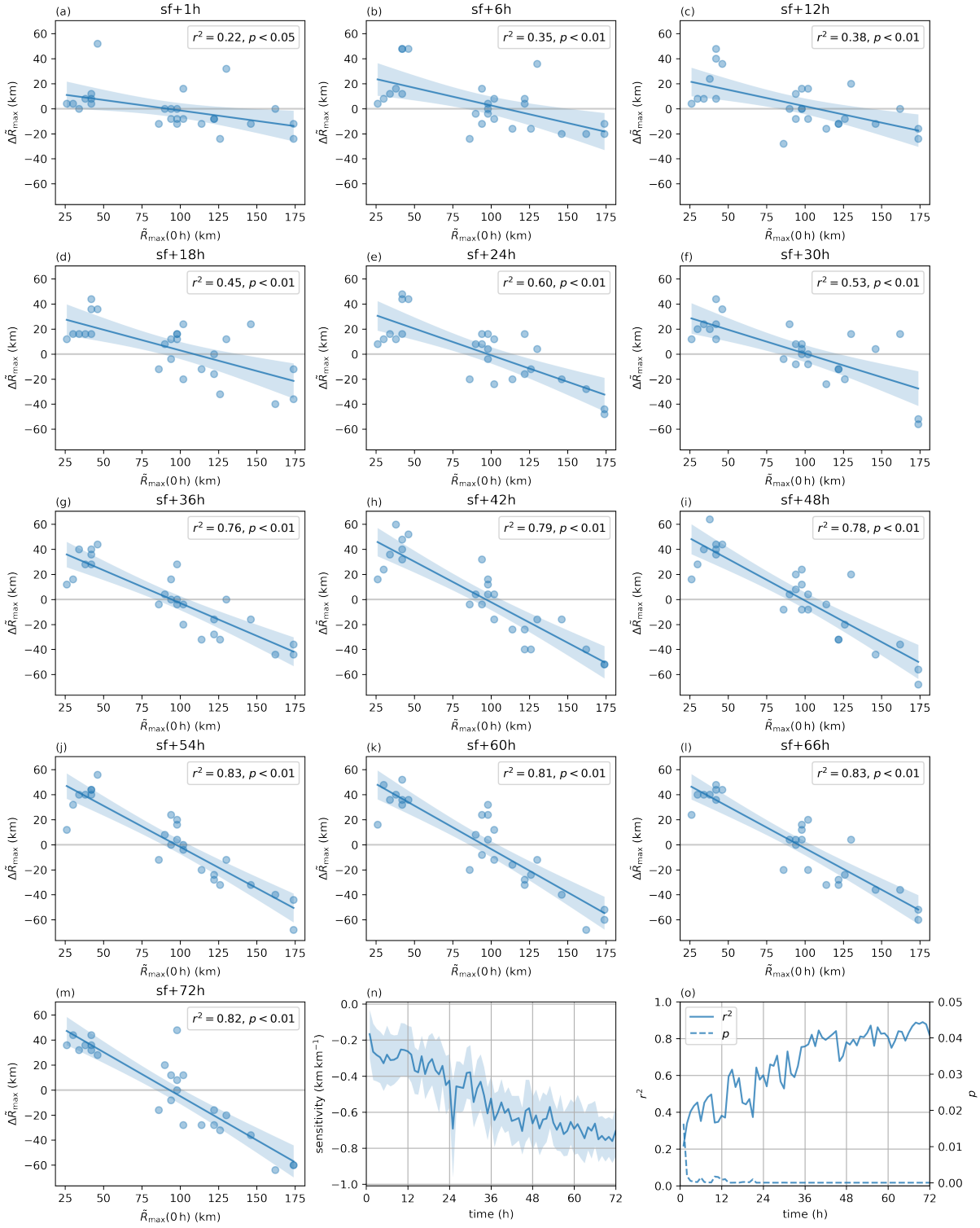


Figure 6.6: (a–m) Scatter plots with linear least square fit of $\Delta\tilde{R}_{max}$ against $\tilde{R}_{max}$ at seafall at various time after seafall. (n) Sensitivity of $\Delta\tilde{R}_{max}$ against $\tilde{R}_{max}$ at seafall as a function of time after seafall. (o) Squared correlation coefficient and p-value between $\Delta\tilde{R}_{max}$ and $\tilde{R}_{max}$ at seafall as a function of time after seafall. (a–n) Shaded regions indicate 95% confidence interval.

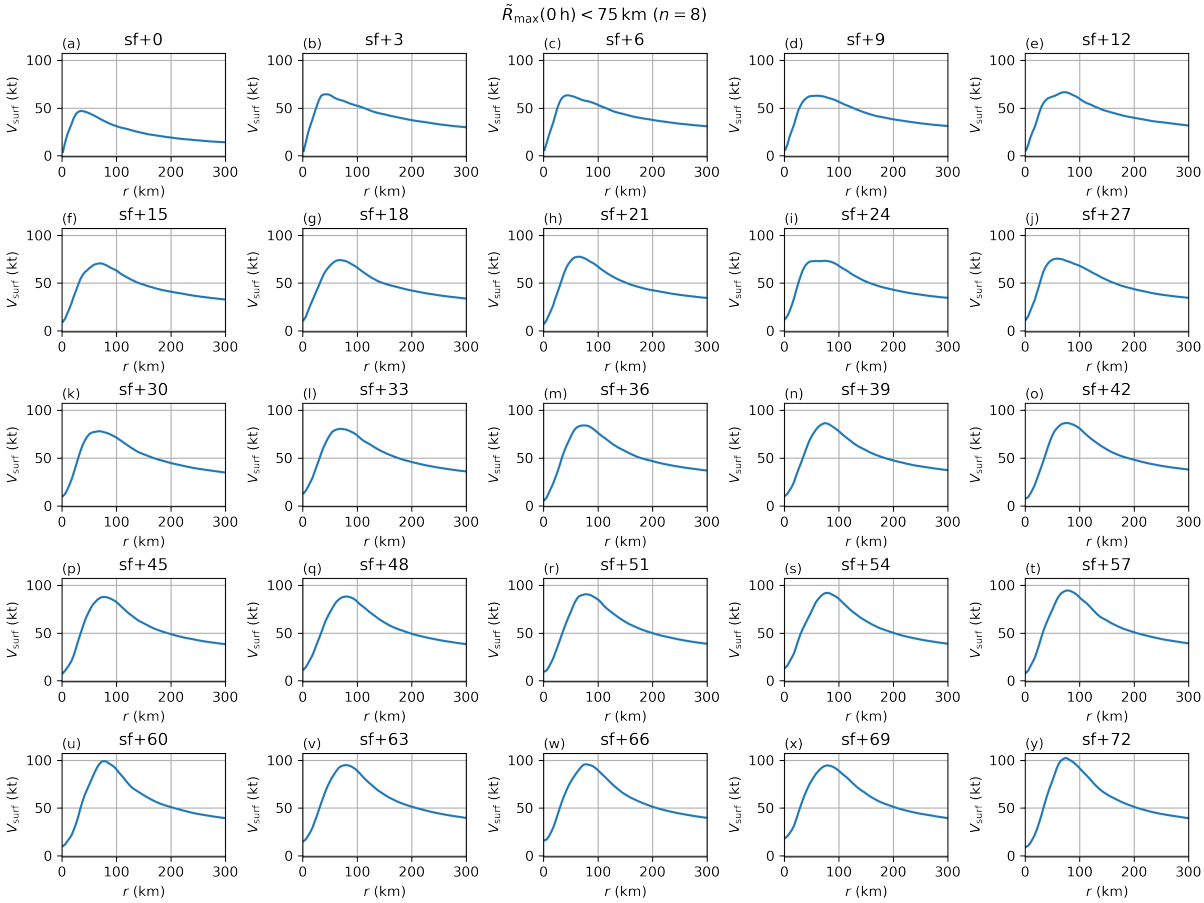


Figure 6.7: Composite azimuthal average radial profile of V_{surf} in seafall runs with $\tilde{R}_{\max} < 75\,\mathrm{km}$ at seafall every 3 hours since seafall.

To summarise, after seafall, the tropical cyclone grows in inner-core size while its eyewall becomes thinner and more tilted over the course of 3 days.

6.4 Discussion

Numerical simulations produced by the WRF-AWR model are used to investigate the post-seafall behaviour of tropical cyclones. The experiment begins with a development run where a bogus vortex is allowed to develop into a tropical cyclone over an ocean surface with constant SST. The entire surface is then switched to land and then back to ocean at various times, producing landfall and seafall runs with tropical cyclones of varying initial states at seafall. In the development run, $V_{\max}$ matches almost exactly V_{gwb} (Figure 6.2 (g)), indicative of gradient wind balance, although not exactly as the corresponding inflow angle ($\alpha_{\max}$) does not vanish (Figure 6.2 (h)). By the time of seafall, $V_{\max}$ has dropped to around $0.6V_{\mathrm{gwb}}$ irrespective of the time the tropical cyclone had spent over land, a clear indication

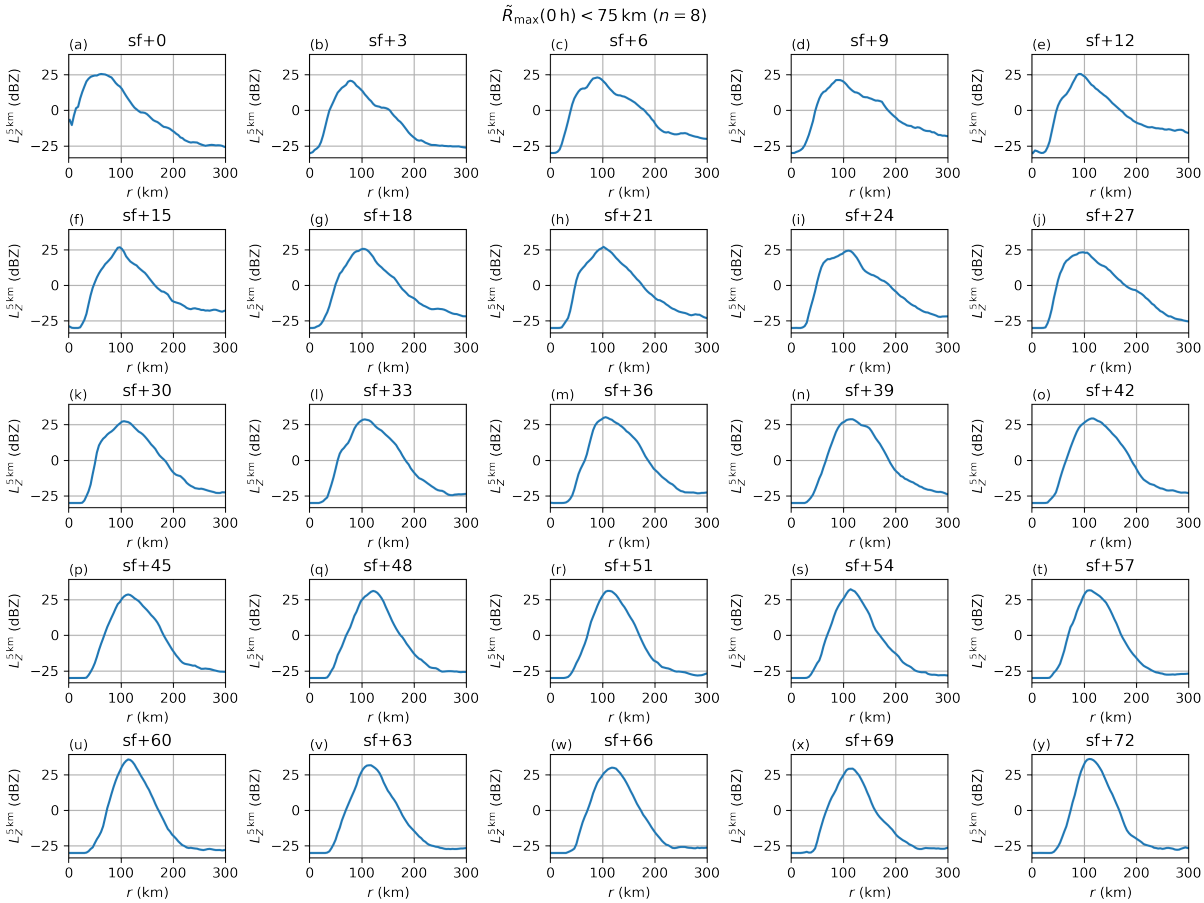


Figure 6.8: Same as Figure 6.7 but for $L_Z^{5\,\mathrm{km}}$.

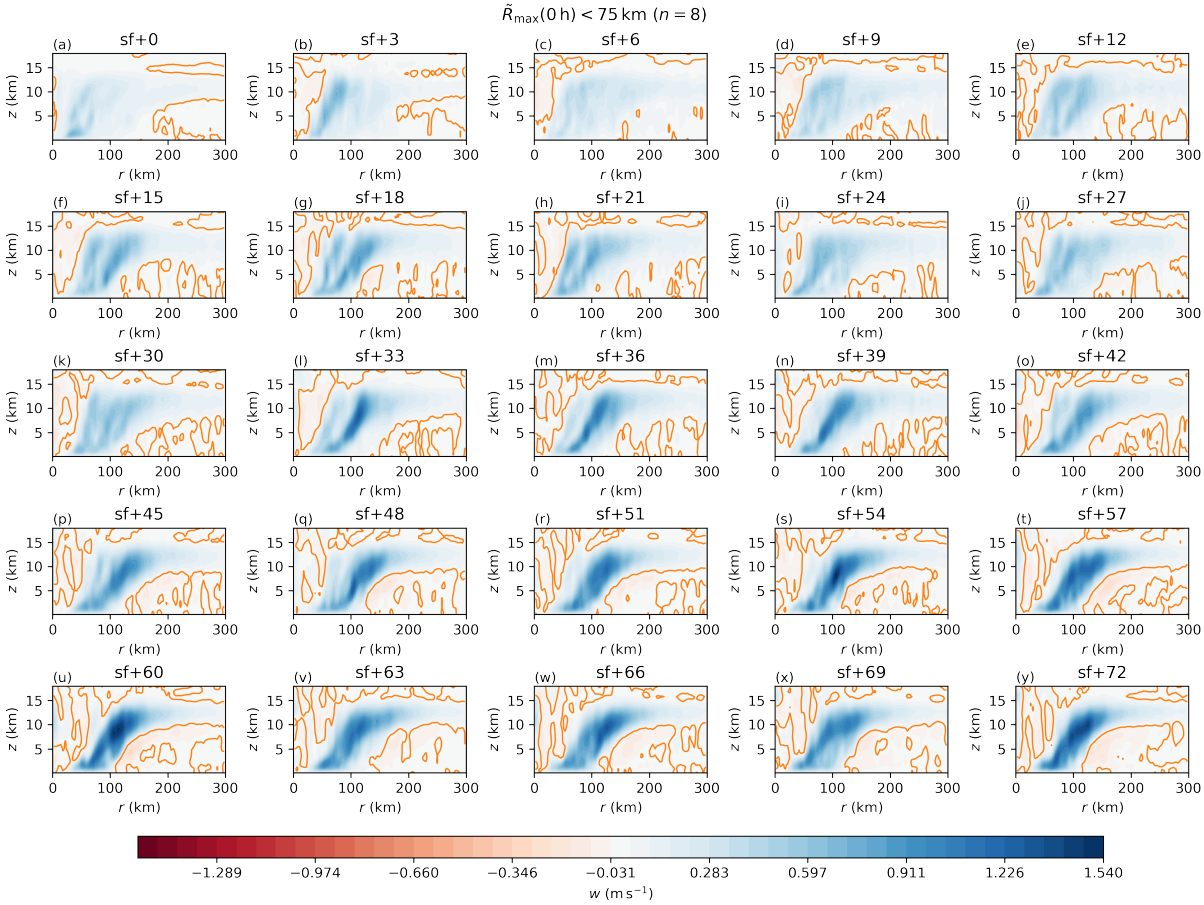


Figure 6.9: Same as Figure 6.7 but for w.

that gradient wind balance is disrupted as one would expect due to higher surface friction over land compared to ocean. Restoration of V_{max} back to the level of V_{gwb} is achieved within 1 hour of seafall (Figure 6.2 (g)) and is accompanied by a decrease in α_{max} (Figure 6.2 (h), indicative of a restoration of gradient wind balance to the extent in the development run.

Seafalling tropical cyclones go through a 2-stage structural evolution as they re-intensify. Immediately after seafall, V_{max} experiences an abrupt leap within 1 hour (Figure 6.2 (a–c)), aligning itself with V_{gwb} (Figure 6.2 (g)); while p_{min} has hardly changed during this process (Figure 6.2 (h)). This suggests that the initial response to seafall from V_{max} is predominately purely dynamical, due to a sharp decrease in surface friction. Afterwards, V_{max} continues to increase at a reduced rate compared to the initial intensification over ocean, accompanied by a gradual decrease in p_{min}. This subsequent, much more gradual, increase in V_{max} could then be understood as an intensification process driven thermodynamically as latent heat and moisture supply to the tropical cyclone from a warm and moist ocean surface resumes. Furthermore, tropical cyclones with higher V_{max} 1 hour after seafall appear to re-intensify at a rate that is slower than the corresponding initial ocean intensification rate by a greater extent. This reduction in intensification rate for seafalling tropical cyclones compared to initial ocean intensification from a similar intensity could be due to their higher l_{max} (Figure 6.3 (d, h, l, p, t)), meaning that they are larger in size and more difficult to spin up.

The intensification rate of V_{max} in the second stage of the post-seafall re-intensification process is bounded from above by the rate in the development run starting at a similar V_{max} (Figure 6.3) and is weakly anti-correlated with V_{max} at and 1 hour after seafall but not with p_{min}, R_{max}, $\tilde{R}_{\mathrm{max}}$ and I at seafall (Figure 6.5). On the other hand, $\Delta\tilde{R}_{\mathrm{max}}$ shows significant anti-correlation with R_{max} at seafall which becomes stronger with increasing sensitivity with time (Figure 6.6). Tropical cyclones with $\tilde{R}_{\mathrm{max}}$ of around 100 km at seafall maintain their inner-core size while smaller (larger) ones tend to expand (contract) to that same size. Given that the $\tilde{R}_{\mathrm{max}}$ in the development run also tends to around 100 km in the long run (Figure 6.1 (d)), it is plausible that this behaviour has to do with the way the simulation is set up or even an artefact of the WRF-ARW model. The Sawyer-Eliassen Equation describes the streamfunction of the secondary flow in the radius-height plane for vortices evolving slowly, remaining near gradient and in hydrostatic balance. By examining its solution in height coordinates, Pendergrass & Willoughby (2009) argued that contraction or expansion of the tropical cyclone eye can be controlled by the tilt of the radius of maximum wind

speed and heat source. Whether the relaxation of $\tilde{R}_{\text{max}}$ towards 100 km seen in the seafall runs is a mere artefact of the model used or has a deeper physical origin warrens further investigations. Nonetheless, there is clearly a group of tropical cyclones with $\tilde{R}_{\text{max}} < 75$ km at seafall that expand in inner-core size afterwards as they re-intensify (Figure 6.6).

In contexts such as the initial intensification of tropical cyclones from genesis (Shapiro & Willoughby 1982, Schubert & Hack 1983, Vigh & Schubert 2009) or the eyewall replacement cycle (Zhou & Wang 2011, Sitkowski et al. 2012), the intensification of tropical cyclones is usually accompanied by a decrease in inner-core size. However, it does not appear to be a rare occurrence for seafalling tropical cyclones to intensify with expanding inner-core size based on the experiment here (Figure 6.7). In the meantime, the eyewall becomes thinner and more tilted as the cyclone re-intensifies post-seafall (Figure 6.9). On the other hand, numerical simulation of Severe Tropical Cyclone Debbie (2017) by Deng & Ritchie (2023) shows an eyewall that contracts while maintaining thickness and becoming less tilted during its offshore intensification from genesis.

6.5 Conclusions

The post-seafall structural evolution of tropical cyclones is investigated using idealised WRF-AWR simulations by switching the entire surface from ocean to land and then back to ocean at various model times. V_{max} matches V_{gwb} closely before landfall and becomes subgradient afterwards. Upon seafall, the tropical cyclones undergo a 2-stage re-intensification process. Within 1 hour of seafall, V_{max} leaps abruptly to catch up with V_{gwb} without noticeable change in p_{min}. Subsequently, V_{max} continues to increase at a much slower rate and is accompanied by a corresponding decrease in p_{min}. The first stage is predominately a purely dynamical response of the tropical cyclone to a sharp decrease in surface friction; while the second stage is a thermodynamically driven intensification process due to a resumption of latent heat and moisture supply from a warm and moist ocean surface. In the second stage, the rate of increase of V_{max} shows a weak dependence on V_{max} 1 hour after seafall but never exceeds that in the initial spin-up from a comparable intensity, probably due to their higher l_{max} making them more reluctant to spin up. On the other hand, $\Delta\tilde{R}_{\text{max}}$ is significantly anti-correlated with $\tilde{R}_{\text{max}}$ at seafall. In particular, tropical cyclones with $\tilde{R}_{\text{max}} < 75$ km at seafall tend to expand in inner-core size accompanied by a thinning of eyewall and increase

in tilt as they re-intensify, differing from the behaviour commonly associated with tropical cyclone intensification from genesis or in eyewall replacement cycle.

Chapter 7

Conclusions

7.1 Summary

As laid downed in Section 1.5 and stated in more details in the beginning of Chapters 3 to 6, this thesis is devoted to addressing the following questions:

1. whether the presence of tropical cyclones in the North Atlantic contributes to the occurrence of fires in the Amazon, and if so what is the physical mechanism behind;
2. whether long-range prediction of ENSO-driven atmospheric responses can be achieved by tracing the maturing of the surface ENSO state back to any preceding signals in the subsurface temperature or heat content anomalies in the Pacific basin;
3. what is the dominating factor affecting the boundary layer wind profile of relatively weak tropical cyclones near landfall; and
4. what is the baseline structural evolution tropical cyclones perturbed by landfall go through as they make seafall?

In Chapter 3, significant interannual correlation between North Atlantic tropical cyclones and South Amazon fires, which have seasonal cycles that are in phase, is found to be driven exclusively by Caribbean tropical cyclones. A cross-equatorial thermally direct Hadley-type circulation response driven by off-equatorial heating partly caused by Caribbean tropical cyclones is hypothesised to provide a direct physical pathway allowing the storms to enable fires in the Amazon. Anomalous precipitation over the Caribbean, irrespective of cause, leads to anomalous ascent by releasing latent heating there. This

sets up an anomalous Hadley-type circulation with a descending branch over the Amazon, promoting atmospheric conditions favourable to fire there. Since much of the precipitation anomalies in the Caribbean can be traced back to the existence of tropical cyclones in the region, they can be considered an enabler of fires in the Amazon.

In Chapter 4, a new SubNiño4 index is created as the anomaly of subsurface potential temperature beneath the Niño4 region between the depths of 100 m and 300 m based on Sparks & Toumi (2020) and is shown to be capable of predicting ENSO-driven regional precipitation anomalies throughout the tropics and fires in Continental and Maritime Southeast Asia. It captures the evolution of subsurface heat content in the Pacific basin between the El Niño and La Niña phases of the ENSO cycle and can therefore serve as a long-range indicator of surface ENSO signals. It is superior to the commonly used western Pacific warm water volume anomaly in that it produces similar but temporally more stable lagged correlations with surface ENSO signals, becoming significant at around the same lead-time but sustained further into shorter lead-times. The SubNiño4 index can further serve as a long-range indicator of atmospheric phenomena driven by ENSO, in particular regional precipitation anomalies throughout the tropics and fires in Continental and Maritime Southeast Asia. In many cases, the SubNiño4 index outperforms the western Pacific warm water volume anomaly by producing higher lagged correlations with the target atmospheric phenomenon over a larger time window. The domain of definition of the SubNiño4 index may identify more precisely the critical point of action of the subsurface branch of established ENSO dynamics.

In Chapter 5, for tropical storms making landfall near Hong Kong, it is observed that the boundary layer profiles of intensifying and steady-state systems are similar to each other and are distinct from those of decaying ones. The decaying tropical storms have a stronger inflow layer than non-decaying ones resulting from a greater inflow angle under similar fractional reduction in wind speed throughout the boundary layer. Compositing the boundary layer profiles of the tropical storms based on their centre's distance to land gives similar results, with correspondence between the close to (far from) land group and the decaying (non-decaying) group. On the other hand, the boundary layer profiles of decaying tropical storms and decaying tropical cyclones at higher intensity are similar, being scaled version of each other. The reason for the boundary layer of decaying tropical storms to differ from that of non-decaying ones is thus attributed to enhanced surface friction due

to proximity to land, rather than intensity change or differing inertial stability, which have been shown in previous studies focused on stronger systems with intensity above tropical storm level (e.g. Rogers et al. 2013) to also affect the boundary layer profile of tropical cyclones.

In Chapter 6, the post-seafall structural evolution of tropical cyclones is investigated using a series of idealised WRF-AWR simulations. It is revealed that seafall leads to a 2-stage re-intensification process of the tropical cyclone. In the first stage, the maximum near-surface wind speed jumps from being subgradient to match with the gradient wind speed within 1 hour of seafall without noticeable change in minimum surface pressure. In the second stage, the maximum near-surface wind speed continues to increase at a much slower rate with a corresponding decrease in minimum surface pressure. The first stage is predominately purely dynamically driven as the tropical cyclone responds to a sharp decrease in surface friction; while the second stage is driven thermodynamically owing to a resumption of latent heat and moisture supply from a warm and moist ocean surface. It is found that the intensification rate of the seafalling tropical cyclone in the second stage cannot exceed that in the initial spin-up from a comparable intensity and is weakly dependent on the maximum near-surface wind speed 1 hour after seafall. The reason for seafalling tropical cyclones to re-intensify at a reduced rate compared to the initial intensification over the ocean from a similar intensity could be due to their higher specific angular momentum at the point of maximum near-sufrace wind speed, suggesting that they are larger in size and more difficult to spin up. It is also found that tropical cyclones with radius of maximum wind below 75 km at seafall tend to expand in inner-core size with a thinning eyewall which increases in tilt as they re-intensify post-seafall. Such behaviours are in contrast to orthodox tropical cyclone intensification from genesis or during eyewall replacement cycle. Whether the expansion in inner-core size is an artefact of the model used or may be traced back to a deeper physical origin associated with, for example, the tilt of the radius of maximum wind speed and heat source requires further investigations.

7.2 Future work

In Chapter 3, the existence of an anomalous cross-equatorial thermally direct Hadley-type cell accompanying the existence of tropical cyclones in the Caribbean is supported by com-

posite observational evidences based on the mid-level vertical velocity. The causal relationship from the hurricanes to the anomalous cell is hypothesised based on the fact that hurricanes enhance precipitation and hence latent heating locally and on existing modelling studies with either direct forcing or precipitation as heat source leading to circulations similar to what is observed. A more complete understanding of the structure and extent of the anomalous cell in question could be achieved by directly analysing the full 3-dimensional wind field and latent heat flux from say EAR5 data. On the other hand, modelling studies, either real or ideal, using tropical cyclone and induced precipitation thereof as heat source could more conclusively establish the causal relationship from hurricane to anomalous circulation cell as well as reveal the physics and mechanisms involved in greater details. Furthermore, it is worth investigating whether fires in southern Southeast Asia and North Australia can also be enabled by the existence of tropical cyclones in the North Pacific through a similar mechanism to what is hypothesised here with Amazon fires.

In Chapter 4, the potential utility of Pacific subsurface potential temperature as a long-range predictor for ENSO-driven atmospheric responses throughout the tropics has been demonstrated through a stable lagged correlation between the SubNiño4 index and precipitations throughout the tropics and fires in both the Maritime and Continental Southeast Asia. To broaden the impact of the study, the SubNiño4 index could be further tested for its capability to produce long-range lagged correlations with other ENSO-driven atmospheric responses such as Amazon fire, North Atlantic tropical cyclones and surface temperature throughout the tropics. The study suggests that there is room for tuning the region over which the subsurface temperature signal is taken to optimise the correlation with the atmospheric responses of interest, which could be pursued using techniques in machine learning and artificial intelligence. To put the results of this study into practice, one could seek to improve existing long-range statistical prediction models for ENSO-driven atmospheric responses by including Pacific subsurface potential temperature signal, possibly in the form of some optimised version of the SubNiño4 index. To further investigate the mechanism behind the origin of the Pacific subsurface temperature anomalies preceding the maturing of the surface ENSO state, study of ocean reanalysis data could be helpful.

Chapter 5 provides observational evidences based on tropical cyclones making landfall near Hong Kong that landfall leads to an enhanced and thickened inflow layer in weak tropical cyclones throughout the middle to bottom of the boundary layer. It could be of in-

terest to verify this finding using observations from other coastal locations prone to tropical cyclone landfall, for example Miami and Okinawa. Model studies can be used to further verify the effects of landfall on weak tropical cyclones compared to that on stronger ones and to separate the effects due to enhanced friction and orography. From a more fundamental perspective, the Ekman layer treatment assumes a 3-way balance among Coriolis force, pressure gradient force and friction within the boundary layer and geostrophic balance above. The non-incorporation of the centripetal force obviously means that it would not be sensible to treat the tropical cyclone boundary layer strictly as an Ekman layer. However, by considering a 4-way balance among Coriolis force, centripetal force, pressure gradient force and friction within the boundary layer and gradient wind balance beyond in analogy to the Ekman layer treatment, it may be possible to achieve a more complete theoretical understanding of the tropical cyclone boundary layer.

Chapter 6 lays a foundation for the study of the structural evolution of tropical cyclones re-entering ocean from land, i.e. seafall, through the use of idealised model. The only mechanism for the re-intensification of seafalling tropical cyclones studied in the literature is that of land-induced eyewall replacement cycle through the case studies by full simulation of Typhoon Zeb (1998) (Wu et al. 2009, 2003), Typhoon Megi (2010) (Wang & Wang 2014, 2021) and Typhoon Fanapi (2010) (Yang et al. 2018), with the first 2 passing through the Philippines and the last through Taiwan. All 3 seafalling typhoons experienced eyewall reorganisation and contraction, consistent with the observational study by Chou et al. (2011). However, none of these studies explored the seafall re-intensification rate. Furthermore, as pointed out by Chou et al. (2011), tropical cyclones passing through Taiwan seldom go through such land-induced eyewall replacement cycle and even those passing through the Philippines do so only 57% of the time. 4 questions naturally arise:

1. how do those seafalling tropical cyclones not undergoing land-induced eyewall replacement cycle re-intensify;

2. are properties such as size, intensity and tilt of the tropical cyclone at landfall and its time spent over land important in determining whether it will go through land-induced eyewall replacement cycle during seafall;

3. how do these parameters affect the re-intensification rate of seafalling tropical cyclones undergoing land-induced eyewall replacement cycle; and

4. how, if in any way, does tropical cyclone behaviour and structural evolution in land-induced eyewall replacement cycle during seafall differ from orthodox eyewall replacement cycle over ocean?

Other than land-induced eyewall replacement cycle, 2 other mechanisms that may provide alternative pathways for the seafall re-intensification of tropical cyclones could be explored — that through the reconnection of a decoupled mid-level vortex and that with a cold core.

Sparks & Toumi (2022*b*) showed through a set of idealised simulations that as a tropical cyclone spins down over land without latent convective heating, the boundary layer decouples from the vortex above. While the surface winds decay quickly, a mid-level vortex persists aloft. As the tropical cyclone makes seafall, latent convective heating is resumed, which based on the argument by Sparks & Toumi (2022*b*) should re-establish the connection between the boundary layer and the mid-level vortex, in turn allowing the tropical cyclone to quickly re-intensify.

Li & Chakraborty (2021) provided a new thermodynamic perspective to the post-landfall evolution of tropical cyclones as opposed to the common understanding of a kinematic spin-down. They showed with a set of idealised simulation experiments that a cold core is born in the lower troposphere, beneath and eating into the original warm core of the tropical cyclone post-landfall without it going through extratropical transition. They argued that the birth of a cold core in landfalling tropical cyclones should be a universal feature because as landfall progresses, the specific humidity and temperature of air reaching the base of the upflow of the tropical cyclone through its inflow decrease, raising the lifting condensation level and the level of free convection thus causing a cold core to come into existence from the bottom. In this case, as a tropical cyclone makes seafall, the thermodynamic interactions between its low-level cold core and the warm sea surface beneath could play a role in the re-intensification of the tropical cyclone.

Bibliography

Adler, R. F., Sapiano, M. R. P., Huffman, G. J., Wang, J.-J., Gu, G., Bolvin, D., Chiu, L., Schneider, U., Becker, A., Nelkin, E., Xie, P., Ferraro, R. & Shin, D.-B. (2018), 'The Global Precipitation Climatology Project (GPCP) Monthly analysis (New Version 2.3) and a review of 2017 global precipitation', *Atmosphere* **9**(4), 138.

Adler, R., Wang, J.-J., Sapiano, M., Huffman, G., Chiu, L., Xie, P.-P., Ferraro, R., Schneider, U., Becker, A., Bolvin, D., Nelkin, E., Gu, G. & NOAA CDR Program (2016), 'Global Precipitation Climatology Project (GPCP) Climate Data Record (CDR), Version 2.3 (Monthly)', Research Data Archive at the National Center for Atmospheric Research, Computational and Information Systems Laboratory, DOI: 10.5065/MM6J-9282.

Alencar, A., Asner, G. P., Knapp, D. & Zarin, D. (2011), 'Temporal variability of forest fires in eastern Amazonia', *Ecological Applications* **21**(7), 2397–2412.

Andreoli, R. V. & Kayano, M. T. (2006), 'Tropical Pacific and South Atlantic effects on rainfall variability over Northeast Brazil', *International Journal of Climatology* **26**(13), 1895–1912.

Aragão, L. E. O. C., Anderson, L. O., Fonseca, M. G., Rosan, T. M., Vedovato, L. B., Wagner, F. H., Silva, C. V. J., Silva Junior, C. H. L., Arai, E., Aguiar, A. P., Barlow, J., Berenguer, E., Deeter, M. N., Domingues, L. G., Gatti, L., Gloor, M., Malhi, Y., Marengo, J. A., Miller, J. B., Phillips, O. L. & Saatchi, S. (2018), '21st century drought-related fires counteract the decline of Amazon deforestation carbon emissions', *Nature Communications* **9**(1), 536.

As-Syakur, A. R., Osawa, T., Miura, F., Nuarsa, I. W., Ekayanti, N. W., Dharma, I. G. B. S., Adnyana, I. W. S., Arthana, I. W. & Tanaka, T. (2016), 'Maritime Continent rainfall variability during the TRMM era: the role of monsoon, topography and El Niño Modoki', *Dynamics of Atmospheres and Oceans* **75**, 58–77.

Ballester, J., Bordoni, S., Petrova, D. & Rodó, X. (2016), 'Heat advection processes leading to El Niño events as depicted by an ensemble of ocean assimilation products', *Journal of Geophysical Research: Oceans* **121**(6), 3710–3729.

Barlow, J., Berenguer, E., Carmenta, R. & França, F. (2020), 'Clarifying Amazonia's burning crisis', *Global Change Biology* **26**(2), 319–321.

Barnston, A. G., Tippett, M. K., L'Heureux, M. L., Li, S. & DeWitt, D. G. (2012), 'Skill of real-time seasonal ENSO model predictions during 2002–11: is our capability increasing?', *Bulletin of the American Meteorological Society* **93**(5), 631–651.

Battisti, D. S. & Hirst, A. C. (1989), 'Interannual variability in a tropical atmosphere-ocean model: influence of the basic state, ocean geometry and nonlinearity', *Journal of the Atmospheric Sciences* **46**(12), 1687–1712.

Berenguer, E., Carvalho, N., Anderson, L. O., Aragão, L. E. O. C., França, F. & Barlow, J. (2021), 'Improving the spatial-temporal analysis of Amazonian fires', *Global Change Biology* **27**(3), 469–471.

Bister, M. & Emanuel, K. A. (2002), 'Low frequency variability of tropical cyclone potential intensity 1. Interannual to irtterdecadal variability', *Journal of Geophysical Research: Atmospheres* **107**(D24), 4801.

Bjerknes, J. (1966), 'A possible response of the atmospheric Hadley circulation to equatorial anomalies of ocean temperature', *Tellus A: Dynamic Meteorology and Oceanography* **18**(4), 820–829.

Bjerknes, J. (1969), 'Atmospheric teleconnections from the equatorial Pacific', *Monthly Weather Review* **97**(3), 163–172.

Bowman, D. M. J. S., Balch, J. K., Artaxo, P., Bond, W. J., Carlson, J. M., Cochrane, M. A., D'Antonio, C. M., DeFries, R. S., Doyle, J. C., Harrison, S. P., Johnston, F. H., Keeley, J. E., Krawchuk, M. A., Kull, C. A., Marston, J. B., Moritz, M. A., Prentice, I. C., Roos, C. I., Scott, A. C., Swetnam, T. W., van der Werf, G. R. & Pyne, S. J. (2009), 'Fire in the earth system', *Science* **324**(5926), 481–484.

Burton, C., Betts, R. A., Jones, C. D., Feldpausch, T. R., Cardoso, M. & Anderson, L. O. (2020), 'El Niño driven changes in global fire 2015/16', *Frontiers in Earth Science* **8**, 199.

Chan, J. C. L. & Kepert, J. D. (2010), *Global Perspectives on Tropical Cyclones: From Science to Mitigation*, 1st edn, World Scientific Publishing Co. Pte. Ltd.

Chelton, D. B. & Risien, C. M. (2016), 'Zonal and meridional discontinuities and other issues with the HadISST1.1 dataset', `https://ir.library.oregonstate.edu/concern/defaults/kw52j9632`.

Chen, Y., Morton, D. C., Andela, N., Giglio, L. & Randerson, J. T. (2016), 'How much global burned area can be forecast on seasonal time scales using sea surface temperatures?', *Environmental Research Letters* **11**(4), 045001.

Chen, Y., Morton, D. C., Jin, Y., Collatz, G. J., Kasibhatla, P. S., van der Werf, G. R., DeFries, R. S. & Randerson, J. T. (2013), 'Long-term trends and interannual variability of forest, savanna and agricultural fires in South America', *Carbon Management* **4**(6), 617–638.

Chen, Y., Randerson, J. T. & Morton, D. C. (2015), 'Tropical North Atlantic ocean-atmosphere interactions synchronize forest carbon losses from hurricanes and Amazon fires', *Geophysical Research Letters* **42**(15), 6462–6470.

Chen, Y., Randerson, J. T., Morton, D. C., DeFries, R. S., Collatz, G. J., Kasibhatla, P. S., Giglio, L., Jin, Y. & Marlier, M. E. (2011), 'Forecasting fire season severity in South America using sea surface temperature anomalies', *Science* **334**(6057), 787–791.

Chou, K.-H., Wu, C.-C. & Wang, Y. (2011), 'Eyewall evolution of typhoons crossing the Philippines and Taiwan: an observational study', *Terrestrial, Atmospheric and Oceanic Sciences* **22**(6), 535–548.

Clark, T. L., Jenkins, M. A., Coen, J. L. & Packham, D. R. (1996), 'A coupled atmosphere-fire model: role of the convective froude number and dynamic fingering at the fireline', *International Journal of Wildland Fire* **6**(4), 177–190.

Copernicus Climate Change Service, Climate Data Store (2019), 'Fire danger indices historical data from the Copernicus Emergency Management Service', Copernicus Climate Change Service (C3S) Climate Data Store (CDS), DOI: 10.24381/cds.0e89c522.

Courtier, P., Thépaut, J.-N. & Hollingsworth, A. (1994), 'A strategy for operational implementation of 4D-Var, using an incremental approach', *Quarterly Journal of the Royal Meteorological Society* **120**(519), 1367–1387.

Cury, R. T. d. S., Balch, J. K., Brando, P. M., Andrade, R. B., Scervino, R. P. & Torezan, J. M. D. (2020), 'Higher fire frequency impaired woody species regeneration in a south-eastern Amazonian forest', *Journal of Tropical Ecology* **36**(4), 190–198.

Czaja, A., van der Vaart, P. & Marshall, J. (2002), 'A diagnostic study of the role of remote forcing in tropical Atlantic variability', *Journal of Climate* **15**(22), 3280–3290.

Davey, M. K., Brookshaw, A. & Ineson, S. (2014), 'The probability of the impact of ENSO on precipitation and near-surface temperature', *Climate Risk Management* **1**, 5–24.

de Souza, I. P., Andreoli, R. V., Kayano, M. T., Vargas, F. F., Cerón, W. L., Martins, J. A., Freitas, E. & de Souza, R. A. F. (2021), 'Seasonal precipitation variability modes over South America associated to El Niño-Southern Oscillation (ENSO) and non-ENSO components during the 1951–2016 period', *International Journal of Climatology* **41**(8), 4321–4338.

Deng, D. & Ritchie, E. A. (2023), 'High-resolution simulation of Tropical Cyclone Debbie (2017). Part I: the inner-core structure and evolution during offshore intensification', *Journal of the Atmospheric Sciences* **80**(2), 441–456.

Di Giuseppe, F., Pappenberger, F., Wetterhall, F., Krzeminski, B., Camia, A., Libertá, G. & San Miguel, J. (2016), 'The potential predictability of fire danger provided by numerical weather prediction', *Journal of Applied Meteorology and Climatology* **55**(11), 2469–2491.

Dijkstra, H. A. (2006), 'The ENSO phenomenon: theory and mechanisms', *Advances in Geosciences* **6**, 3–15.

Drosdowsky, W. (2006), 'Statistical prediction of ENSO (Nino 3) using sub-surface temperature data', *Geophysical Research Letters* **33**(3), L03710.

Emanuel, K. (2005), 'Increasing destructiveness of tropical cyclones over the past 30 years', *Nature* **436**(7051), 686–688.

Emanuel, K. (2020), 'Evidence that hurricanes are getting stronger', *Proceedings of the National Academy of Sciences of the United States of America* **117**(24), 13194–13195.

Emanuel, K., Callaghan, J. & Otto, P. (2008), 'A hypothesis for the redevelopment of warm-core cyclones over northern Australia', *Monthly Weather Review* **136**(10), 3863–3872.

Enfield, D. B. (1996), 'Relationships of inter-American rainfall to tropical Atlantic and Pacific SST variability', *Geophysical Research Letters* **23**(23), 3305–3308.

Enfield, D. B., Lee, S.-K. & Wang, C. (2006), 'How are large Western Hemisphere warm pools formed?', *Progress in Oceanography* **70**(2–4), 346–365.

Enfield, D. B. & Mayer, D. A. (1997), 'Tropical atlantic sea surface temperature variability and its relation to El Niño-Southern Oscillation', *Journal of Geophysical Research: Oceans* **102**(C1), 929–945.

Enfield, D. B., Mestas-Nuñez, A. M. & Trimble, P. J. (2001), 'The Atlantic Multidecadal Oscillation and its relation to rainfall and river flows in the continental U.S', *Geophysical Research Letters* **28**(10), 2077–2080.

European Centre for Medium-Range Weather Forecasts (2023), 'ERA5: uncertainty estimation', `https://confluence.ecmwf.int/display/CKB/ERA5%3A+uncertainty+estimation`.

Fanin, T. & van der Werf, G. R. (2017), 'Precipitation-fire linkages in Indonesia (1997–2015)', *Biogeosciences* **14**(18), 3995–4008.

Fernandes, K., Baethgen, W., Bernardes, S., DeFries, R., DeWitt, D. G., Goddard, L., Lavado, W., Lee, D. E., Padoch, C., Pinedo-Vasquez, M. & Uriarte, M. (2011), 'North tropical Atlantic influence on western Amazon fire season variability', *Geophysical Research Letters* **38**(12), L12701.

Ferreira Barbosa, M. L., Delgado, R. C., Forsad de Andrade, C., Teodoro, P. E., Silva Junior, C. A., Wanderley, H. S. & Capristo-Silva, G. F. (2021), 'Recent trends in the fire dynamics in Brazilian Legal Amazon: interaction between the ENSO phenomenon, climate and land use', *Environmental Development* **39**, 100648.

Folland, C. K., Colman, A. W., Rowell, D. P. & Davey, M. K. (2001), 'Predictability of Northeast Brazil rainfall and real-time forecast skill, 1987–98', *Journal of Climate* **14**(9), 1937–1958.

Folland, C. K., Palmer, T. N. & Parker, D. E. (1986), 'Sahel rainfall and worldwide sea temperatures, 1901–85', *Nature* **320**(6063), 602–607.

Friedl, M. A., Sulla-Menashe, D., Tan, B., Schneider, A., Ramankutty, N., Sibley, A. & Huang, X. (2010), 'MODIS Collection 5 global land cover: algorithm refinements and characterization of new datasets', *Remote Sensing of Environment* **114**(1), 168–182.

Gebremichael, M., Krajewski, W. F., Morrissey, M., Langerud, D., Huffman, G. J. & Adler, R. (2003), 'Error uncertainty analysis of GPCP Monthly rainfall products: a data-based simulation study', *Journal of Applied Meteorology and Climatology* **42**(12), 1837–1848.

Giglio, L., Csiszar, I. & Justice, C. O. (2006), 'Global distribution and seasonality of active fires as observed with the Terra and Aqua Moderate Resolution Imaging Spectroradiometer (MODIS) sensors', *Journal of Geophysical Research: Biogeosciences* **111**(G2), G02016.

Giglio, L., Schroeder, W., Hall, J. V. & Justice, C. O. (2020), 'MODIS Collection 6 Active Fire Product User's Guide Revision C', `https://modis-fire.umd.edu/files/MODIS_C6_Fire_User_Guide_C.pdf`.

Giglio, L., Schroeder, W. & Justice, C. O. (2016), 'The Collection 6 MODIS active fire detection algorithm and fire products', *Remote Sensing of Environment* **178**, 31–41.

Gill, A. E. (1980), 'Some simple solutions for heat-induced tropical circulation', *Quarterly Journal of the Royal Meteorological Society* **106**(449), 447–462.

Goldenberg, S. B., Landsea, C. W., Mestas-Nuñez, A. M. & Gray, W. M. (2001), 'The recent increase in Atlantic hurricane activity: causes and implications', *Science* **293**(5529), 474–479.

Goldenberg, S. B. & Shapiro, L. J. (1996), 'Physical mechanisms for the association of El Niño and West African rainfall with Atlantic major hurricane activity', *Journal of Climate* **9**(6), 1169–1187.

Good, S. A., Martin, M. J. & Rayner, N. A. (2013), 'EN4: quality controlled ocean temperature and salinity profiles and monthly objective analyses with uncertainty estimates', *Journal of Geophysical Research: Oceans* **118**(12), 6704–6716.

Gouretski, V. & Cheng, L. (2020), 'Correction for systematic errors in the global dataset of temperature profiles from mechanical bathythermographs', *Journal of Atmospheric and Oceanic Technology* **37**(5), 841–855.

Gouretski, V. & Reseghetti, F. (2010), 'On depth and temperature biases in bathythermograph data: development of a new correction scheme based on analysis of a global ocean database', *Deep-Sea Research Part I: Oceanographic Research Papers* **57**(6), 812–833.

Gray, W. M. (1968), 'Global view of the origin of tropical disturbances and storms', *Monthly Weather Review* **96**(10), 669–700.

Gray, W. M. (1984), 'Atlantic seasonal hurricane frequency. Part I: El Niño and 30 mb Quasi-Biennial Oscillation influences', *Monthly Weather Review* **112**(9), 1649–1668.

Grisogono, B. (2011), 'The angle of the near-surface wind-turning in weakly stable boundary layers', *Quarterly Journal of the Royal Meteorological Society* **137**(656), 700–708.

Hastenrath, S. (2000), 'Upper air mechanisms of the Southern Oscillation in the tropical Atlantic sector', *Journal of Geophysical Research: Atmospheres* **105**(D11), 14997–15009.

Hayashi, M., Jin, F.-F. & Stuecker, M. F. (2020), 'Dynamics for El Niño-La Niña asymmetry constrain equatorial-Pacific warming pattern', *Nature Communications* **11**(1), 4230.

He, J., Hon, K. K., Chan, P. W. & Li, Q. S. (2022), 'Dropsonde observations and numerical simulations of intensifying/weakening tropical cyclones over the northern South China Sea', *Weather* **77**(9), 332–338.

Hersbach, H., Bell, B., Berrisford, P., Biavati, G., Horányi, A., Muñoz Sabater, J., Nicolas, J., Peubey, C., Radu, R., Rozum, I., Schepers, D., Simmons, A., Soci, C., Dee, D. & Thépaut, J.-N. (2019*a*), 'ERA5 monthly averaged data on pressure levels from 1979 to present', Copernicus Climate Change Service (C3S) Climate Data Store (CDS), DOI: 10.24381/cds.6860a573.

Hersbach, H., Bell, B., Berrisford, P., Biavati, G., Horányi, A., Muñoz Sabater, J., Nicolas, J., Peubey, C., Radu, R., Rozum, I., Schepers, D., Simmons, A., Soci, C., Dee, D. & Thépaut, J.-N. (2019*b*), 'ERA5 monthly averaged data on single levels from 1979 to present', Copernicus Climate Change Service (C3S) Climate Data Store (CDS), DOI: 10.24381/cds.f17050d7.

Hersbach, H., Bell, B., Berrisford, P., Hirahara, S., Horányi, A., Muñoz-Sabater, J., Nicolas, J., Peubey, C., Radu, R., Schepers, D., Simmons, A., Soci, C., Abdalla, S., Abellan, X.,

Balsamo, G., Bechtold, P., Biavati, G., Bidlot, J., Bonavita, M., De Chiara, G., Dahlgren, P., Dee, D., Diamantakis, M., Dragani, R., Flemming, J., Forbes, R., Fuentes, M., Geer, A., Haimberger, L., Healy, S., Hogan, R. J., Hólm, E., Janisková, M., Keeley, S., Laloyaux, P., Lopez, P., Lupu, C., Radnoti, G., de Rosnay, P., Rozum, I., Vamborg, F., Villaume, S. & Thépaut, J.-N. (2020), 'The ERA5 global reanalysis', *Quarterly Journal of the Royal Meteorological Society* **146**(730), 1999–2049.

Hlywiak, J. & Nolan, D. S. (2022), 'The evolution of asymmetries in the tropical cyclone boundary layer wind field during landfall', *Monthly Weather Review* **150**(3), 529–549.

Hoell, A., Funk, C., Zinke, J. & Harrison, L. (2017), 'Modulation of the southern Africa precipitation response to the El Niño Southern Oscillation by the subtropical Indian Ocean Dipole', *Climate Dynamics* **48**(7), 2529–2540.

Hong, S.-Y. & Lim, J.-O. J. (2006), 'The WRF Single-Monent 6-Class Microphysics Scheme (WSM6)', *Journal of the Korean Meteorological Society* **42**(2), 129–151.

Hong, S.-Y., Noh, Y. & Dudhia, J. (2006), 'A new vertical diffusion package with an explicit treatment of entrainment processes', *Monthly Weather Review* **134**(9), 2318–2341.

Huffman, G. J., Adler, R. F., Arkin, P., Chang, A., Ferraro, R., Gruber, A., Janowiak, J., McNab, A., Rudolf, B. & Schneider, U. (1997), 'The Global Precipitation Climatology Project (GPCP) combined precipitation dataset', *Bulletin of the American Meteorological Society* **78**(1), 5–20.

Huffman, G. J. & Bolvin, D. T. (2018), 'TRMM and Other Data Precipitation Data Set Documentation', `https://docserver.gesdisc.eosdis.nasa.gov/public/project/GPM/3B42_3B43_doc_V7.pdf`.

Iacono, M. J., Delamere, J. S., Mlawer, E. J., Shephard, M. W., Clough, S. A. & Collins, W. D. (2008), 'Radiative forcing by long-lived greenhouse gases: calculations with the AER radiative transfer models', *Journal of Geophysical Research: Atmospheres* **113**(D13), D13103.

Iguchi, T., Kozu, T., Kwiatkowski, J., Meneghini, R., Awaka, J. & Okamoto, K. (2009), 'Uncertainties in the rain profiling algorithm for the TRMM precipitation radar', *Journal of the Meteorological Society of Japan* **87A**, 1–30.

Inoue, M., Handoh, I. C. & Bigg, G. R. (2002), 'Bimodal distribution of tropical cyclogenesis in the Caribbean: characteristics and environmental factors', *Journal of Climate* **15**(20), 2897–2905.

Izumo, T., Lengaigne, M., Vialard, J., Suresh, I. & Planton, Y. (2019), 'On the physical interpretation of the lead relation between warm water volume and the El Niño Southern Oscillation', *Climate Dynamics* **52**(5), 2923–2942.

Jiménez, P. A., Dudhia, J., González-Rouco, J. F., Navarro, J., Montávez, J. P. & García-Bustamante, E. (2012), 'A revised scheme for the WRF surface layer formulation', *Monthly Weather Review* **140**(3), 898–918.

Jin, E. K., Kinter, J. L., III, Wang, B., Park, C.-K., Kang, I.-S., Kirtman, B. P., Kug, J.-S., Kumar, A., Luo, J.-J., Schemm, J., Shukla, J. & Yamagata, T. (2008), 'Current status of ENSO prediction skill in coupled ocean-atmosphere models', *Climate Dynamics* **31**(6), 647–664.

Jin, F.-F. (1997*a*), 'An equatorial ocean recharge paradigm for ENSO. Part I: conceptual model', *Journal of the Atmospheric Sciences* **54**(7), 811–829.

Jin, F.-F. (1997*b*), 'An equatorial ocean recharge paradigm for ENSO. Part II: a stripped-down coupled model', *Journal of the Atmospheric Sciences* **54**(7), 830–847.

Jordan, C. L. (1958), 'Mean soundings for the West Indies area', *Journal of Meteorology* **15**(1), 91–97.

Julian, P. R. & Chervin, R. M. (1978), 'A study of the Southern Oscillation and Walker Circulation phenomenon', *Monthly Weather Review* **106**(10), 1433–1451.

Kaplan, A., Kushnir, Y., Cane, M. A. & Blumenthal, M. B. (1997), 'Reduced space optimal analysis for historical data sets: 136 years of Atlantic sea surface temperatures', *Journal of Geophysical Research: Oceans* **102**(C13), 27835–27860.

Kepert, J. (2001), 'The dynamics of boundary layer jets within the tropical cyclone core. Part I: linear theory', *Journal of the Atmospheric Sciences* **58**(17), 2469–2484.

Kepert, J. & Wang, Y. (2001), 'The dynamics of boundary layer jets within the tropical cyclone core. Part II: nonlinear enhancement', *Journal of the Atmospheric Sciences* **58**(17), 2485–2501.

Khaira, U. & Astitha, M. (2023), 'Exploring the real-time WRF forecast skill for four Tropical Storms, Isaias, Henri, Elsa and Irene, as they impacted the Northeast United States', *Remote Sensing* **15**(13), 3219.

Kiladis, G. N. & Diaz, H. F. (1989), 'Global climatic anomalies associated with extremes in the Southern Oscillation', *Journal of Climate* **2**(9), 1069–1090.

Killick, R. (2021), 'EN.4.2.2 Product User Guide', Met Office Hadley Centre, `https://www.metoffice.gov.uk/hadobs/en4/EN.4.2.2_Product_User_Guide_v1.0.pdf`.

King, A. D. & Vincent, C. L. (2018), 'Using global and regional model simulations to understand Maritime Continent wet-season rainfall variability', *Geophysical Research Letters* **45**(22), 12534–12543.

Klein, S. A., Soden, B. J. & Lau, N.-C. (1999), 'Remote sea surface temperature variations during ENSO: evidence for a tropical atmospheric bridge', *Journal of Climate* **12**(4), 917–932.

Knapp, K. R. (2019), 'International Best Track Archive for Climate Stewardship (IBTrACS) Technical Documentation', `https://www.ncei.noaa.gov/sites/default/files/2021-07/IBTrACS_version4_Technical_Details.pdf`.

Knapp, K. R., Diamond, H. J., Kossin, J. P., Kruk, M. C. & Schreck, C. J., III (2018), 'International Best Track Archive for Climate Stewardship (IBTrACS) Project, Version 4', NOAA National Centers for Environmental Information, DOI: 10.25921/82ty-9e16.

Knapp, K. R., Kruk, M. C., Levinson, D. H., Diamond, H. J. & Neumann, C. J. (2010), 'The International Best Track Archive for Climate Stewardship (IBTrACS): unifying tropical cyclone data', *Bulletin of the American Meteorological Society* **91**(3), 363–376.

Knight, J. R., Allan, R. J., Folland, C. K., Vellinga, M. & Mann, M. E. (2005), 'A signature of persistent natural thermohaline circulation cycles in observed climate', *Geophysical Research Letters* **32**(20), L20708.

Knupp, K. R., Walters, J. & Biggerstaff, M. (2006), 'Doppler profiler and radar observations of boundary layer variability during the landfall of Tropical Storm Gabrielle', *Journal of the Atmospheric Sciences* **63**(1), 234–251.

Knupp, K. R., Walters, J. & McCaul, E. W., Jr. (2000), 'Doppler profiler observations of Hurricane Georges at landfall', *Geophysical Research Letters* **27**(20), 3361–3364.

Knutson, T. R., McBride, J. L., Chan, J., Emanuel, K., Holland, G., Landsea, C., Held, I., Kossin, J. P., Srivastava, A. K. & Sugi, M. (2010), 'Tropical cyclones and climate change', *Nature Geoscience* **3**(3), 157–163.

Kossin, J. P., Knapp, K. R., Olander, T. L. & Velden, C. S. (2020), 'Global increase in major tropical cyclone exceedance probability over the past four decades', *Proceedings of the National Academy of Sciences of the United States of America* **117**(22), 11975–11980.

Kothawale, D. R. & Rajeevan, M. (2017), 'Monthly, seasonal and annual rainfall time series for all-India, homogeneous regions and meteorological subdivisions: 1871–2016', Indian Institute of Tropical Meteorology, Earth System Science Organization, Ministry of Earth Sciences, `https://www.tropmet.res.in/~lip/Publication/RR-pdf/RR-138.pdf`.

Krishnan, R., Mujumdar, M., Vaidya, V., Ramesh, K. V. & Satyan, V. (2003), 'The abnormal Indian summer monsoon of 2000', *Journal of Climate* **16**(8), 1177–1194.

Kushnir, Y. (1994), 'Interdecadal variations in North Atlantic sea surface temperature and associated atmospheric conditions', *Journal of Climate* **7**(1), 141–157.

Ladwig, W. (2017), 'wrf-python (Version 1.2.0)', Boulder, Colorado: UCAR/NCAR, DOI: 10.5065/D6W094P1.

Latif, M., Anderson, D., Barnett, T., Cane, M., Kleeman, R., Leetmaa, A., O'Brien, J., Rosati, A. & Schneider, E. (1998), 'A review of the predictability and prediction of ENSO', *Journal of Geophysical Research: Oceans* **103**(C7), 14375–14393.

Lenssen, N. J. L., Goddard, L. & Mason, S. (2020), 'Seasonal forecast skill of ENSO teleconnection maps', *Weather and Forecasting* **35**(6), 2387–2406.

L'Heureux, M. L., Takahashi, K., Watkins, A. B., Barnston, A. G., Becker, E. J., Di Liberto, T. E., Gamble, F., Gottschalck, J., Halpert, M. S., Huang, B., Mosquera-Vásquez, K. & Wittenberg, A. T. (2017), 'Observing and predicting the 2015/16 El Niño', *Bulletin of the American Meteorological Society* **98**(7), 1363–1382.

Li, F., Zeng, X. D. & Levis, S. (2012), 'A process-based fire parameterization of intermediate complexity in a dynamic global vegetation model', *Biogeosciences* **9**(7), 2761–2780.

Li, J. & Ruan, C. (2018), 'The North Atlantic-Eurasian teleconnection in summer and its effects on Eurasian climates', *Environmental Research Letters* **13**(2), 024007.

Li, L. & Chakraborty, P. (2021), 'Birth of a cold core in tropical cyclones past landfall', *Physical Review Fluids* **6**(5), L051801.

Li, Z., Thompson, E. J., Behrangi, A., Chen, H. & Yang, J. (2023), 'Performance of GPCP Daily products over oceans: evaluation using passive aquatic listeners', *Geophysical Research Letters* **50**(11), e2023GL104310.

Liao, F., Su, R., Chan, P.-W., Qi, Y. & Hon, K.-K. (2019), 'Observational study on the characteristics of the boundary layer during changes in the intensity of tropical cyclones landing in Guangdong, China', *Advances in Meteorology* **2019**, 8072914.

Liew, S. C. (2013), Anthropogenic and climatic influences on biomass burning in Insular Southeast Asia, *in* '2013 IEEE International Geoscience and Remote Sensing Symposium - IGARSS'.

Lin, J. & Qian, T. (2019), 'Switch between El Nino and La Nina is caused by subsurface ocean waves likely driven by lunar tidal forcing', *Scientific Reports* **9**(1), 13106.

Lin, N., Emanuel, K., Oppenheimer, M. & Vanmarcke, E. (2012), 'Physically based assessment of hurricane surge threat under climate change', *Nature Climate Change* **2**(6), 462–467.

Lindzen, R. S. & Hou, A. V. (1988), 'Hadley circulations for zonally averaged heating centered off the equator', *Journal of the Atmospheric Sciences* **45**(17), 2416–2427.

Liu, Y., Chiang, J. C. H., Chou, C. & Patricola, C. M. (2014), 'Atmospheric teleconnection mechanisms of extratropical North Atlantic SST influence on Sahel rainfall', *Climate Dynamics* **43**(9), 2797–2811.

Lorenz, E. N. (1967), *The Nature and Theory of the General Circulation of the Atmosphere*, World Meteorological Organization.

Losada, T., Rodriguez-Fonseca, B., Mohino, E., Bader, J., Janicot, S. & Mechoso, C. R. (2012), 'Tropical SST and Sahel rainfall: a non-stationary relationship', *Geophysical Research Letters* **39**(12), L12705.

Maloney, E. D. & Hartmann, D. L. (2000), 'Modulation of hurricane activity in the Gulf of Mexico by the Madden-Julian oscillation', *Science* **287**(5460), 2002–2004.

Mangeon, S., Voulgarakis, A., Gilham, R., Harper, A., Sitch, S. & Folberth, G. (2016), 'INFERNO: a fire and emissions scheme for the UK Met Office's Unified Model', *Geoscientific Model Development* **9**(8), 2685–2700.

Mann, M. E., Steinman, B. A. & Miller, S. K. (2014), 'On forced temperature changes, internal variability, and the AMO', *Geophysical Research Letters* **41**(9), 3211–3219.

Marengo, J. A., Souza, C. M., Jr., Thonicke, K., Burton, C., Halladay, K., Betts, R. A., Alves, L. M. & Soares, W. R. (2018), 'Changes in climate and land use over the Amazon region: current and future variability and trends', *Frontiers in Earth Science* **6**, 228.

McGregor, S., Timmermann, A., Schneider, N., Stuecker, M. F. & England, M. H. (2012), 'The effect of the South Pacific Convergence Zone on the termination of El Niño events and the meridional asymmetry of ENSO', *Journal of Climate* **25**(16), 5566–5586.

McPhaden, M. J. (2004), 'Evolution of the 2002/03 El Niño', *Bulletin of the American Meteorological Society* **85**(5), 677–696.

Moron, V., Bigot, S. & Roucou, P. (1995), 'Rainfall variability in subequatorial America and Africa and relationships with the main sea-surface temperature modes (1951–1990)', *International Journal of Climatology* **15**(12), 1297–1322.

Mutai, C. C., Ward, M. N. & Colman, A. W. (1998), 'Towards the prediction of the East Africa short rains based on sea-surface temperature-atmosphere coupling', *International Journal of Climatology* **18**(9), 975–997.

National Aeronautics and Space Administration (2017), 'Precipitation Processing System Tropical Rainfall Measuring Mission: File Specification for TRMM Products Version 7.006', `https://gpm.nasa.gov/sites/default/files/2020-02/filespec.TRMM_.V7.pdf`.

O'Kane, T. J., Sandery, P. A., Monselesan, D. P., Sakov, P., Chamberlain, M. A., Matear, R. J., Collier, M. A., Squire, D. T. & Stevens, L. (2019), 'Coupled data assimilation and ensemble initialization with application to multiyear ENSO prediction', *Journal of Climate* **32**(4), 997–1024.

Park, S., Kang, D., Yoo, C., Im, J. & Lee, M.-I. (2020), 'Recent ENSO influence on East African drought during rainy seasons through the synergistic use of satellite and reanalysis data', *ISPRS Journal of Photogrammetry and Remote Sensing* **162**, 17–26.

Pendergrass, A. G. & Willoughby, H. E. (2009), 'Diabatically induced secondary flows in tropical cyclones. Part I: quasi-steady forcing', *Monthly Weather Review* **137**(3), 805–821.

Petrova, D., Ballester, J., Koopman, S. J. & Rodó, X. (2020), 'Multiyear statistical prediction of ENSO enhanced by the tropical Pacific observing system', *Journal of Climate* **33**(1), 163–174.

Petrova, D., Koopman, S. J., Ballester, J. & Rodó, X. (2017), 'Improving the long-lead predictability of El Niño using a novel forecasting scheme based on a dynamic components model', *Climate Dynamics* **48**(3), 1249–1276.

Phlips, P. J. & Gill, A. E. (1987), 'An analytic model of the heat-induced tropical circulation in the presence of a mean wind', *Quarterly Journal of the Royal Meteorological Society* **113**(475), 213–236.

Picaut, J., Masia, F. & du Penhoat, Y. (1997), 'An advective-reflective conceptual model for the oscillatory nature of the ENSO', *Science* **277**(5326), 663–666.

Planton, Y., Vialard, J., Guilyardi, E., Lengaigne, M. & Izumo, T. (2018), 'Western Pacific oceanic heat content: a better predictor of La Niña than of El Niño', *Geophysical Research Letters* **45**(18), 9824–9833.

Pope, V. D., Gallani, M. L., Rowntree, P. R. & Stratton, R. A. (2000), 'The impact of new physical parametrizations in the Hadley Centre climate model: HadAM3', *Climate Dynamics* **16**(2), 123–146.

Powell, M. D. (1982), 'The transition of the Hurricane Frederic boundary-layer wind field from the open Gulf of Mexico to landfall', *Monthly Weather Review* **110**(12), 1912–1932.

Ramesh, N. & Murtugudde, R. (2013), 'All flavours of El Niño have similar early subsurface origins', *Nature Climate Change* **3**(1), 42–46.

Ramos, A. M., Russo, A., DaCamara, C. C., Nunes, S., Sousa, P., Soares, P. M. M., Lima, M. M., Hurduc, A. & Trigo, R. M. (2023), 'The compound event that triggered the destructive fires of October 2017 in Portugal', *iScience* **26**(3), 106141.

Rasmusson, E. M. & Carpenter, T. H. (1982), 'Variations in tropical sea surface temperature and surface wind fields associated with the Southern Oscillation/El Niño', *Monthly Weather Review* **110**(5), 354–384.

Rauniyar, S. P., Protat, A. & Kanamori, H. (2017), 'Uncertainties in TRMM-Era multisatellite-based tropical rainfall estimates over the Maritime Continent', *Earth and Space Science* **4**(5), 275–302.

Rayner, N. A., Parker, D. E., Horton, E. B., Folland, C. K., Alexander, L. V., Rowell, D. P., Kent, E. C. & Kaplan, A. (2003), 'Global analyses of sea surface temperature, sea ice, and night marine air temperature since the late nineteenth century', *Journal of Geophysical Research: Atmospheres* **108**(D14), 4407.

Ren, Y., Zhang, J. A., Guimond, S. R. & Wang, X. (2019), 'Hurricane boundary layer height relative to storm motion from GPS dropsonde composites', *Atmosphere* **10**(6), 339.

Rodríguez-Pérez, J. R., Ordóñez, C., Roca-Pardiñas, J., Vecín-Arias, D. & Castedo-Dorado, F. (2020), 'Evaluating lightning-caused fire occurrence using spatial generalized additive models: a case study in central Spain', *Risk Analysis* **40**(7), 1418–1437.

Rodwell, M. J. & Hoskins, B. J. (2001), 'Subtropical anticyclones and summer monsoons', *Journal of Climate* **14**(15), 3192–3211.

Rogers, R., Reasor, P. & Lorsolo, S. (2013), 'Airborne doppler observations of the inner-core structural differences between intensifying and steady-state tropical cyclones', *Monthly Weather Review* **141**(9), 2970–2991.

Ropelewski, C. F. & Halpert, M. S. (1987), 'Global and regional scale precipitation patterns associated with the El Niño/Southern Oscillation', *Monthly Weather Review* **115**(8), 1606–1626.

Ropelewski, C. F. & Halpert, M. S. (1989), 'Precipitation patterns associated with the high index phase of the Southern Oscillation', *Journal of Climate* **2**(3), 268–284.

Rowell, D. P., Folland, C. K., Maskell, K. & Ward, M. N. (1995), 'Variability of summer rainfall over tropical North Africa (1906–92): observations and modelling', *Quarterly Journal of the Royal Meteorological Society* **121**(523), 669–704.

Schlesinger, M. E. & Ramankutty, N. (1994), 'An oscillation in the global climate system of period 65–70 years', *Nature* **367**(6465), 723–726.

Schneider, T. (2006), 'The general circulation of the atmosphere', *Annual Review of Earth and Planetary Sciences* **34**, 655–688.

Schroeder, W., Prins, E., Giglio, L., Csiszar, I., Schmidt, C., Morisette, J. & Morton, D. (2008), 'Validation of GOES and MODIS active fire detection products using ASTER and ETM+ data', *Remote Sensing of Environment* **112**(5), 2711–2726.

Schubert, W. H. & Hack, J. J. (1983), 'Transformed Eliassen balanced vortex model', *Journal of the Atmospheric Sciences* **40**(6), 1571–1583.

Shapiro, L. J. (1983), 'The asymmetric boundary layer flow under a translating hurricane', *Journal of the Atmospheric Sciences* **40**(8), 1984–1998.

Shapiro, L. J. (1987), 'Month-to-month variability of the Atlantic tropical circulation and its relationship to tropical storm formation', *Monthly Weather Review* **115**(11), 2598–2614.

Shapiro, L. J. & Willoughby, H. E. (1982), 'The response of balanced hurricanes to local sources of heat and momentum', *Journal of the Atmospheric Sciences* **39**(2), 378–394.

Silva Junior, C. H. L., Anderson, L. O., Silva, A. L., Almeida, C. T., Dalagnol, R., Pletsch, M. A. J. S., Penha, T. V., Paloschi, R. A. & Aragão, L. E. O. C. (2019), 'Fire responses to the 2010 and 2015/2016 Amazonian droughts', *Frontiers in Earth Science* **7**, 97.

Sitkowski, M., Kossin, J. P., Rozoff, C. M. & Knaff, J. A. (2012), 'Hurricane eyewall replacement cycle thermodynamics and the relict inner eyewall circulation', *Monthly Weather Review* **140**(12), 4035–4045.

Skamarock, W. C., Klemp, J. B., Dudhia, J., Gill, D. O., Liu, Z., Berner, J., Wang, W., Powers, J. G., Duda, M. G., Barker, D. & Huang, X.-y. (2021), 'A Description of the Advanced Research WRF Model Version 4.3 (No. NCAR/TN-556+STR)', DOI: 10.5065/1dfh-6p97.

Sparks, N. & Toumi, R. (2020), 'Pacific subsurface ocean temperature as a long-range predictor of South China tropical cyclone landfall', *Communications Earth & Environment* **1**(1), 30.

Sparks, N. & Toumi, R. (2022*a*), 'The dependence of tropical cyclone pressure tendency on size', *Geophysical Research Letters* **49**(19), e2022GL098926.

Sparks, N. & Toumi, R. (2022*b*), 'A physical model of tropical cyclone central pressure filling at landfall', *Journal of the Atmospheric Sciences* **79**(10), 2585–2599.

Srivastava, G., Chakraborty, A. & Nanjundiah, R. S. (2019), 'Multidecadal see-saw of the impact of ENSO on Indian and West African summer monsoon rainfall', *Climate Dynamics* **52**(11), 6633–6649.

Stuivenvolt Allen, J., Wang, S.-Y. S., LaPlante, M. D. & Yoon, J.-H. (2021), 'Three western Pacific typhoons strengthened fire weather in the recent Northwest U.S. conflagration', *Geophysical Research Letters* **48**(3), e2020GL091430.

Suarez, M. J. & Schopf, P. S. (1988), 'A delayed action oscillator for ENSO', *Journal of the Atmospheric Sciences* **45**(21), 3283–3287.

Sun, Q., Wu, B., Zhou, T.-J. & Yan, Z.-X. (2018), 'ENSO hindcast skill of the IAP-DecPreS near-term climate prediction system: comparison of full-field and anomaly initialization', *Atmospheric and Oceanic Science Letters* **11**(1), 54–62.

Sutton, R. T. & Hodson, D. L. R. (2005), 'Atlantic Ocean forcing of North American and European summer climate', *Science* **309**(5731), 115–118.

Takaya, Y., Kosaka, Y., Watanabe, M. & Maeda, S. (2021), 'Skilful predictions of the Asian summer monsoon one year ahead', *Nature Communications* **12**(1), 2094.

Tang, B. H. & Neelin, J. D. (2004), 'ENSO unfluence on Atlantic hurricanes via tropospheric warming', *Geophysical Research Letters* **31**(24), L24204.

Tartaglione, C. A., Smith, S. R. & O'Brien, J. J. (2003), 'ENSO impact on hurricane landfall probabilities for the Caribbean', *Journal of Climate* **16**(17), 2925–2931.

Thomsen, G. L., Smith, R. K. & Montgomery, M. T. (2015), 'Tropical cyclone flow asymmetries induced by a uniform flow revisited', *Journal of Advances in Modeling Earth Systems* **7**(3), 1265–1284.

Thonicke, K., Spessa, A., Prentice, I. C., Harrison, S. P., Dong, L. & Carmona-Moreno, C. (2010), 'The influence of vegetation, fire spread and fire behaviour on biomass burning and trace gas emissions: results from a process-based model', *Biogeosciences* **7**(6), 1991–2011.

Timmermann, A., An, S.-I., Kug, J.-S., Jin, F.-F., Cai, W., Capotondi, A., Cobb, K. M., Lengaigne, M., McPhaden, M. J., Stuecker, M. F., Stein, K., Wittenberg, A. T., Yun, K.-S., Bayr, T., Chen, H.-C., Chikamoto, Y., Dewitte, B., Dommenget, D., Grothe, P., Guilyardi, E., Ham, Y.-G., Hayashi, M., Ineson, S., Kang, D., Kim, S., Kim, W., Lee, J.-Y., Li, T., Luo, J.-J., McGregor, S., Planton, Y., Power, S., Rashid, H., Ren, H.-L., Santoso, A., Takahashi, K., Todd, A., Wang, G., Wang, G., Xie, R., Yang, W.-H., Yeh, S.-W., Yoon, J., Zeller, E. & Zhang, X. (2018), 'El Niño-Southern Oscillation complexity', *Nature* **559**(7715), 535–545.

Ting, M., Kushnir, Y. & Li, C. (2014), 'North Atlantic Multidecadal SST Oscillation: external forcing versus internal variability', *Journal of Marine Systems* **133**, 27–38.

Trenberth, K. (2005), 'Uncertainty in hurricanes and global warming', *Science* **308**(5729), 1753–1754.

Tropical Rainfall Measuring Mission (TRMM) (2011), 'TRMM (TMPA/3B43) Rainfall Estimate L3 1 month 0.25 degree x 0.25 degree V7, Greenbelt, MD', Goddard Earth Sciences Data and Information Services Center (GES DISC), DOI: 10.5067/TRMM/TMPA/MONTH/7.

Tse, K. T., Li, S. W., Chan, P. W., Mok, H. Y. & Weerasuriya, A. U. (2013), 'Wind profile observations in tropical cyclone events using wind-profilers and doppler SODARs', *Journal of Wind Engineering and Industrial Aerodynamics* **115**, 93–103.

Vallis, G. K. (2017), *Atmospheric and Oceanic Fluid Dynamics: Fundamentals and Large-Scale Circulation*, 2nd edn, Cambridge University Press.

van der Werf, G. R., Randerson, J. T., Giglio, L., Collatz, G. J., Mu, M., Kasibhatla, P. S., Morton, D. C., DeFries, R. S., Jin, Y. & van Leeuwen, T. T. (2010), 'Global fire emissions and the contribution of deforestation, savanna, forest, agricultural, and peat fires (1997–2009)', *Atmospheric Chemistry and Physics* **10**(23), 11707–11735.

Vellinga, M. & Milton, S. F. (2018), 'Drivers of interannual variability of the East African "Long Rains"', *Quarterly Journal of the Royal Meteorological Society* **144**(712), 861–876.

Vigaud, N., Lyon, B. & Giannini, A. (2017), 'Sub-seasonal teleconnections between convection over the Indian Ocean, the East African long rains and tropical Pacific surface temperatures', *International Journal of Climatology* **37**(3), 1167–1180.

Vigh, J. L. & Schubert, W. H. (2009), 'Rapid development of the tropical cyclone warm core', *Journal of the Atmospheric Sciences* **66**(11), 3335–3350.

Wakefield, R. A., Basara, J. B., Shepherd, J. M., Brauer, N., Furtado, J. C., Santanello, J. A., Jr. & Edwards, R. (2021), 'The inland maintenance and reintensification of Tropical Storm Bill (2015). Part I: contributions of the brown ocean effect', *Journal of Hydrometeorology* **22**(10), 2675–2693.

Wallace, J. M. & Hobbs, P. V. (2006), *Atmospheric Science: An Introductory Survey*, 2nd edn, Elsevier. Inc.

Wang, C. (2001), 'A unified oscillator model for the El Niño-Southern Oscillation', *Journal of Climate* **14**(1), 98–115.

Wang, C. (2002), 'Atmospheric circulation cells associated with the El Niño-Southern Oscillation', *Journal of Climate* **15**(4), 399–419.

Wang, C. (2018), 'A review of ENSO theories', *National Science Review* **5**(6), 813–825.

Wang, C. & Enfield, D. B. (2003), 'A further study of the tropical Western Hemisphere warm pool', *Journal of Climate* **16**(10), 1476–1493.

Wang, C., Lee, S.-K. & Enfield, D. B. (2008), 'Atlantic warm pool acting as a link between Atlantic Multidecadal Oscillation and Atlantic tropical cyclone activity', *Geochemistry, Geophysics, Geosystems* **9**(5), Q05V03.

Wang, C., Weisberg, R. H. & Virmani, J. I. (1999), 'Western Pacific interannual variability associated with the El Niño-Southern Oscillation', *Journal of Geophysical Research: Oceans* **104**(C3), 5131–5149.

Wang, H. & Wang, Y. (2014), 'A numerical study of Typhoon Megi (2010). Part I: rapid intensification', *Monthly Weather Review* **142**(1), 29–48.

Wang, H. & Wang, Y. (2021), 'A numerical study of Typhoon Megi (2010). Part II: eyewall evolution crossing the Luzon Island', *Monthly Weather Review* **149**(2), 375–394.

Wang, S. & Toumi, R. (2019), 'Impact of dry midlevel air on the tropical cyclone outer circulation', *Journal of the Atmospheric Sciences* **76**(6), 1809–1826.

Wang, S. & Toumi, R. (2021), 'Recent migration of tropical cyclones toward coasts', *Science* **371**(6528), 514–517.

Wang, S. & Toumi, R. (2022), 'An analytic model of the tropical cyclone outer size', *npj Climate and Atmospheric Science* **5**(1), 46.

Wang, W., Bruyère, C., Duda, M., Dudhia, J., Gill, D., Kavulich, M., Werner, K., Chen, M., Lin, H.-C., Michalakes, J., Rizvi, S., Zhang, X., Berner, J., Munoz-Esparza, D., Reen, B., Ha, S., Fossell, K., Beezley, J. D., Coen, J. L. & Mandel, J. (2022), 'User's Guide for the Advanced Research WRF (ARW) Modeling System, Version 4', `https://www2.mmm.ucar.edu/wrf/users/docs/user_guide_v4/contents.html`.

Wang, Y., Feng, J., Li, J., An, R. & Wang, L. (2020), 'Variability of boreal spring Hadley circulation over the Asian monsoon domain and its relationship with tropical SST', *Climate Dynamics* **54**(3), 1655–1669.

Wang, Y., Li, Y., Xu, J., Tan, Z.-M. & Lin, Y. (2021), 'The intensity dependence of tropical cyclone intensification rate in a simplified energetically based dynamical system model', *Journal of the Atmospheric Sciences* **78**(7), 2033–2045.

Webster, P. J., Holland, G. J., Curry, J. A. & Chang, H.-R. (2005), 'Changes in tropical cyclone number, duration, and intensity in a warming environment', *Science* **309**(5742), 1844–1846.

Weisberg, R. H. & Wang, C. (1997), 'A western Pacific oscillator paradigm for the El Niño-Southern Oscillation', *Geophysical Research Letters* **24**(7), 779–782.

Wills, R. C. J., Armour, K. C., Battisti, D. S. & Hartmann, D. L. (2019), 'Ocean-atmosphere dynamical coupling fundamental to the Atlantic Multidecadal Oscillation', *Journal of Climate* **32**(1), 251–272.

Wilson, R. M. (1999), 'Statistical aspects of major (intense) hurricanes in the Atlantic basin during the past 49 hurricane seasons (1950–1998): implications for the current season', *Geophysical Research Letters* **26**(19), 2957–2960.

Wooster, M. J., Perry, G. L. W. & Zoumas, A. (2012), 'Fire, drought and El Niño relationships on Borneo (Southeast Asia) in the pre-MODIS era (1980–2000)', *Biogeosciences* **9**(1), 317–340.

Wu, C.-C., Cheng, H.-J., Wang, Y. & Chou, K.-H. (2009), 'A numerical investigation of the eyewall evolution in a landfalling typhoon', *Monthly Weather Review* **137**(1), 21–40.

Wu, C.-C., Chou, K.-H., Cheng, H.-J. & Wang, Y. (2003), 'Eyewall contraction, breakdown and reformation in a landfalling typhoon', *Geophysical Research Letters* **30**(17), 1887.

Yang, M.-J., Wu, Y.-C. & Liou, Y.-C. (2018), 'The study of inland eyewall reformation of Typhoon Fanapi (2010) using numerical experiments and vorticity budget analysis', *Journal of Geophysical Research: Atmospheres* **123**(17), 9604–9623.

Yang, S.-C., Kalnay, E., Cai, M. & Rienecker, M. M. (2008), 'Bred vectors and tropical Pacific forecast errors in the NASA coupled general circulation model', *Monthly Weather Review* **136**(4), 1305–1326.

Yanto, Rajagopalan, B. & Zagona, E. (2016), 'Space-time variability of Indonesian rainfall at inter-annual and multi-decadal time scales', *Climate Dynamics* **47**(9), 2975–2989.

Yoon, J.-H. (2016), 'Multi-model analysis of the Atlantic influence on southern Amazon rainfall', *Atmospheric Science Letters* **17**(2), 122–127.

Yoon, J.-H. & Zeng, N. (2010), 'An Atlantic influence on Amazon rainfall', *Climate Dynamics* **34**(2), 249–264.

Yuan, C., Tozuka, T., Landman, W. A. & Yamagata, T. (2014), 'Dynamical seasonal prediction of southern African summer precipitation', *Climate Dynamics* **42**(11), 3357–3374.

Zehnder, J. A. (2023), 'Tropical cyclone', *Encyclopædia Britannica*, `https://www.britannica.com/science/tropical-cyclone`.

Zeng, N., Yoon, J.-H., Marengo, J. A., Subramaniam, A., Nobre, C. A., Mariotti, A. & Neelin, J. D. (2008), 'Causes and impacts of the 2005 Amazon drought', *Environmental Research Letters* **3**(1), 014002.

Zhang, G., Li, X., Perrie, W. & Zhang, J. A. (2021), 'Tropical cyclone winds and inflow angle asymmetry from SAR imagery', *Geophysical Research Letters* **48**(20), e2021GL095699.

Zhang, J. A. & Uhlhorn, E. W. (2012), 'Hurricane sea surface inflow angle and an observation-based parametric model', *Monthly Weather Review* **140**(11), 3587–3605.

Zhang, L., Wang, C. & Wu, L. (2012), 'Low-frequency modulation of the Atlantic warm pool by the Atlantic Multidecadal Oscillation', *Climate Dynamics* **39**(7), 1661–1671.

Zhang, S., Wang, H., Jiang, H. & Ma, W. (2021), 'Evaluation of ENSO prediction skill changes since 2000 based on multimodel hindcasts', *Atmosphere* **12**(3), 365.

Zhao, S., Jin, F.-F. & Stuecker, M. F. (2021), 'Understanding lead times of warm water volumes to ENSO sea surface temperature anomalies', *Geophysical Research Letters* **48**(19), e2021GL094366.

Zhou, X. & Wang, B. (2011), 'Mechanism of concentric eyewall replacement cycles and associated intensity change', *Journal of the Atmospheric Sciences* **68**(5), 972–988.

Appendix A

Supplementary Plots for Chapter 4

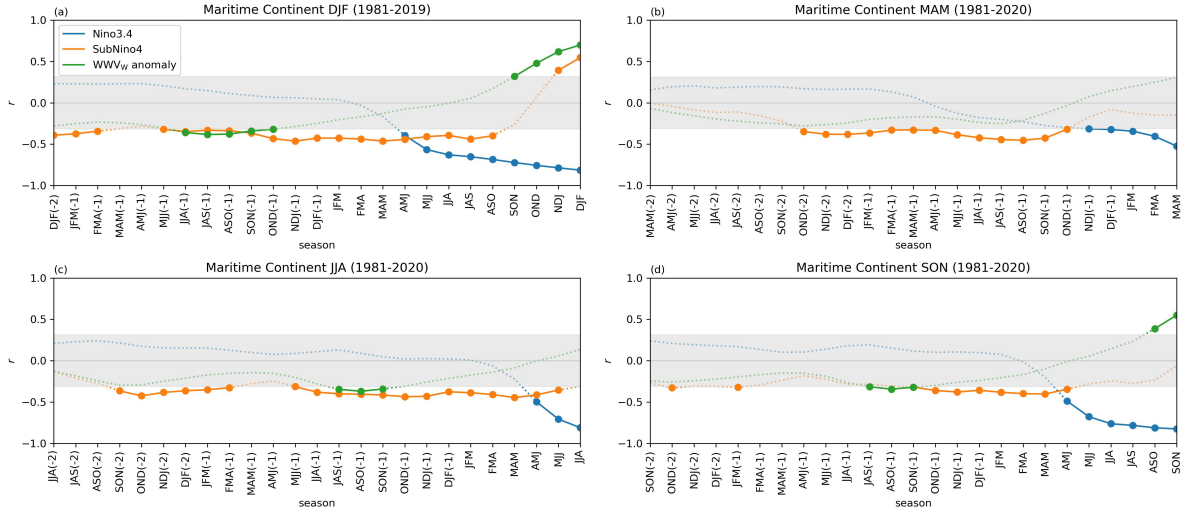


Figure A.1: Same as Figure 4.7 but showing r.

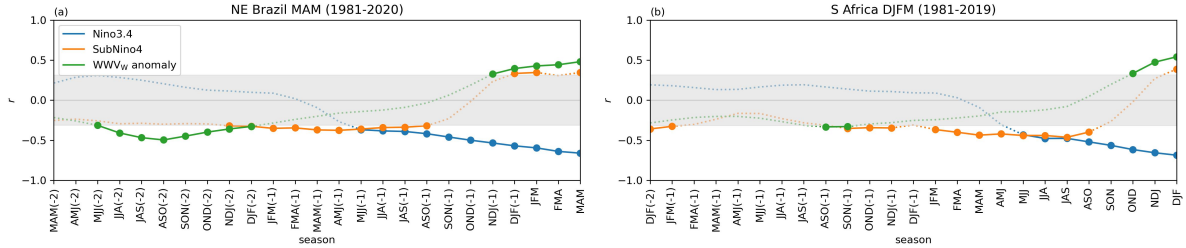


Figure A.2: Same as Figure 4.8 but showing r.

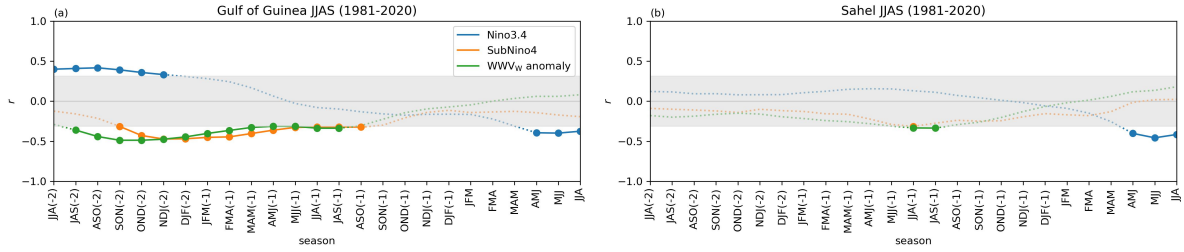


Figure A.3: Same as Figure 4.9 but showing r.

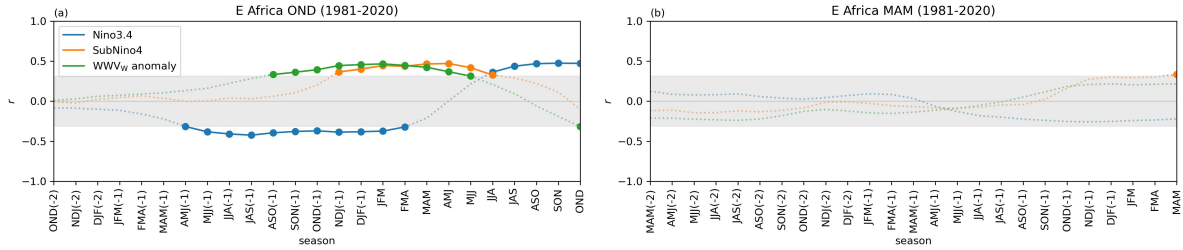


Figure A.4: Same as Figure 4.10 but showing r.

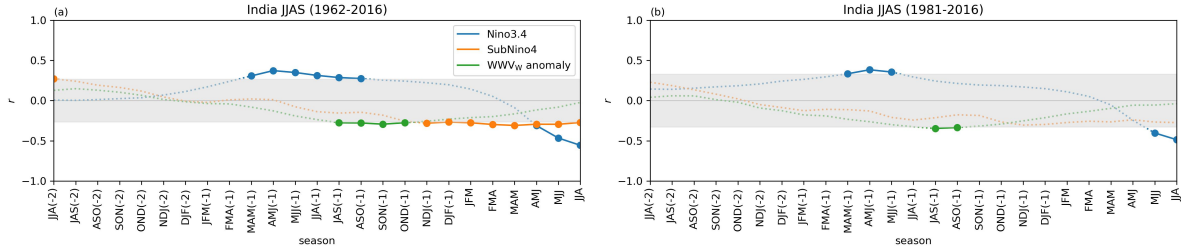


Figure A.5: Same as Figure 4.11 but showing r.

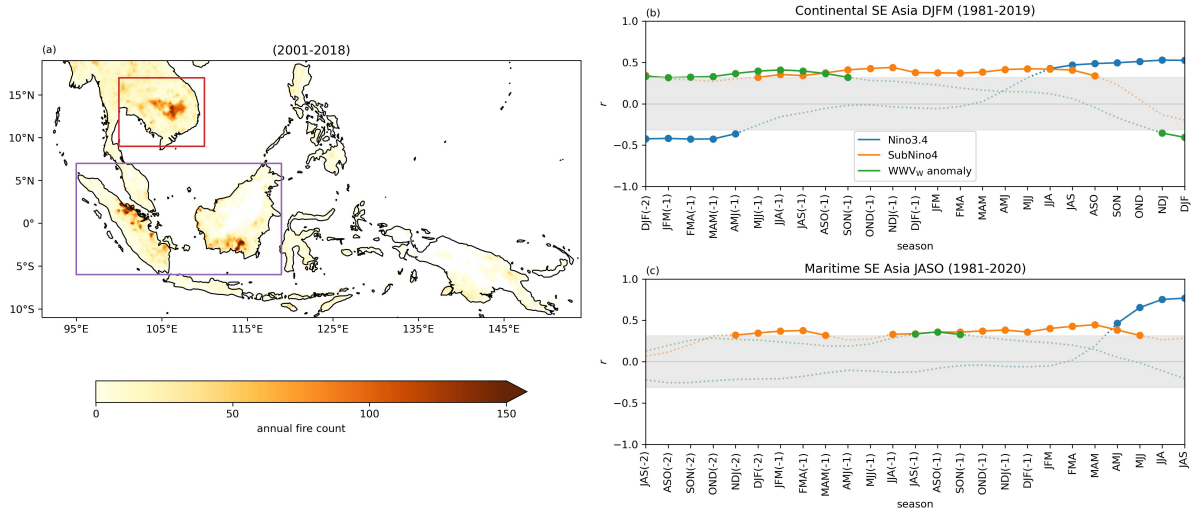


Figure A.6: Same as Figure 4.12 but showing r.

Appendix B

Supplementary Plots for Chapter 5

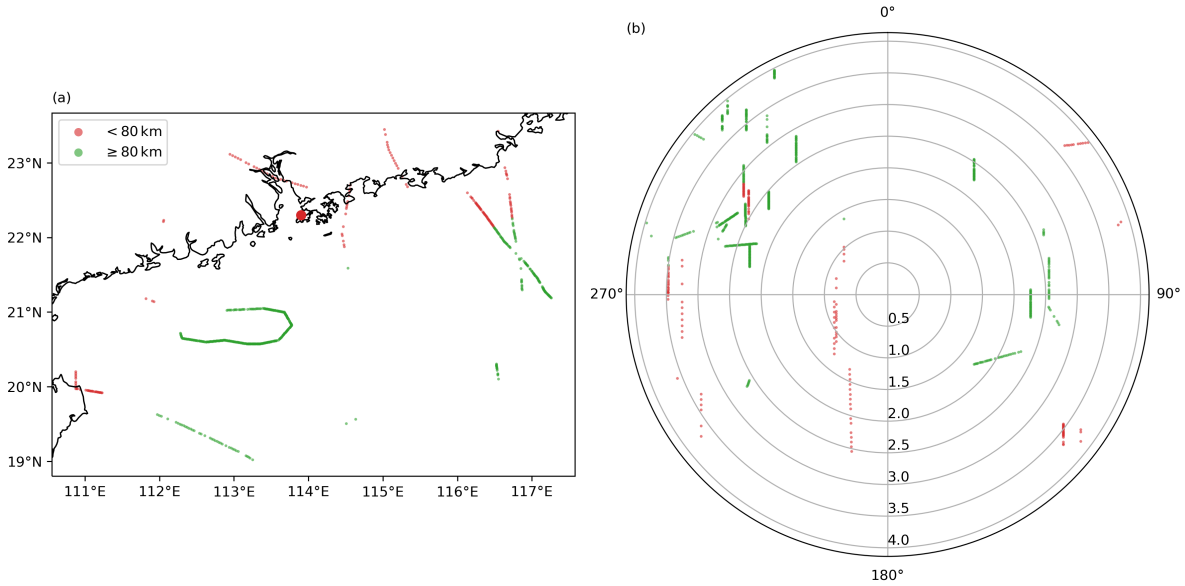


Figure B.1: Same as Figure 5.1 but for TS only, classified into close to ($< 80\,$km) and far from ($\geq 80\,$km) land.

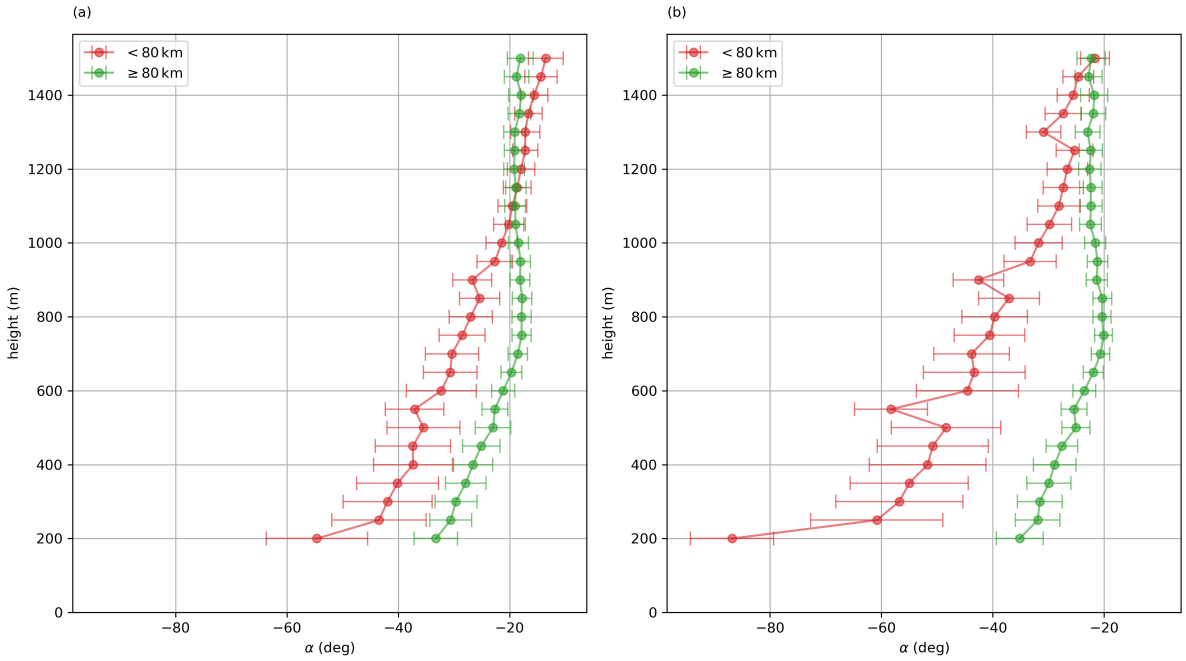


Figure B.2: Same as Figure 5.2 but with profiles composited by cyclone centre's distance to land.

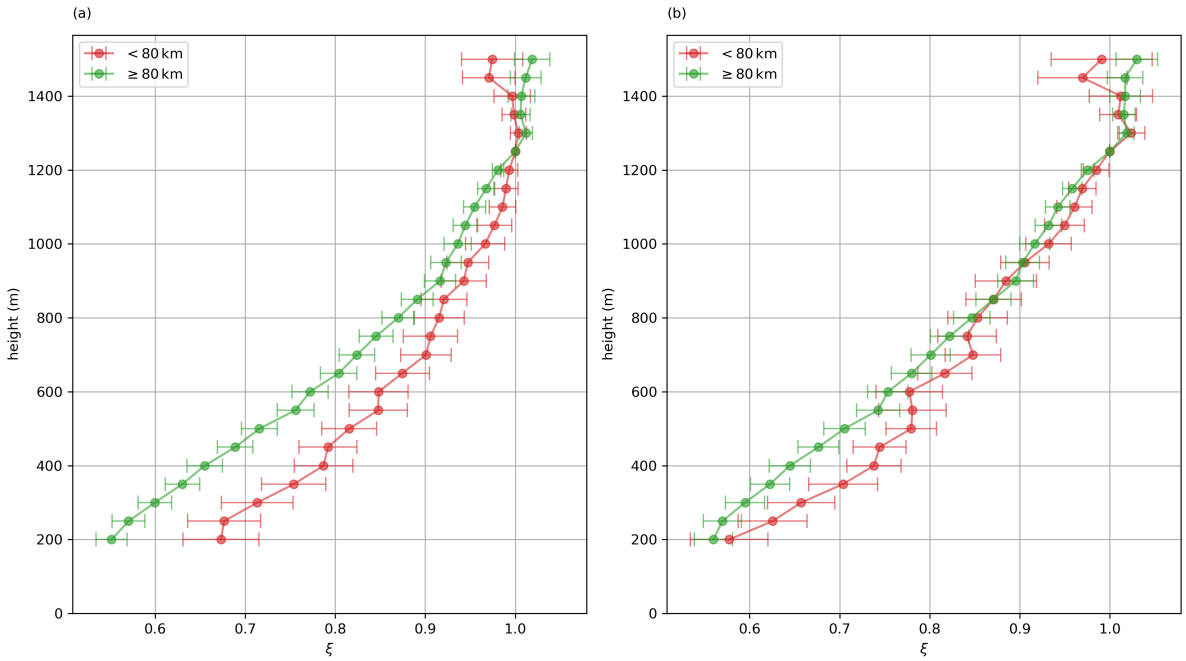


Figure B.3: Same as Figure 5.3 but with profiles composited by cyclone centre's distance to land.

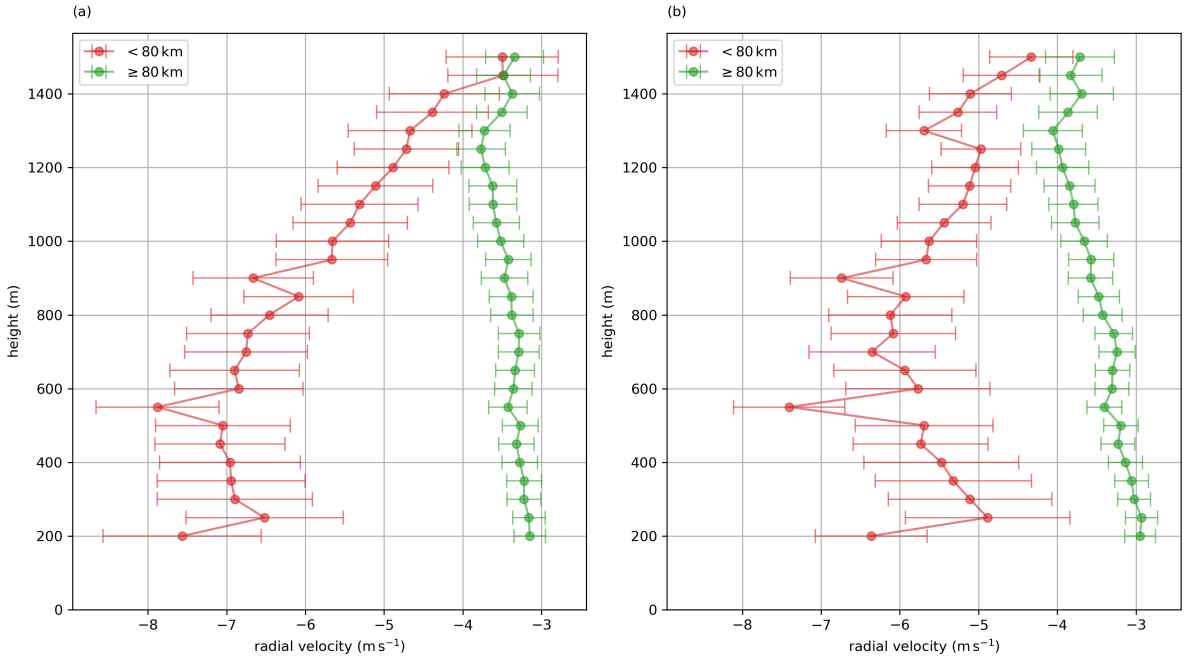


Figure B.4: Same as Figure 5.4 but with profiles composited by cyclone centre's distance to land.

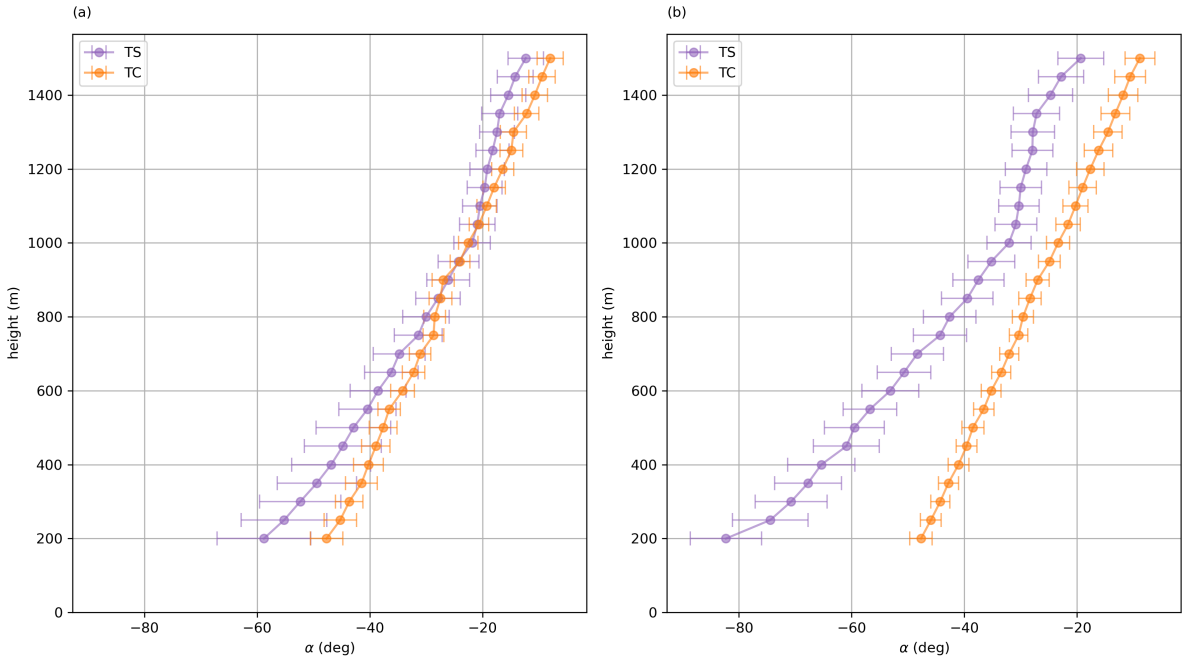


Figure B.5: Same as Figure 5.2 but for decaying TS and TC.

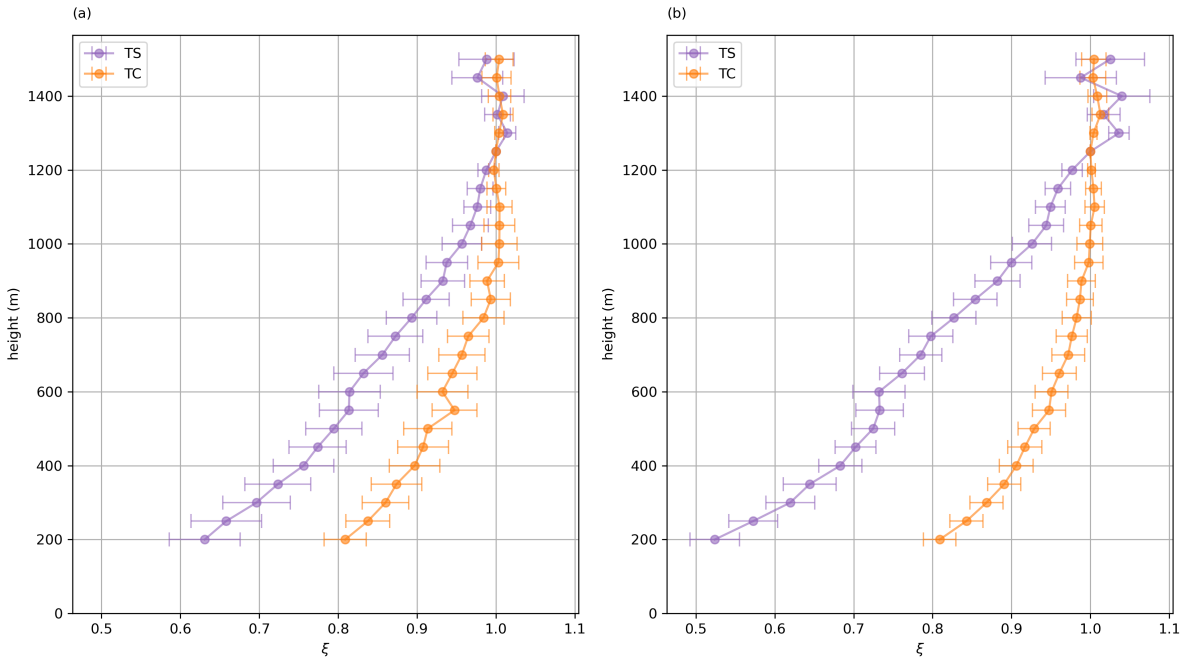


Figure B.6: Same as Figure 5.3 but for decaying TS and TC.

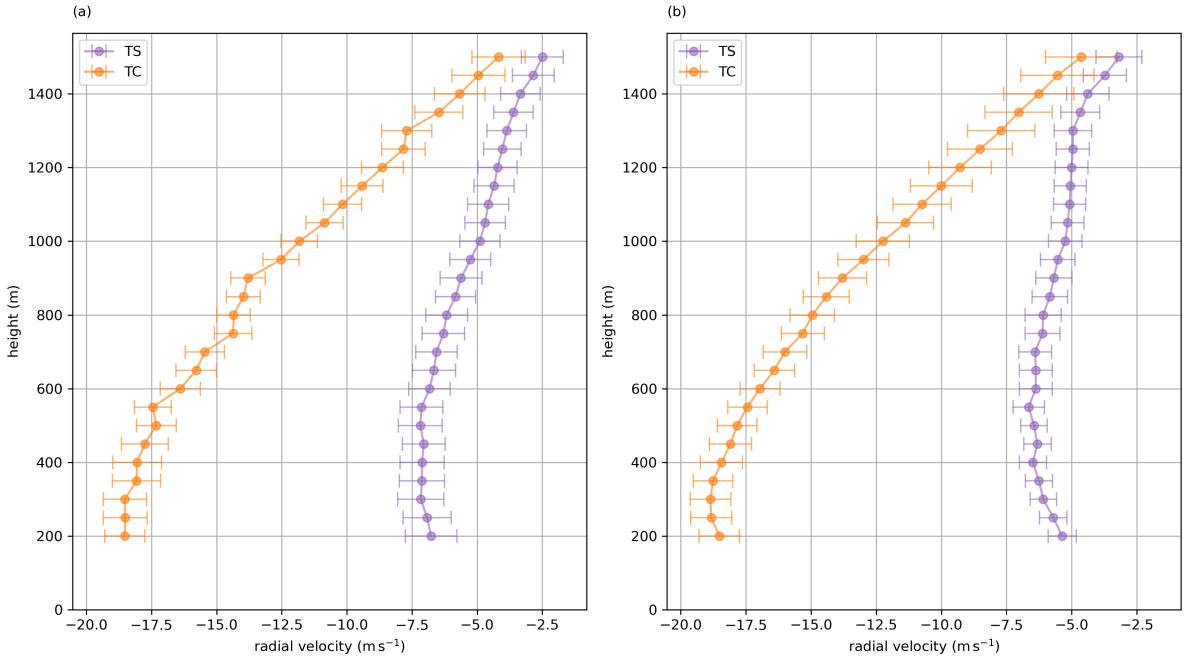


Figure B.7: Same as Figure 5.4 but for decaying TS and TC.